UNSIVERSITY OF THESSALY

SCHOOL OF ENGINEERING

DEPARTMENT OF MECHANICAL ENGINEERING

Diploma thesis

PEM Fuel Cells: Study of Carbon Monoxide poisoning in Pt-Pd/C anode catalyst layers

by

Diamantis Petros-Tilemachos

Michalas Eleftherios-Rafail

Supervisor

Prof. Tsiakaras Panagiotis

Submitted in fulfillment of the requirements for the Diploma in the Department of Mechanical Engineering of the University of Thessaly

Volos, 2022

ΠΑΝΕΠΙΣΤΗΜΙΟ ΘΕΣΣΑΛΙΑΣ

ΠΟΛΥΤΕΧΝΙΚΗ ΣΧΟΛΗ

ΤΜΗΜΑ ΜΗΧΑΝΟΛΟΓΩΝ ΜΗΧΑΝΙΚΩΝ

Διπλωματική εργασία

Κυψέλες Καυσίμου τύπου PEM: Μελέτη της δηλητηρίασης του μονοξειδίου του άνθρακα σε ηλεκτρόδια ανόδου Pt-Pd/C

Υπό

Διαμάντης Πέτρος-Τηλέμαχος

Μιχάλας Ελευθέριος-Ραφαήλ

Επιβλέπων

Καθηγητής Τσιακάρας Παναγιώτης

Υπεβλήθη για την εκπλήρωση μέρους των απαιτήσεων για την απόκτηση του Διπλώματος Μηχανολόγου Μηχανικού

Βόλος, 2022

Εγκρίθηκε από τα Μέλη της Τριμελούς Εξεταστικής Επιτροπής:

1st Examiner: Dr Tsiakaras Panagiotis (Supervisor)
Professor of Department of Mechanical Engineering,
School of Engineering
University of Thessaly

2nd Examiner: Dr Saharidis Georgios
Assistant Professor of Mechanical Engineering,
School of Engineering
University of Thessaly

3rd Examiner: Dr Brouzgou Angeliki
Assistant Professor
Energy Systems Department,
University of Thessaly

ACKNOWLEDGEMENTS

For the accomplishment of this thesis, we must warmly thank our supervisor professor Dr. Panagiotis Tsiakaras, who gave us the opportunity to assist and participate in experimental design and testing at the Laboratory of Alternative Energy Conversion Systems (LAECS) of the Department of Mechanical Engineering at the University of Thessaly. Both his guidance and his advice were determining factors for the completion of this work. His great research work has been a source of knowledge for us, to further understand complex and specific issues surrounding energy storage and energy generation devices.

We would also like to thank our parents and siblings for their enormous emotional and financial support over the years. There is no doubt that without them, the realization of this trip would have been impossible. We feel grateful to them, and we hope to make them happy.

Last but not least, we cannot help but express our gratitude to the laboratory staff, Mr. Konstantinos Molochas, Ms. Balkourani Georgia and Dr. Kontou Sotiria who helped us to deeply understand the experimental setups and the techniques that have been used.

Diamantis Petros-Tilemachos

Michalas Eleftherios-Rafail

ΕΥΧΑΡΙΣΤΙΕΣ

Για την πραγματοποίηση αυτής της διπλωματικής εργασίας οφείλουμε να ευχαριστήσουμε θερμά τον επιβλέποντα καθηγητή μας Δόκτωρ Παναγιώτη Τσιακάρα, ο οποίος μας έδωσε την δυνατότητα να παρακολουθήσουμε και να συμμετάσχουμε στον σχεδιασμό και στη διενέργεια πειραμάτων στο εργαστήριο Εναλλακτικών Συστημάτων Μετατροπής Ενέργειας του τμήματος Μηχανολόγων Μηχανικών του Πανεπιστημίου Θεσσαλίας. Τόσο η καθοδήγηση του αλλά και οι συμβουλές του υπήρξαν καθοριστικοί παράγοντες για την ολοκλήρωση της παρούσας εργασίας. Το πλούσιο ερευνητικό του έργο υπήρξε για εμάς πηγή γνώσης για την περαιτέρω κατανόηση σύνθετων και εξειδικευμένων θεμάτων γύρω από τις συσκευές αποθήκευσης και παραγωγής ενέργειας.

Επίσης, θα θέλαμε να ευχαριστήσουμε τους γονείς μας και τα αδέρφια μας για την τεράστια συναισθηματική και οικονομική συνεισφορά τους όλα αυτά τα χρόνια. Δεν υπάρχει αμφιβολία ότι χωρίς αυτούς, το ταξίδι αυτό δεν θα μπορούσε να πραγματοποιηθεί. Νιώθουμε ευγνώμονες απέναντι τους και ελπίζουμε να τους κάνουμε χαρούμενους.

Τέλος, δεν θα μπορούσαμε να μην εκφράσουμε την ευγνωμοσύνη μας στο προσωπικό του εργαστηρίου, Μολόχα Κωνσταντίνο, Μπαλκουράνη Γεωργία και Δρ. Κοντού Σωτηρία οι οποίοι μας βοήθησαν να κατανοήσουμε πλήρως τις πειραματικές διατάξεις και τεχνικές που χρησιμοποιήσαμε.

Διαμάντης Πέτρος-Τηλέμαχος

Μιχάλας Ελευθέριος-Ραφαήλ

ABSTRACT

In order to reduce the environmental damage mainly caused by the combustion of coal and petroleum, political agreements have been made to replace the fossil fuels usage with other sources of energy. Renewable energy sources are looking the most promising among the primary sources of energy. However, renewable energy sources are dependent on natural phenomena and therefore they lack reliability. To deal with this, energy storage devices are now gathering a lot of attention, as they provide a pathway to a sustainable energy future based on renewable energy sources. In fact, electrochemical devices can play a huge role in converting chemical energy into electricity and vice versa. Among those electrochemical devices, fuel cells which use hydrogen as energy carrier to produce electricity when its needed, have great potential for further use.

In the first part of this work, the basic principles of electrochemistry and some of the electrochemical devices are being presented. Followingly, further analysis around the fundamentals of operating polymer exchange membrane fuel cell (PEMFC) and their main degradation mechanism, which is known as poisoning, is taking place. The poisoning of a PEMFC is mainly caused by the presence of carbon monoxide traces at hydrogen-rich gas which fuels the cell.

In the second part of this work, electrochemical techniques including Cyclic Voltammetry, Linear sweep voltammetry, Chronoamperometry and Electrochemical impedance spectroscopy have been employed to investigate (i) the activation procedure of a PEMFC, (ii) the optimal operating temperature, (iii) the performance comparison of the cell using three different anode catalysts (Pt/C at 0.2 mg/cm^2 , PtPd/C and $PtPd_3$/C at 0.04 mg/cm^2,) and (iv) the carbon monoxide tolerance of the cell using four different anode catalysts (Pt/C at 0.2 and 0.04 mg/cm^2, PtPd/C and $PtPd_3$/C at 0.04 mg/cm^2).

ΠΕΡΙΛΗΨΗ

Έχοντας ως στόχο την μείωση της περιβαλλοντικής ζημιάς που έχει προκληθεί κυρίως από την καύση του κάρβουνου και του πετρελαίου, πολιτικές συμφωνίες έχουν συναφθεί για να αντικατασταθούν τα ορυκτά καύσιμα με άλλες πηγές ενέργειας. Οι ανανεώσιμες πηγές ενέργειας (ΑΠΕ) μοιάζουν να είναι οι πιο πολλά υποσχόμενες πηγές ενέργειας. Όμως, οι ΑΠΕ είναι εξαρτημένες από τα φυσικά φαινόμενα και άρα στερούνται αξιοπιστίας. Για να αμβλυνθεί αυτό, μεγάλη προσοχή δίνεται τώρα σε συσκευές αποθήκευσης της ενέργειας, καθώς ανοίγουν ένα νέο μονοπάτι για ένα ενεργειακά βιώσιμο μέλλον βασισμένο στις ΑΠΕ. Στην πραγματικότητα, οι ηλεκτροχημικές συσκευές, μπορούν να παίξουν μεγάλο ρόλο στην μετατροπή χημικής ενέργειας σε ηλεκτρισμό και αντίστροφα. Ανάμεσα στις ηλεκτροχημικές συσκευές, οι κυψέλες καυσίμου που χρησιμοποιούν το υδρογόνο ως φορέα ενέργειας για να την παραγωγή ηλεκτρικής ενέργειας, όταν αυτό χρειαστεί, παρουσιάζουν μεγάλη δυναμική για περαιτέρω χρήση.

Στο πρώτο μέρος της παρούσας εργασίας, παρουσιάζονται οι βασικές αρχές της ηλεκτροχημείας και κάποιες από τις ηλεκτροχημικές συσκευές. Ακολούθως, πραγματοποιείται περαιτέρω ανάλυση γύρω από τις βασικές αρχές λειτουργίας μιας κυψέλης καυσίμου πολυμερικού ηλεκτρολύτη (PEMFC) και του κύριου μηχανισμού αστοχίας, γνωστό ως δηλητηρίαση. Η δηλητηρίαση μιας PEMFC προκαλείται κυρίως από την παρουσία ιχνών μονοξειδίου του άνθρακα στο πλούσιο σε υδρογόνο αέριο που τροφοδοτεί την κυψέλη.

Στο δεύτερο μέρος της εργασίας, ηλεκτροχημικές τεχνικές συμπεριλαμβανομένων της κυκλικής βολταμμετρίας, γραμμικής βολταμμετρίας, χρονοαμπερομετρίας και ηλεκτροχημικής φασματοσκοπίας εμπέδησης, χρησιμοποιούνται για την διερεύνηση (i) της διαδικασίας ενεργοποίησης μιας κυψέλης τύπου PEMFC, (ii) της βέλτιστης θερμοκρασίας λειτουργίας, (iii) την σύγκριση λειτουργίας της κυψέλης χρησιμοποιώντας τρείς διαφορετικούς ανοδικούς καταλύτες (Pt/C σε 0.2 mg/cm^2 , PtPd/C και $PtPd_3$/C σε 0.04 mg/cm^2) και (iv) της αντοχής της κυψέλης σε μονοξείδιο του άνθρακα χρησιμοποιώντας τέσσερις διαφορετικούς ανοδικούς καταλύτες (Pt/C σε 0.2 και 0.04 mg/cm^2, PtPd/C και $PtPd_3$/C σε 0.04 mg/cm^2).

CONTENTS

LIST OF FIGURES

LIST OF TABLES

CHAPTER I

1. INTRODUCTION

1.1. Overview

Since the very beginning of the human history, sustainable energy is the Holy Grail of the social prosperity and development. Every international superpower throughout modern history is directly connected to an energy source. More recently, during Age of Steam (1770-1914 AD) Britain became the largest empire in the world as it was based on industrial coal revolution and managed to control the largest coal resources [1]. During the middle of the 20th century, petroleum powered the economic expansion and social prosperity of the global community, leading global power countries to secure oil supplies around the world [2]. That status quo lasted until the Arab oil embargo on 1973 that triggered an international oil crisis [3]. It was then that the use of alternative energy sources intensified as a meaning to reduce energy prices around the world until the prices fall again. Today, the need for alternative energy sources rises again as a path to diminish the environmental damage that fossil fuels provoke. It is why, the global community seeks to transition from a fossil-based economy to a more environmentally friendly structure economy [4]. Moving in that direction the Paris agreement was adopted by 196 entities around the world, including China, European Union, India, Russia, United States, on 12 December of 2015. According to this treaty, countries will take actions to reduce greenhouse gas (GHG) emissions (mainly produced by fossil fuels) in order to limit global temperature rise by 2050 [5]. As a result, investments in renewable energy systems and new technologies to store that energy are anticipated to take place in the foreseeable future, especially from the G20's countries. This energy transition will not be an effortless process. As of today, the energy mix of these countries is diverse considering that their major primal source of energy production is different as shown in **Figure 1**. For example, Brazil and Canada are mainly dependent on renewable energy sources (RES), while South Africa and Saudi Arabia mostly produce energy via fossil fuels. Lastly, France and Republic of Korea use nuclear energy for the most part of their energy production policy.

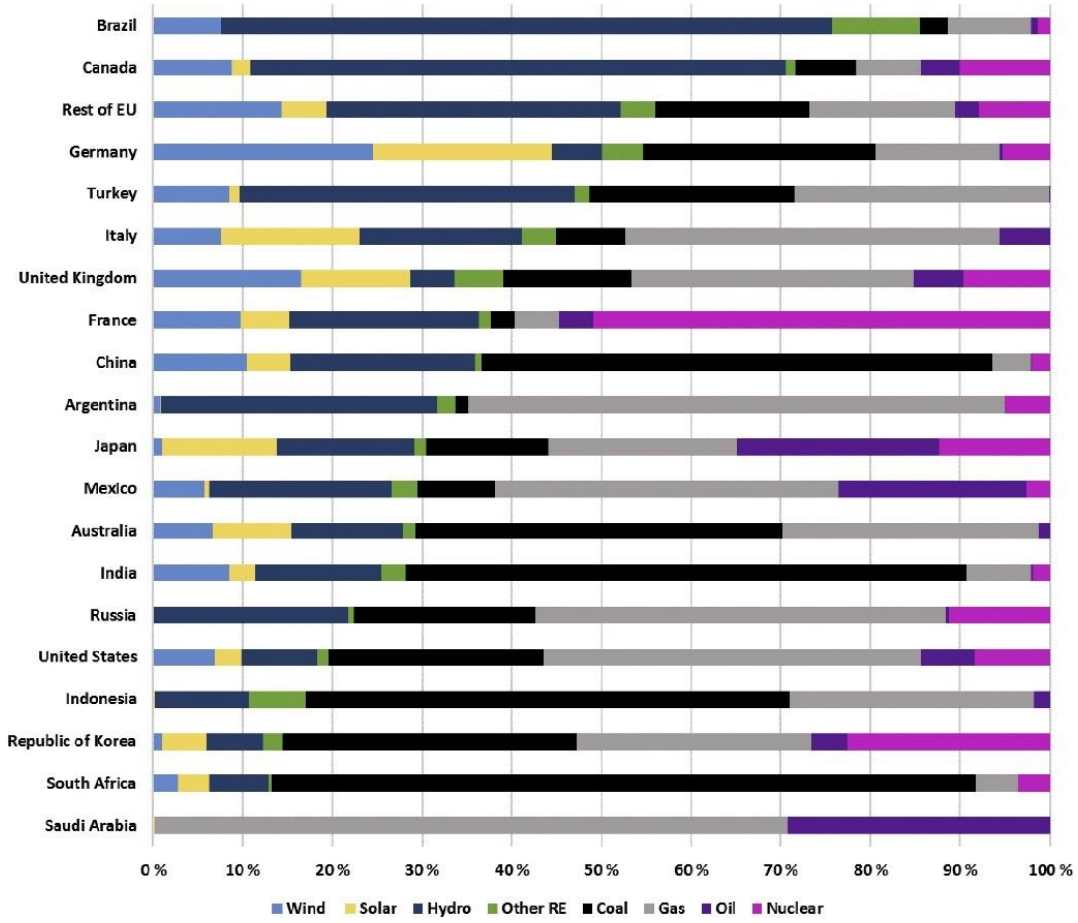

Figure 1. Shares of energy production by source across the G20 countries (Group of Twenty) [6].

1.2. Fossil fuels

Over the past years' energy was, almost entirely, produced in thermal power plants where the thermal energy is converted to electricity. The thermal energy produced by the combustion of coal, natural gas and oil was turned into high-pressure steam that is used to generate electricity. The mix of power generation in 2014 is indicative of the fossil fuels contribution, when 40,8% and 21,6% of the total electrical energy produced was attributed to coal and natural gas respectively, according to the WEC (World Energy Council) [7]. Producing energy from fossil fuels combustion has significantly improved over the last decades, since it was the center of attention. However, the emissions of the combustion (carbon dioxide, methane, sulfur dioxide) have proved to be harmful for the environment. Natural gas and oil produce less CO_2 per unit of energy compared to coal, since the coal is mainly consisted by carbon-carbon bonds while natural gas is mainly consisted of carbon-hydrogen bonds. Moreover, coal is containing a little amount of sulfur that is liberated in the atmosphere during

combustion. Therefore, it is likely that in the next few years natural gas will soon replace coal [8]. Despite their dangerous emissions, most scientists also believe that fossil fuels are not abundant, and their annually production will soon be declined [9-11]. Considering the exponential growth of global population and their improved living standards, that decline will lead to supply chain problems, therefore alternative sources of energy should be used in the coming years.

1.3. Nuclear energy

Nuclear energy was introduced in the early 1940's as a result of technologic progress for military purposes but soon enough proved to be promising for commercial use also. It became famous as a way to produce tremendous amount of energy using tiny amount of substance [12]. Nuclear power plants produce electricity from splitting atoms through the process of nuclear fission. In the beginning, uranium was used as a fuel, as it was known for its fissile behavior [13]. It was found that the original mass of the uranium was bigger than the total mass of the products of the fission, indicating that a certain amount of energy was released. This is in accordance with the theory of special relativity where the loss in mass, m, is directly connected to the energy, E, released, where $E=mc^2$ and c is the speed of light. Since the speed of light is a large value, even a small amount of material lost can result huge amount of energy. That energy produced is used in the same way as in a conventional power plant; it boils water creating steam that is used to move a steam turbine. Nuclear power plants do not produce greenhouse gasses and therefore it is considered as a practical alternative solution for energy production.

1.4. Renewable Energy

Renewable energy is energy that is produced by continuous phenomena taking place in the local environment. The energy flow regardless of the presence of any device to intercept this power. For instance, sunlight hitting the earth irrespective of the presence of any device that collect its power [14]. Renewable energy sources will play a key role in the next few years for a sustain energy future in both the developed and developing countries for three main reasons:

- They are the cleanest energy sources for the environment as they do not produce significant amounts of pollution. The use of renewable energy sources provides an alternative way to avoid both the GHG emissions from fossil fuels and radioactive byproducts from nuclear plants.
- They cannot be exhausted for the next billion years since they are related to continuous energy flow. In contrast, both the fossil fuels and nuclear energy are related to finite resources. Once they are used up, they cannot be replaced, but only after million years.
- Provide the ability to isolated and decentralized communities to produce energy depending on the local environment. As a result, they are becoming independent from both the national and the international network leading to a real energy autonomy [15].

There is a wide variety of renewable energy resources. The most significant sources such as solar energy, wind energy, hydroelectric power and biomass are already used in most of the countries to replace fossil fuels. The contribution of these sources, according to the International Energy Agency (IEA), for the last two years, is shown in **Figure 2**.

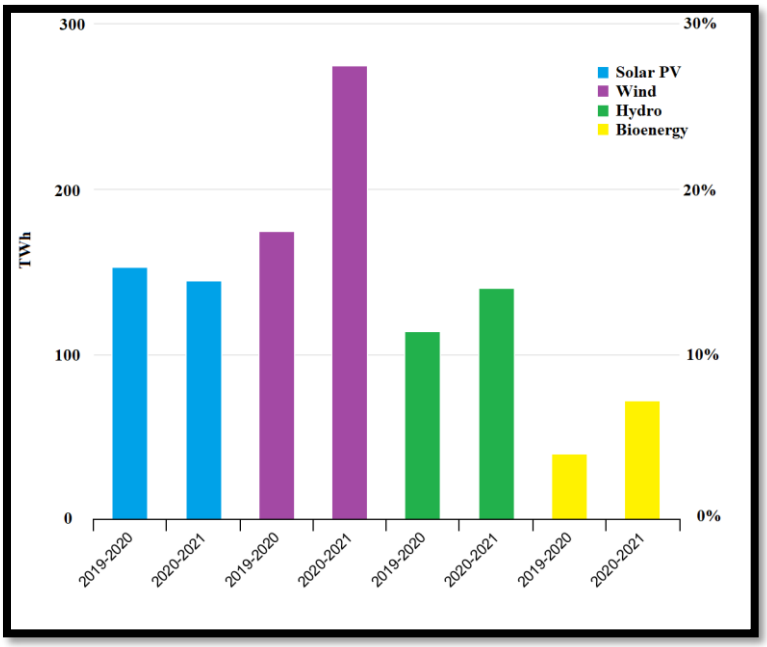

Figure 2. The outcome of the four main renewable energy resources according to the IEA for 2019-2021 [16].

1.4.1. Solar energy

Solar energy is the most plentiful renewable source of energy as 1.8×10^{14} KW, emitted from sun, reach earth surface [17]. Therefore, it is probably the most promising source of energy as it can solely power the entire human activity. The energy is reaching at earth surface both in form of light and heat. That energy is coming from a nuclear fusion reaction that converts hydrogen into helium inside the core of the sun [18]. There are two main different ways to benefit from the solar energy; either by converting the light into electricity using photovoltaics cell or by collecting the heat from the sun using concentrated solar power plants. In photovoltaics, which mainly use silicon as semiconductor, photons coming from sun hit the cell resulting in exciting electrons to move through the semiconductor giving electrical power. Concentrated solar power plants use mirrors to reflect sunlight radiation to a receiver. The heat is then used to convert water into steam that rotate a turbine [19].

1.4.2. Wind energy

Wind energy is produced by converting the motion of the wind into electricity, using a great turbine. Wind is an indirect byproduct of solar energy that reach earth surface. The irregular distribution of heat on earth atmosphere triggers the motion of the wind [20]. Wind farms can either be used on land or sea. The former was monopolizing the market when it came to wind energy. However, the limited available land areas and the visual pollution [21] caused a growth expansion in offshore wind power investments over the last few years. Besides, wind speeds at sea tends to be larger than those in the land resulting higher efficiency. Offshore wind farm does not come without a cost. More importantly, the construction and repair at a marine environment seems challenging while undersea cabling brings a higher total cost. In European Union wind shared only about 5.3% of total energy production back in 2010 according to European Wind Energy Association [22]. The target of 100 GW of wind energy has already been reached. That amount of energy can power 57 million households, corresponding to the production of 39 nuclear plants [23].

1.4.3. Hydropower

Hydropower plants convert the potential energy of water into electrical power. The water that is evaporated from the heat that sun provides on earth surface is usually gathered on high land. On its way back to the sea level, led by gravity force, its flow moves around a turbine-generator [8]. In order to improve the efficiency of this source, the water is now enclosed by dams that keep the water high. This can be also considered as mean to store energy, saving some of the water reserves for another time. It has long been a controversy among environmentalists whether hydropower should be considered a green energy solution even though it has almost zero GHG emissions. The creation of new “lakes” and the reduction of water availability on lowered water level disturb the ecosystem of the area [24].

1.4.4. Biomass energy

Biomass is defined as organic based materials that are combusted to produce energy. Biomass is accounted for a big amount of energy production globally as a primary source. Agricultural and forestry activities are the main source of biomass production. Some crops, sugar, grain and forest trimming are mainly used as biomass. They can be used to produce electricity, heat or even as a transportation fuel [25]. When it comes to the production of electricity, it used in a similar manner that fossil fuels are combusted to rotate a turbine-generator. During combustion, some GHG emissions occurs, but these emissions would still occur even if the biomass were allowed to rot in the ground. Another significant challenge is the need to completely dry the biomass before combustion as the moisture contained can largely reduce the efficiency. The most significant biofuel that it can be converted into is biodiesel, biogas and biohydrogen.

CHAPTER II

2. ELECTROCHEMISTRY & ELECTROCHEMICAL DEVICES

2.1. Electrochemistry

Considering the need of the energy transition and the rapid growth of renewable energy use, the dominance of these sources for energy production worldwide is only a matter of time. However, the renewable sources of energy are mainly dependent on natural phenomena that are hard to be precisely predicted. That is the main reason that the advocates of fossil fuels claim that the renewable sources of energy are unreliable. For example, the variation of sunlight may sometimes lead to an excessive production of energy while other times may be insufficient to supply the network demands. Therefore, low-cost, reliable, and efficient devices for energy storage must be developed in the next years. However, most of the time, the primary energy produced cannot be directly stored. It is why storage of produced energy requires the conversion of it in the first place in other forms, including thermal, kinetic, potential, or chemical energy [26]. Electrochemical devices are probably the most promising tools to serve that purpose. In this chapter, some of the main type of electrochemical devices are presented [27].

Electrochemistry can be described as the science field investigating the relationship between chemical reactions and electrons transfer/electrical energy. All electrochemical devices are based on the same principles, and they can all be compared to a simplified electrochemical cell. That cell is consisted of two electronic conductors that are called electrodes, separated by an ionic conductor that is called electrolyte [28]. All metals and carbon materials can be used as electrodes while soluble salts, acids, and bases dissolved in water are mainly used as electrolytes. In an electrochemical cell passage of electric current occurs, involving chemical reaction (Eq 2.1), taking place at the electrode/electrolyte interface.

$$O + ne^- \leftrightarrow R \quad (1)$$

where both O and R, are named electroactive species. O is the oxidized, R is the reduced and n is the number of electrons exchanged between O and R [29].

During this reaction the electrons produced in an electrode, called the anode, travel through an external circuit to the second electrode that receive the electrons, called the cathode. Meanwhile the electrolyte bulk solution allows the flow of ions but block the passage of electrons. If electrolyte permitted the electron flow, it would result a self-discharge system. The electrochemical cell can be categorized into two types; the galvanic and the electrolytic cell (see **Figure 3**).

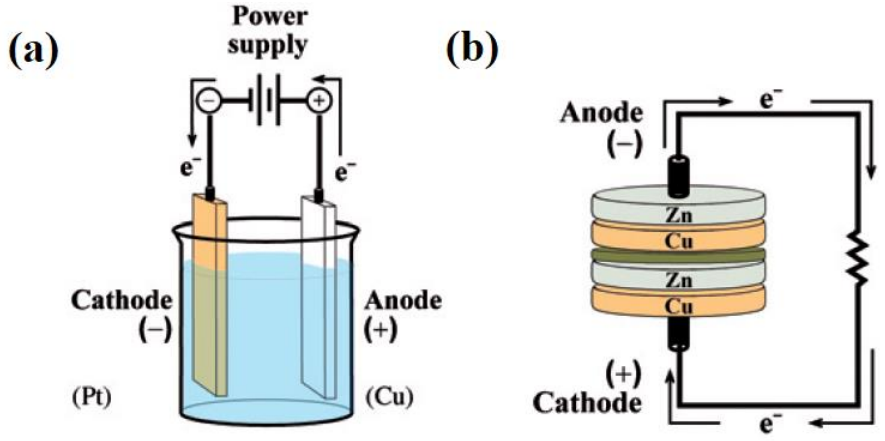

Figure 3. Illustration of (a) Electrocatalytic cell, (b) Galvanic cell [29].

In the former (**Figure 3b**), the chemical reaction occurs spontaneously and results a potential between the electrodes, triggering the flow of electrons through an external circuit (i.e., a copper wire). In the latter (**Figure 3a**), an applied potential results the flow of electrons that cause the chemical reactions at the electrodes.

2.2. Batteries

Batteries are electrochemical cells that are connected in series or parallel. They are carriers of chemical energy that is converted to electrical power according to (Eq 2.1) when used. They are considered to be one of the most convenient electrochemical devices based on their portability and their efficiency. Batteries are being categorized in two main types; i) primary batteries and ii)

secondary batteries. Primary batteries cannot be recharged as they have no reversible cell processes. In contrast, secondary batteries can be electrically recharged as they have reversible cell processes [26]. To further analyze the charging and discharging process Daniell cell should be introduced as a reference (see **Figure 4**). John Daniell (1790-1845) played a major role in battery technology development, as he was the first one achieved to obtain a continuous current by using an electrochemical cell. Daniell cell is divided in two half cells. In the first half, zinc (Zn) electrode used as anode and in the second half, copper (Cu) electrode used as cathode. Anode and cathode electrodes were dipped in zinc sulphate solution ($ZnSO_4$) and copper sulphate solution ($CuSO_4$), respectively. The two electrodes are connected with an external wire [30].

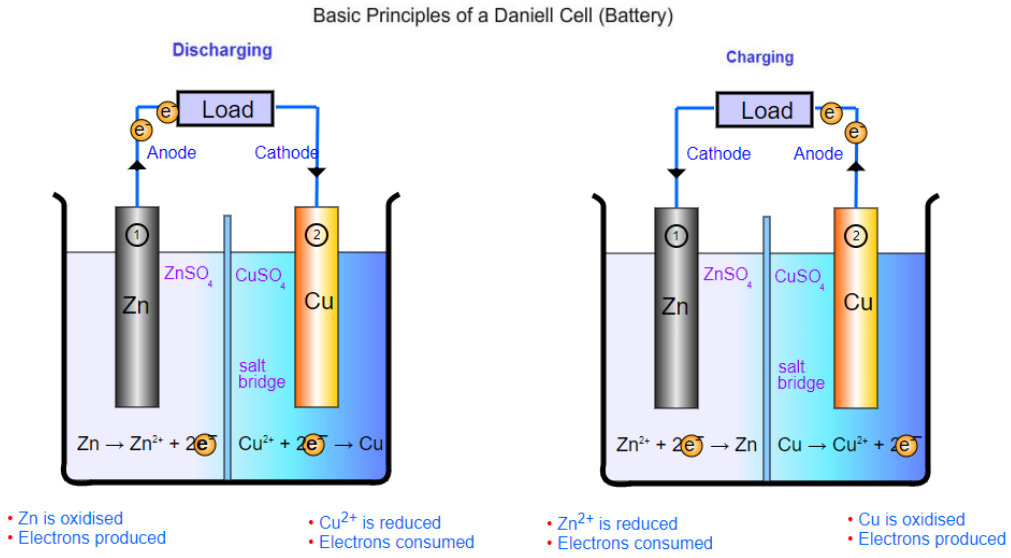

Figure 4. Illustration of discharging/charging process of a Daniell Cell [31].

During the initial state the Zinc anode electrode has more electrons than normal, while copper cathode electrode has less electrons than normal. Hence, zinc electrode is negatively charged, and copper electrode is positively charged. That-potential difference led the electrons to flow from the anode to the cathode. Throughout discharging process, electrons transfer from the anode to the cathode via the external metallic wire providing power. By the time the electrochemical active species are completely oxidized or reduced according to the following equations, the battery can no longer provide power.

$$\text{Anode: } Zn \rightarrow Zn^{2+} + 2e^{-}, Eo = 0{,}76V \quad (2)$$

$$\text{Cathode: } Cu^{2+} + 2e^{-} \rightarrow Cu, E^{O} = 0.34\,V \quad (3)$$

As it can be seen the total potential that Daniell managed to produce is 1.1 V.

If the battery belongs at the primary category, can now be recycled, or disposed. But if the battery belongs at the secondary category, it can be recharged. During recharging process an external current is applied to the cell, driving electrons back to the zinc electrode, which now plays the role of the cathode. Therefore, the anode electrode is now the copper electrode that being oxidized as described below.

$$\text{Anode: } Zn^{2+} + 2e^{-} \rightarrow Zn\,, E^{o} = -0{,}76V \quad (4)$$

$$\text{Cathode: } Cu \rightarrow Cu^{2+} + 2e^{-}, E^{o} = -0{,}34V \quad (5)$$

The most used primary batteries are alkaline and lithium-metal cells. As for the secondary type of batteries, which seem more promising, lead-acid batteries, nickel-metal hybrid cells and lithium-ion cells, are of the most used.

2.2.1. Alkaline batteries

Alkaline batteries are still up to date the most used primary battery type. Zinc (Zn) is used as anode electrode, manganese dioxide (MnO_2) is used as cathode and finally aqueous potassium hydroxide (KOH) as electrolyte. The main characteristic of these batteries is the long duration of lifetime even under heavy load or low temperature (-10 ^{o}C). This is why; they are mostly preferred to supply energy at daily used devices such as audio-visual devices, game equipment or wireless office equipment. A single alkaline cell results an initial 1.5 V that it gradually reduces under working conditions. Even after a significant amount of usage time, the cell can operate at around 1.15V for a period of time. The alkaline cell can also be used as a stack with other alkaline cells resulting 9V, when six cells stacked or 6V, when four of them are stacked [32].

2.2.2. Lithium metal batteries

Lithium batteries, also known as lithium metal (LMB), are primary batteries that use lithium as anode electrode. Manganese dioxide (MnO_2) is the most common material used in cathode, while organic solution with salt of lithium is used as electrolyte. This type of batteries are well known for

their enormous theoretical capacity that is set up to 3860 mAh/g [33]. Unfortunately, the manufacturing of rechargeable LMBs is far from ready as they exhibit poor performance [34,35]. However, in the recent years' scientists have tried to overcome this problem by using lithium-sulfur (Li-S) [36] and lithium-oxygen ($Li-O_2$) [37] batteries. Those two seem to be promising due to their great theoretical energy density [38]. Lastly, further research focuses on developing solid state electrolytes (SSE) for Li-S and $Li-O_2$ batteries, as these seem to deal with most of the safety issues occurred and increase the total efficiency.

2.2.3. Metal-air batteries

Considering $Li-O_2$ as an example, more metals have also already been used to form a metal-air battery, including aluminum, magnesium, zinc, and iron. In fact, metal-air batteries (MABs) can be classified both as primary and secondary batteries [39]. What makes MAB so special is that use an air-positive electrode. The other electrode, the negative one, is made of metal. Oxygen, which is contained in air, is reduced in the air electrode, which is actually a thin film. Therefore, several materials have been used to examine and optimize the oxygen electrocatalysis, including catalysts for both reactions [40-43]. Since the oxygen is plentiful, the battery can provide power until the metal is totally exhausted. Keeping in mind, that oxygen is coming from the outside, the interior space of the battery is solely used for the negative electrode, resulting large capacity [44].

2.2.4. Lead acid batteries

Lead acid batteries (SLA) are the first type of rechargeable batteries ever invented. Lead (Pb) is used as anode, while lead dioxide (PbO_2) is used as cathode in a sulfuric acid (H_2SO_4) solution. They are the most used rechargeable batteries and they come at low cost. Their theoretical voltage is around 2.05V [45]. During the discharging process both electrodes are turning into lead sulfate ($PbSO_4$) while the solution, giving the sulfate ions, is gradually converting into water (H_2O) [46]. The appearance of water during discharging process can cause serious problem in charging process. During charging process, the voltage of the cell will be increased, even further than the

corresponding value of water electrocatalysis. Consequently, oxygen and hydrogen gasses will be generated, requiring a special treatment to avoid charging gas ignition. Moving in that direction, some cells are designed to just let the O_2 and the H_2 to move away, while others are designed to force those two to re-form water molecules [45].

2.2.5. Nickel metal hydride batteries

Nickel metal hydride (NiMH) batteries are rechargeable systems which use nickel oxyhydroxide (NiO(OH)) as cathode and hydrogen absorbing (MH) alloys as anode electrode, while hydroxide potassium (KOH) is used as the solution [47]. NiMH batteries were firstly introduced in order to replace the nickel-cadmium batteries as an alternative eco-friendly solution because cadmium has proven to be toxic. However, NiMH also presented higher specific energy and higher peak powers. The strongest points of NiMH are their high safety and their long duration life. Hence, they seemed to be the most suitable choice for hybrid electric vehicles technology (HEV), and they were used by Toyota and Honda in 90's [48,49]. Lately, NiMH sales seem to go down as lithium-ion batteries exhibit higher performance [50].

2.2.6. Lithium-ion batteries

Lithium-ion batteries (LiB) seem to be the most promising rechargeable battery type as they already used in a wide variety of portable devices such as mobile phones, while due to their development they tend to replace NiMH batteries in HEV. They were named after their characteristic way of function. In an LiB during discharge process, lithium ions are moving from the anode electrode to the cathode electrode while during charge the process is reversed [51]. The most popular materials that used in a LiB are graphite as anode, $LiCoO_2$, $LiFePO_4$, $LiMn_2O_4$ as cathode and $LiPF_6$ as the solution [52,53]. LiB present high open circuit voltage (around 3.94V), slow discharge time and no memory effect. However, LiB have to face some challenges to become more reliable. Firstly, the low Lithium-ion diffusion kinetics during the charging process. To deal with that problem, researchers are testing new efficient materials [54]. Secondly, many fire or

explosion incidents have been occurred worldwide when the battery is heated up. Despite the number of incidents further study is needed to be done in order to define the exact mechanism that triggers the explosion [54].

2.3. Supercapacitors

Supercapacitors (SC) also known as ultracapacitors are used to store high amount of energy. Conventional capacitors and supercapacitors basic principles are much alike. However, ultracapacitors use electrolyte instead of dielectrics and greater surface area electrodes resulting higher energy density than conventional capacitors and higher power densities than batteries as shown in **Figure 5**. Thus, SC are filling the gap between the batteries and the conventional capacitors.

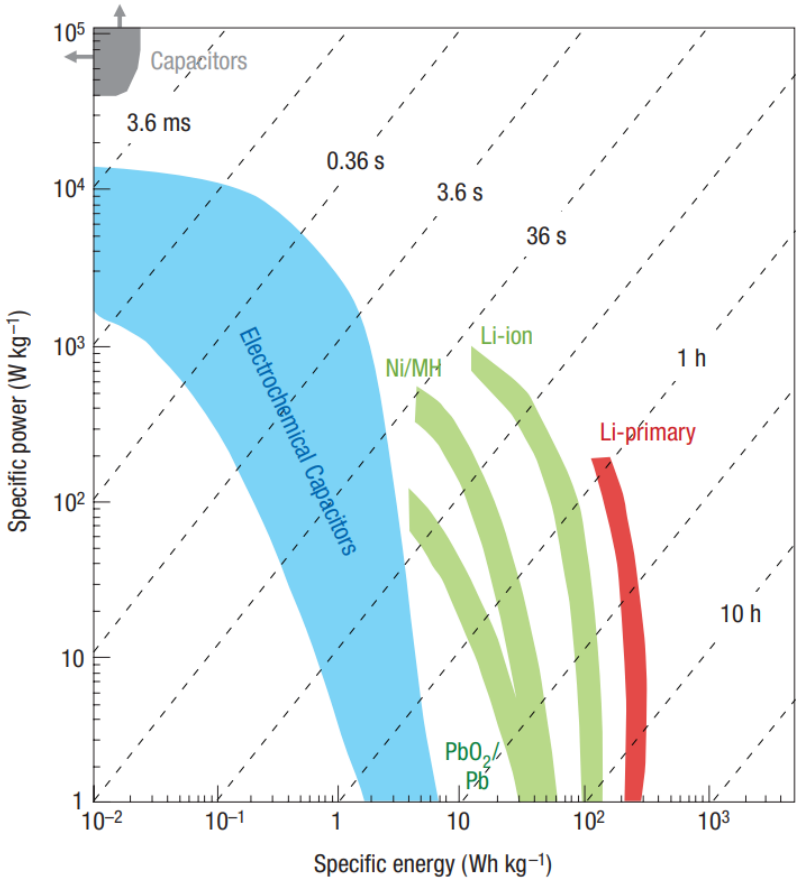

Figure 5. Specific power versus specific energy for certain electrochemical devices [55].

This signifies that if a supercapacitor is used in an EV, it can achieve higher speed but for shorter distances. Conventional capacitors do not depend on the electrochemistry to store energy but rather electrostatically. They are using two parallel metal plates isolated by physical contact by a charging

insulator material called dielectric. When voltage is applied to the device, opposite charges are gathering on each plate creating an electric field resulting to store energy [56]. Capacitance (C), Energy density (E), Power density (P) of a capacitor is calculated by the following equations:

$$C = \varepsilon_o \varepsilon_r \frac{A}{D} \quad (6)$$

$$E = \frac{1}{2} CV^2 \quad (7)$$

$$P_{max} = \frac{V^2}{4R} \quad (8)$$

where A is the surface area of the electrodes, D is the distance between them, ε_o is the dielectric constant of the vacuum, ε_r is the dielectric constant of the intercepted material, V is the voltage applied, R is the internal resistance of the device that includes all the internal parts [57,58]. As it is already mentioned before, supercapacitors are operating under the same basic principles, including the above equations. The capacity is proportional to the surface area and inverse analogues with the distance. Therefore, SC are hitting higher capacitance and energy values by increasing the surface area of the electrodes and decreasing the distance in between (see Eq. 2.6).

Three main supercapacitors type can be distinguished according to the mechanism that they use to store energy (see **Figure 6**):

a) Electrochemical double-layer capacitors (EDLC): use non-Faradaic process to store energy electrostatically. They are mostly consisted of two carbon electrodes, an electrolyte (instead of a dielectric) and a separator. When an electric field is applied to the device, the two electrodes are getting charged. As a result, the ions in the electrolyte are attracted to the opposite charged electrode, forming a double layer at each electrode. Electrodes porosity do not allow ions to recombine. As no chemical reaction occurs, the EDLCs components remain stable, meaning that the capacitor exhibits long duration life [56].

b) Pseudocapacitors: use Faradaic process to store energy through fast reduction-oxidation (RedOx) reactions. Specifically, in this case, charge transfer between the electrode and the electrolyte occurs. Both Metal oxides [59,60] and conducting polymers [61] have been

investigated as possible electrode materials because of their high conductivity. Due to the Faradaic process, pseudocapacitors hit higher energy density values than EDLC but less duration life cycles.

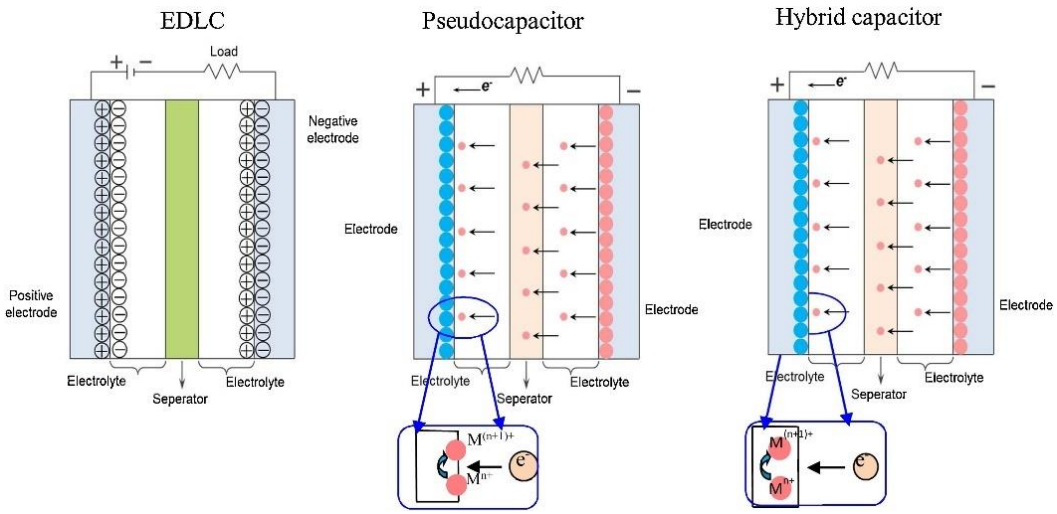

Figure 6. Illustration of EDLC, pseudocapacitor, hybrid capacitor [62].

c) Hybrid supercapacitors: are devices that combine the high-cycling duration life of EDLC and the high energy density values of pseudocapacitors. To do so, hybrid systems are combining a faradaic process electrode with a non-faradaic process electrode. That combination can increase the energy density of an EDLC without a serious reduction in life-duration of the capacitor. The two main combinations that have been tested so far are: i) a metal oxide electrode with a carbon electrode and ii) a lithium-based electrode with a carbon electrode [63].

2.4. Electrochemical sensors

Electrochemical sensors detect the amount of a specified substance/analyte using an electrode as the transducer element, to transform the signal produced from the analyte's detection in electricity. More specifically, the targeted substance is reacting with the sensing electrode producing an electric signal. That signal is analogous with the substance concentration [64]. Electrochemical sensors are consisted of a working electrode (WE), an electrolyte, and a counter electrode (CE), while a reference electrode (RE) is required for sensors that require an external

driving voltage. These electrodes (WE, CE, RE) are individually deployed within the sensor's electrolyte. Initially, the substance enters the cell via a capillary-type opening and a hydrophobic barrier, allowing enough ambient gas to react with the sensor while preventing electrolyte leakage. Followingly, the substance is reaching at the transducer electrode (working electrode) where a RedOx reaction occurs generating current that flow between the positive and the negative electrode. By measuring that current, the concentration of the substance can be defined. The working electrode (WE) must sustain a stable potential, however due to the RedOx reactions that's impossible. To monitor the potential of the transducer electrode, reference electrode (RE) is inserted in the electrolyte (see **Figure 7**) [65,66].

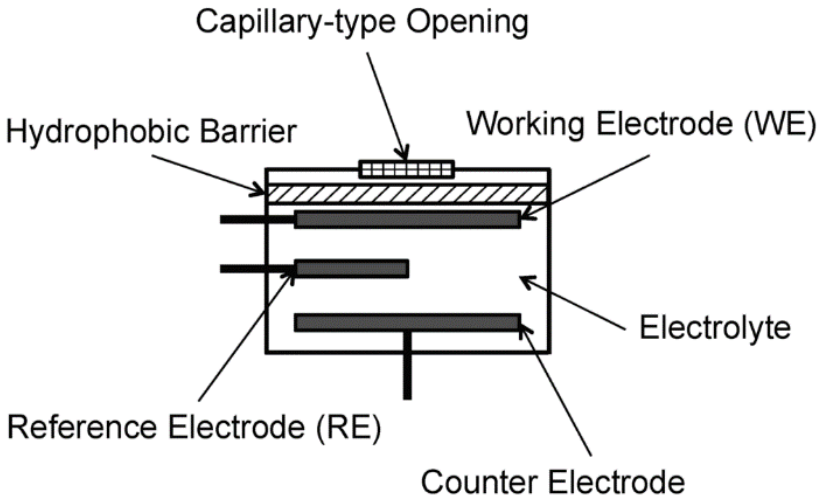

Figure 7. Schematic presentation of an electrochemical sensor [67].

Electrochemical sensors are considered superior to others, due to their high detectability and their tolerance on high temperature working conditions. They have found application in a wide variety of fields such as environment, clinical measurements, and automobile. In this context, a lot of studies for new materials have been done lately. More specifically, when it comes to the detection of gas emissions due to internal combustion machines or oxygen detection, solid state sensors have proven to be a reliable technology and therefore researchers have focused on finding suitable materials for both electrode and electrolyte [68-73]. As for the health-related field, recent studies in usage of nanomaterials in electrochemical sensors are promising better selectivity and more

accurate measurements [74-77]. Electrochemical sensors are categorized in three main categories [78]:

a) Potentiometric sensor: is measuring the potential difference between the WE and the RE when no current occurs [79]. The potential of the WE is linked to the dissolved ions of the targeted substance. For that purpose, an ion-selective electrode is used. That potential signal is then used to define the concentration of the substance according to the Nernst equation (Eq 2.9) [80]:

$$E = E^{O} + \frac{RT}{nF} \ln [a_i] \quad (9)$$

where E is the potential difference [=] Volt, E^o is the standard potential [=] Volt, R is the gas constant [=] J/K, T is the temperature [=] K, n is the number of electrons involved, F is the faraday constant [=] C/mol and a_i is the activity of the ion. This type of sensor is unrelated to the substance volume. The most popular potentiometric sensors are those that used to measure pH, NH_4^+, H^+ [81].

b) Amperometric/Voltametric sensor: is based on the current flow between the WE and the RE. Amperometric sensors monitor the current response at a constant potential while the voltametric sensors monitor the current flow at a range of different potential [82]. The WE is considered to be the key component of these sensors as it is the electrode where the RedOx reactions take place. RedOx reactions are directly affecting the electrodes and consequently the whole sensor performance. Thus, researchers are trying to find new low-cost and long-term solutions [83]. In some cases, they considered to be the most suitable solution as they do not use a reference atmosphere [84].

c) Conductometric sensor: is based on the ability of a solution to conduct an alternating current voltage is applied on the electrodes. The presence of ionic species results a modified conductance that it is measured [85]. The most important advantage over the other types is that they produced with low-cost thin film while no RE is required [86].

2.5. Electrolyzers

In recent years hydrogen, used as a fuel, have become one of the most trending topics. However, there is a common misconception about the role of the hydrogen. Hydrogen, unlike fossil fuels, nuclear and renewable sources, is not a primal source of energy as the energy benefit of it is less than the energy required to "mine" it [87]. Nevertheless, hydrogen can be used as an energy carrier that can be produced from a wide variety of primal energy sources such as wind and solar. Producing hydrogen from RES results no GHG emissions and therefore it is considered to be a promising strategy to reach energy sustainability [88]. Nowadays, there are two main ways of hydrogen production: thermal (steam methane reforming) and electrochemical (electrolysis). Among the chemical compounds that can be used to produce hydrogen, alcohols and bio-ethanol seems promising [89]. The equations (2.10) and (2.11) describe the reforming and electrolysis process respectively [90].

$$xCH_4 + yH_2O \rightarrow yH_2 + zCO + (x - z)CO_2 \quad (10)$$

$$H_2O \rightarrow H_2 + {}^{1}/_{2}\, O_2 \quad (11)$$

An electrolyzer is an electrochemical device that uses electricity to decompose liquid water into hydrogen and oxygen gasses (electrolysis) as described above. An electrolyzer is consisted of two electrodes, an electrolyte, and a directional current (DC) source. The splitting is taking place in the two charged electrodes, where a reduction reaction is happening at the negatively charged cathode and an oxidation reaction is happening at the positively charged anode as shown in **Figure 8**. The total electrochemical reaction consists of two separate reactions, the hydrogen evolution reaction (HER) at cathode and oxygen evolution reaction (OER) at anode. At the cathode, hydrogen ions consume the electrons that come from the source, while hydroxide anions are reaching the anode and set their electrons free. To achieve high efficiency, catalysts are also employed. Most common electrocatalysts used in electrolyzers are Pt, Pd, Ir, Pd and Ru. However, these noble metals are too expensive and therefore R&D is underway to employ new synthesized catalyst materials, with different structure strategies, for both the anode (OER) and the cathode

(HER) reactions [91-101]. Pure water does not conduct electric current and therefore an electrolyte is also used (such as H_2SO_4), while platinum is the most used electrode material so far [102].

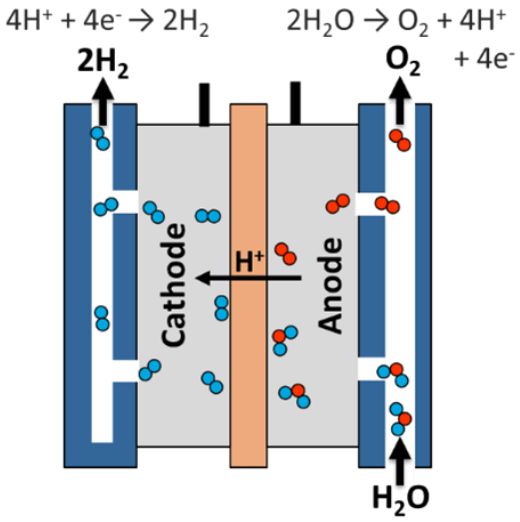

Figure 8. Illustration of an electrolyzer [103].

There are three common types of electrolyzers, based on the electrolyte used. However, the basic function principles remain the same:

a) Alkaline electrolyzer cell (AEC): is the first electrolyzer ever used. It mainly uses potassium hydroxide as electrolyte. AEC suffers from high corrosion rate and slow electrochemical kinetics especially of the CE for (OER) in an acid solution. However, AFC technology has been widely studied and it its cheap enough [104,105].

b) Polymer electrolyte membrane cell (PEMEC): uses a polymer ionic-conducting membrane as electrolyte. The thin membrane is placed between the two electrodes reducing their distance at its minimum. PEMEC is considered to be safer than AEC as it can operate under high pressure conditions and no toxic electrolyte is used (as in AEC) [106]. PEMEC are not currently widely used but due to the emerging electrolysis technology is expected to expand its usage [107].

c) Solid oxide electrolyzer cell (SOEC): is using ion conducting ceramics as electrolyte material. It is mainly used for high-temperature steam electrolysis (973-1273 K). Yttria-stabilized zirconia (YSZ) is looking a promising electrolyte, while doping materials are

tested to function at medium temperatures also [108]. SOEC is mainly used for its highly theoretical efficiency [109].

2.6. Fuel Cells

Fuel cells (FC) are electrochemical devices that convert the chemical energy of a fuel (H_2 or hydrocarbon) into electricity. The main difference between a FC and a battery is the fact that a FC can provide electrical energy as long as it is supplied with a fuel and an oxidant (mainly air). In contrast, a battery can no longer provide electricity once the chemical energy is consumed. A schematic presentation of a FC is shown in **Figure 9**. The idea behind a FC is to utilize the electron transfer from high-energy reactant bond to low-energy product bond. To achieve that, a fuel and an oxidant enters the anode and the cathode respectively, while an electrolyte solution is placed between them [110]. In the anodic side, the fuel is separated into electrons and protons which follow different directions. The electrons are moving via an external circuit, while protons are moving via the electrolyte. They are both heading to the cathodic side where they recombine to produce heat and water.

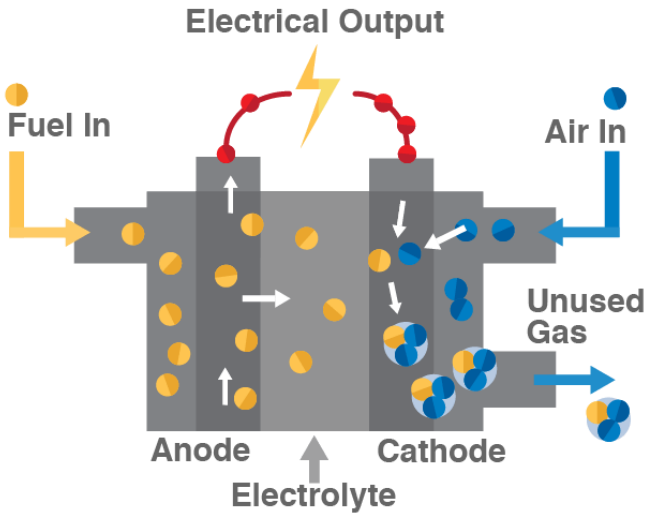

Figure 9. Illustration of a typical Fuel Cell [111].

There are five main types of fuel cells. They all function under the same principles but they are categorized based on the electrolyte and the fuel used. Each one of them also presents different efficiency and thus have different applications [112]. A short description of each type will be presented while an extensive exploration of PEMFC follows in the next chapter.

2.6.1 Alkaline fuel cell (AFC)

Alkaline fuel cell was the first FC ever employed to produce electricity. As the AEC, alkaline fuel cell is also named after the alkaline electrolyte that it is being used. The most common alkaline electrolyte used is aqueous KOH where OH^- is the charge carrier, while the electrodes are mostly made of Nickel. Those two are significantly reducing the total cost of an AFC [104]. The fuel used in an AFC is typically pure hydrogen and it is supplied to the anode. Oxygen is used as oxidant, and it is fed at the cathode. At anode, where the oxidation reaction takes place, hydrogen unites with the hydroxyl anions resulting water and free electrons that travel through the external circuit to the cathode. At cathode, where the reduction reaction takes place, oxygen, water and the free electrons are united giving hydroxyl anions [113]. AFCs are functioning at low temperatures and due to their "old-fashion" technology they are low-cost electrochemical devices. Lastly, glucose has also been tested at an alkaline fuel cell and is gathering a lot of attention as it can produce 24 electrons during its complete oxidation, which is a considerable high number. Further R&D is yet to be done, as glucose cannot be easily oxidized [114].

2.6.2. Phosphoric acid fuel cell (PAFC)

Phosphoric acid fuel cells also use only hydrogen for fuel. However, PAFC can operate with both pure hydrogen and hydrogen reformate gas mixture. This is mainly because, PAFC's temperature operation rage is set between 180-210^oC. Due to the medium temperature range and the electrolyte tolerance, carbon monoxide (CO), coming from the air does not significantly affect the cell. PAFC utilize liquid phosphoric acid electrolyte (H_3PO_4), where H^+ is the charge carrier, which is a stable proton conductor favoring protons to move for the anode to the cathode [115]. The electrolyte is contained in a thin porous matrix of silicon carbide (SiC) between two carbon-based platinum electrodes [116]. Hydrogen, which is supplied at the anode, is oxidized and the protons travel through the electrolyte while the electrons travel through an external circuit. At the cathode, the protons and the electrons are reacting with oxygen providing energy and water.

2.6.3. Molten carbonate fuel cell (MCFC)

Molten carbonate fuel cell (MCFC) has the largest fuel flexibility among the other, as it can use hydrogen or hydrocarbons (mainly methane) or alcohols as fuel. That flexibility is mainly based on the temperature at which MCFC work at (~650^{o}C). MCFC were named after their electrolyte as molten mixture of carbonates is employed in a ceramic ($LiO\text{-}AlO_2$) matrix, where CO_3^{-2} is the charge carrier [117]. The most interesting characteristic of a MCFC is that CO and CO_2 behave as fuels and not as a degradation mechanism. Nickel (Ni) and its alloy with Chromium (Cr) are mainly used as anode material while Nickel oxide (NiO) is used as cathode material [118]. The cathode is fed with air and CO_2. At the cathode oxygen which is contained in the air (~21%) reacts with the CO_2 resulting carbonates. Carbonate travels from the cathode to the anode through the electrolyte where it is reacting with the hydrogen, which is supplied to the anode, producing steam, CO_2 and electrons. CO_2 can be used to supply cathode with a recirculatory system. Despite that unique function principle, MCFC can only be used in stationary continuous applications mainly because of the high temperature and the recirculatory system needed [119].

2.6.4. Solid oxide fuel cell (SOFC)

Solid oxide fuel cell (SOFC) is the FC which operate at the highest temperature range among the other. As SOEC, solid oxide fuel cell also uses an ionic conducting membrane made of ceramics, mainly of yttria-stabilized zirconia (YSZ) where O^{2-} is the charge carrier. As any other high-temperature fuel cell, SOFC can also be fueled with reformate hydrogen gas instead of pure hydrogen or methane and still work with no significant losses [120]. Oxygen, which is used as oxidant, is getting reduced at the cathode to oxygen ions (O^{2-}) which travel through the electrolyte membrane to the anode where it reacts with the hydrogen (and CO as a product of reformate process). As a result, water and carbon dioxide molecules are generated at the anode, while heat and electricity are also products of the reaction [110]. Most of the modern SOFC devices use nickel yttria-stabilized zirconia and strontium-doped lanthanum manganite ($La_{1-x}Sr_xMnO_3$) as anode and

cathode material respectively [121]. SOFC are considered to be the most efficient type of FC and thus it will gather much attention at the foreseeable future. They can be employed at large scale activities such as industry. However, research and development (R&D) is underway to find new materials in order to reduce both the temperature operation range and electrolyte thickness that will lead at higher marketability [122-125]. For that purpose, a new type of FC has emerged, protonic ceramic fuel cells (PCFC), that use proton-conducting electrolytes. They are considered as a SOFC subcategory because they have many characteristics in common. However, PCFC can operate at lower temperatures (~500^{o}C) and they produce water at the cathode instead of the anode. PCFC ceramic electrolyte materials are usually doped perovskite compositions based on $BaCeO_3$ and $BaZrO_3$ [126].

2.6.5. Polymer electrolyte membrane fuel cell (PEMFC)

Polymer electrolyte membrane, also known as proton exchange membrane (PEMFC) is seems to be the most promising fuel cell technology developed so far. It has already been manufactured for portable applications and transportation [127]. They generally operate at low temperatures (below 100^{o}C). PEMFC are using a polymer membrane with high conductivity, mainly Nafion, as the electrolyte where H^+ is the charge carrier [104]. As for the electrode materials, both anode and cathode employ platinum (Pt) based on carbon (C) due to its high catalyst performance. However, Pt electrodes are really expensive and therefore new catalysts, some of them exhibit even higher than 0.44 A/mg at 0.9 V, are under development [128-131]. At the anode, hydrogen is oxidized and as a result the protons pass through the membrane to the cathode, while electrons are moving through an external circuit. At the cathode, oxygen meets the protons and the electrons and water is composed as the only product of the total reaction [132]. There are other types of PEMFC that use different fuel such as methanol (DMFC) and ethanol (DE-PEMFC) however they exhibit slower kinetics than PEMFC [133,134] and higher catalyst loading is needed, meaning that they also have higher cost [135].

CHAPTER III

3. PEM FUEL CELL FUNDAMENTALS

3.1. Overview

PEMFCs are used for a wide variety of applications, particularly for providing energy in vehicles. As a consequence of the high interest in these cells and in hydrogen, investment in PEMs in the last decade easily exceeded all other types of cells. PEMFC have some comparative advantages in real life application as they:

- Employ a solid polymer electrolyte
- Operate at low temperature range which allow them to start quickly and operate safely
- Release no carbon emissions when they are fueled with pure hydrogen
- Present high efficiency and high energy density

Although significant development has taken place for PEMFCs for stationary applications, many developers are now focusing on portable use. A single PEMFC cannot result more than 1V and therefore, numerous PEMFC are usually used as a stack (in parallel or in series) [136]. **Figure 10** presents a typical single PEMFC.

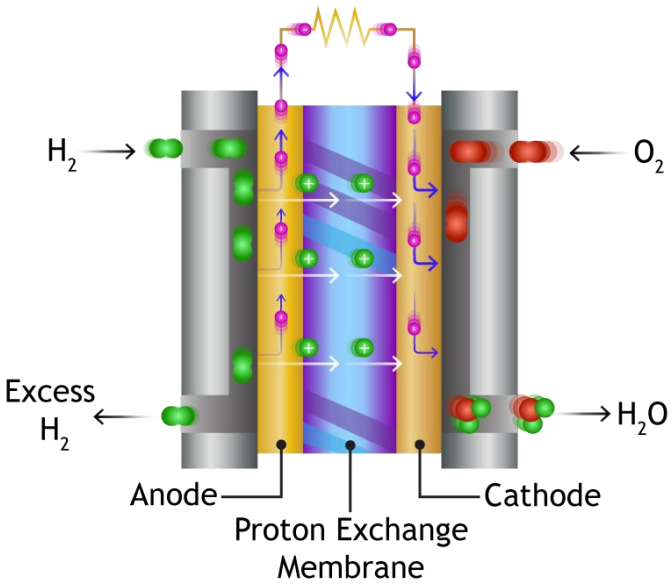

Figure 10. Schematic illustration of a typical PEMFC [137].

The two main components of a PEMFC are the bipolar plates (also known as flow-field plates) and the membrane. The bipolar plates are shown in **Figure 10** as two grey plates. Their main role is to feed both the anode and the cathode with the fuel and the oxidant respectively through flow channels [138]. Besides that, bipolar plates must also be able to remove the resulted water in a way that will not cause a flooding. The design of proper bipolar plates is quietly challenging as it should present high chemical stability, low weight and volume and low cost [139]. The polymer exchange membrane of a PEM fuel cell, not only plays the role of the electrolyte, facilitating the passage of protons from the anode to the cathode but also carries the two electrodes, which are composed by catalyst layers and gas diffusion layers at each side (membrane electrode assembly, see **Section 5.2. Membrane activation**). The catalyst layers (CL) are where the electrochemical reactions take place, while platinum (Pt) and its alloys has found to be the optimal choice [140]. The polymer membrane should exhibit remarkable proton conductivity, preventing the gas crossover and presenting high chemical stability. One of the most used polymers is Nafion [141]. The polymer membrane is the determining factor of a PEMFC performance and lifetime duration.

3.2. Working principles of PEMFC

A typical PEMFC is fueled with hydrogen at the anode, while air is used as oxidant at the cathode. As it was already mentioned, the membrane which plays the role of the electrolyte is sandwiched between the two electrodes, one at each side. At the anodic side, the hydrogen is oxidized ($H_2 \rightarrow 2H^+ + 2e^-$). It is firstly adsorbed at the free sites of catalyst and eventually releases two electrons. The formed proton hydrogen (H^+) travels through the solid electrolyte to the cathode while the free electron (e^-) travels through an external circuit. At the same time, as air enters the cathodic side, oxygen which is contained in the air, is adsorbed at the catalyst surface. This adsorbed oxygen then meets the hydrogen protons and the free electrons that reach the cathode forming water molecules ($½O_2 + 2H^+ + 2e^- \rightarrow H_2O$) that are then removed. As it can be easily understood the two reactions can occur on three phases boundary (TPB) where, an ionic conductor

(solid polymer electrolyte), an electron conductor (catalyst) and reactant gasses phase come in contact as shown in **Figure 11** [142]. The resulted water must be removed as it blocks that triple phase contact. CL must possess a large triple phase boundary zone to boost the total performance of the cell.

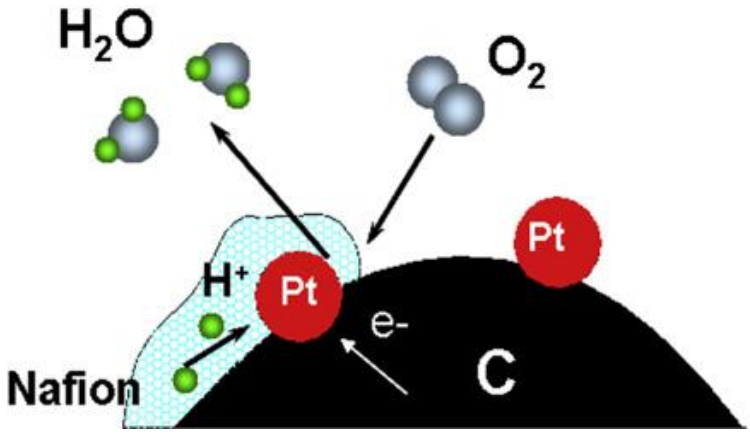

Figure 11. Illustration of a three-phase zone [143].

Anode reaction (HOR)

During the HOR, the hydrogen is decomposed into electrons and protons. However, the anodic electrochemical reaction is quite complicated and involves several steps. That being said, the reaction is principally controlled on the slowest step. Using Pt as a reference anodic catalyst the mechanism can be describes as:

$$2Pt + H_2 \rightarrow 2Pt - H_{ads} \quad (12)$$

$$Pt - H_{ads} \rightarrow Pt + H^+ + e^- \quad (13)$$

The hydrogen is firstly adsorbed on two platinum free sites through dissociative chemical adsorption and finally the dissociated hydrogen is oxidized electrochemically. The adsorption of hydrogen is the rate determining step for HOR as it shows the slower kinetic rate. In general, the HOR presents high kinetic rate and as a result, low mass loading of platinum catalyst can also be used (less than 0.05 mg/cm^2) reducing the total cost.

Cathode reaction (ORR)

On the other hand, the ORR which is the rate determining reaction exhibits slow kinetic rate. In fact, ORR is five times orders slower than HOR and it is responsible for half of the voltage losses during operation [144,145]. The ORR mechanism is even more complicated than the HOR and it is a subject of massive research. There are two main pathways for the ORR to take place in a PEM fuel cell as shown in **Figure 12**.

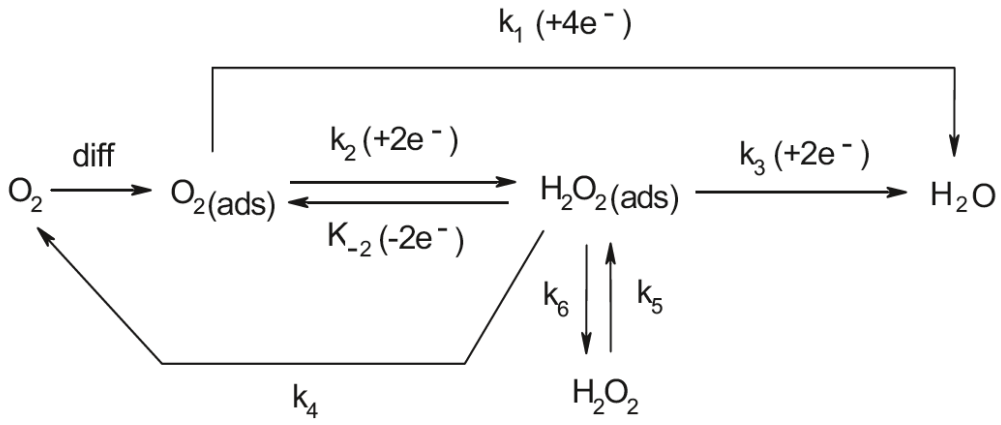

Figure 12. ORR mechanism on noble metal catalysts [143].

According to the first mechanism, the adsorbed oxygen can directly form water molecules with a four-electron involving reaction. Following the second pathway, the adsorbed oxygen is reduced by forming hydrogen peroxide (H_2O_2), as an intermediate specie, with a two-electron involving reaction. The hydrogen peroxide can then use different paths. It can be oxidized back to O_2 or further reduced to H_2O involving two-electron reaction or decomposed in H_2O and O_2. Finally, H_2O_2 can also be desorbed into the bulk and vice versa. The formation of H_2O_2 not only reduces the total performance of a catalyst but it can also proves damaging for the catalyst itself.

3.3. Thermodynamics and voltage losses

A very common way to examine a fuel cell performance is by using polarization curves. Polarization curve shows the voltage output of a FC versus current density loading (see **Figure 13**).

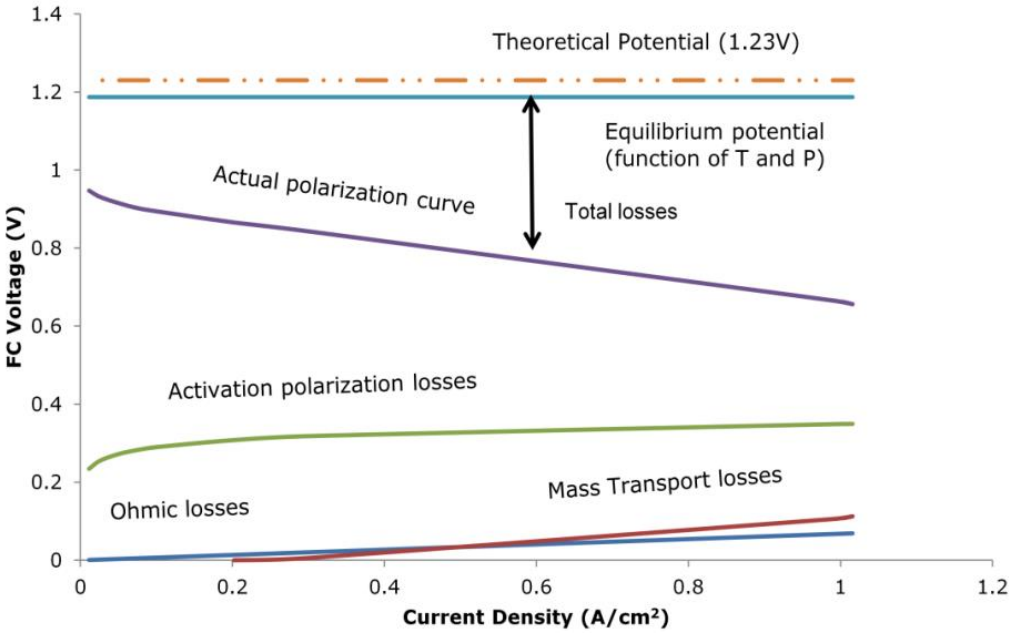

Figure 13. Typical fuel cell polarization curve at 25°C, 1 atm [146].

The theoretical potential, which refers to the reversible cell potential, can be calculated by the following equation [147]:

$$E_{th} = -\frac{\Delta G}{nF} = -\frac{G^{products} - G^{reactans}}{nF} \quad (14)$$

where n is the number of electrons per molecule of hydrogen (typically n=2), F is the Faraday's constant, ΔG is the Gibb's free energy of formation per mole difference between the products and the reactants (hydrogen and oxygen respectively) and E_{th} is the theoretical FC potential. Gibb's free energy is directly affected by the temperature and the pressure; therefore, the thermodynamic potential is not the same at any given temperature or pressure. The reversible standard potential (theoretical fuel cell potential) of a H_2/O_2 PEM fuel cell is 1.23 V per mol of H_2, calculated at 25°C operating temperature and 1 atm [148]. Even if the theoretical potential is determined as reversible, the actual open circuit voltage (OCV) of a PEM fuel cell is always lower than that indicating an irreversible voltage loss. When a load is applied to the FC, current starts to flow through the external circuit, resulting to a further voltage drop. Following the two latter points, the voltage losses can be attributed to three main phenomenon which are further describe above.

3.3.1. Activation polarization losses (ΔV_{act})

Activation polarization losses refer to the voltage losses which are caused by the slow kinetics at both the anode and the cathode. In other words, a portion of voltage is used to overcome the activation energy for the reactions. These losses dominate the low current density region of a polarization curve. The overpotentials at the anode and the cathode are called activation polarization and they are symbolized as $n_{act,a}$ and $n_{act,c}$ respectively, where [148]:

$$n_{act} = n_{act,c} + n_{act,a} \quad (15)$$

As we have already mentioned in previous paragraph, ORR is the sluggish reaction of the cell and therefore it needs much higher activation polarization than the HOR, which is quietly fast reaction. Therefore, the anodic activation polarization loss can be neglected. As the activation losses can now be determined by a single reaction, it can be described by the Butler-Volmer equation, where n_{act} (activation overpotential) is calculated by:

$$n_{act} = -\frac{RT}{anF}\ln(io) + \frac{RT}{anF}\ln(i) \quad (16)$$

where R is the universal gas constant, T is the temperature of the cell, a is the charge transfer coefficient, n is the number of moles involved, F is the Faraday constant and i_o is the exchange current density. The exchange current density is an indicator of the rate at which the reactions take place. The higher its value, the lower the n_{act}. The above equation can be reduced to Tafel equation [149]:

$$n_{act} = a + blog(i) \quad (17)$$

Where a and b are kinetic parameters. b is known as Tafel slope, and it will be further explained in **Section 4.4. Linear sweep voltammetry (LSV).**

3.3.2. Ohmic polarization losses (ΔV_{ohm})

Ohmic losses refer to the voltage losses caused by both the resistance to the electron flow and the resistance to the proton transportation. These are referred as internal ohmic resistances and they dominate the linear region of the polarization curve. Ohmic polarization (n_{ohm}) can be expressed by the Ohm's law as follows:

$$\Delta V = i \times R_{ohm} \quad (18)$$

where i is the current density [=] Ampere/cm^2 and R_{ohm} is the internal resistance of the cell [=] Ω*cm^2. The internal resistance of the cell includes both the electronic and ionic resistance and it can be expressed as:

$$R_{ohm} = R_{elec} + R_{ionic} \quad (19)$$

The ionic resistance dominates the R_{ohm} as it is much larger than the R_{elec}. To reduce the R_{ionic} thin membranes can also be used, however there are some limitations due to the fuel crossover [150].

3.3.3. Mass transport losses (ΔV_{mt})

During a PEM fuel cell operation, the cell continuously consumes the supplied fuel and oxidant to produce electricity. However, at high current densities the two gasses are consumed faster than the rate of supply. As a result, a voltage decline can be seen in high current density region at the polarization curve. The losses are even higher when the supplied gasses are not at its pure form (air instead of pure oxygen). Moreover, the water removal from the cathode can also affect this region of the graph. The current density at which the concentration of the reactants become zero is called limiting current density (i_L) [151].

Combining the above information, it can easily be understood that the actual cell voltage (V_{fc}) can be calculated as [110] :

$$V_{FC} = E_{therm} - \Delta V_{act} - \Delta V_{ohm} - \Delta V_{mt} \quad (20)$$

where activation and mass transport losses occur at both electrodes, while ohmic losses are mainly occurs at the electrolyte.

3.4. Carbon monoxide poisoning

As it was already mentioned, PEM fuel cell is gathering a lot of attention over the last few years, and they have finally reached the commercialization phase [152]. The highest performance is achieved by supplying the cell with pure hydrogen at the anode and oxygen (or air) at the cathode.

However, the cost of pure hydrogen production through electrolysis is currently too high (see **Section 2.5. Electrolyzers**). Therefore, the dominant method of hydrogen production is via stream reforming (primarily natural gas) [153]. The reformation process of a hydrocarbon results a rich hydrogen gas containing 1-2% CO. A PEM fuel cell, which mainly operates at low temperatures, cannot tolerate that amount of CO and for that reason, a process known as preferential oxidation (PrOx), can be used to reduce the containing CO at reformate product at 50-100 ppm [154]. Nevertheless, even that small concentration of carbon monoxide causes critical performance losses compared to pure hydrogen supply performance.

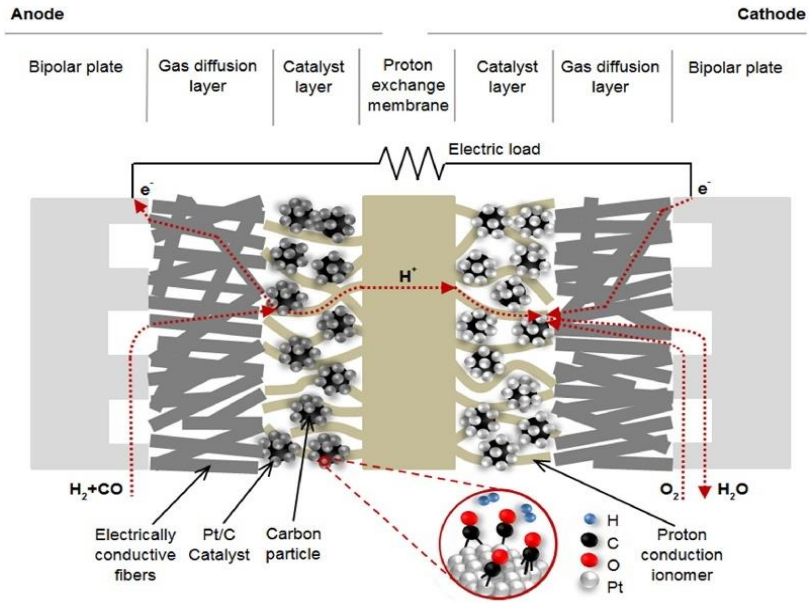

Figure 14. Schematic presentation of CO action in a PEMFC [155].

CO molecules block the active sites of platinum catalyst and therefore, the hydrogen adsorption and oxidation cannot be easily occurred (see **Figure 14**). As a result, the performance of the cell is reduced. That degradation mechanism is known as CO poisoning, and it will be further investigated in the next paragraph.

3.5. Poisoning mechanism

In **Section 3.2. Working principles of PEMFC,** the anode reaction steps were deeply discussed in case of pure hydrogen supply. However, when reformate hydrogen is supplied, the anodic catalyst behavior is not the same. Carbon monoxide is competing with the hydrogen molecules for the free

sites of the catalyst [156]. In normal operating conditions, CO is preferred by the platinum as it can be adsorbed more easily [157,158]. As a result, catalyst surface is slowly covered by CO which is attached on catalyst sites and blocks the hydrogen adsorption and oxidation. CO can be adsorbed with two different ways forming either linear or bridge-bonded species [159,160] as shown below:

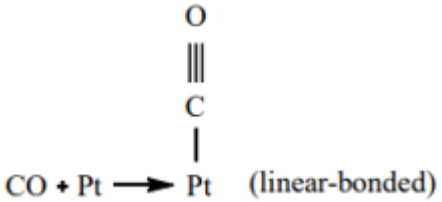

(21)

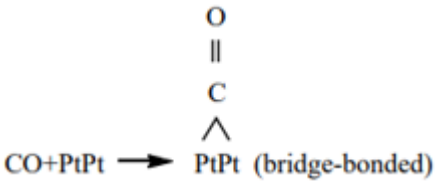

(22)

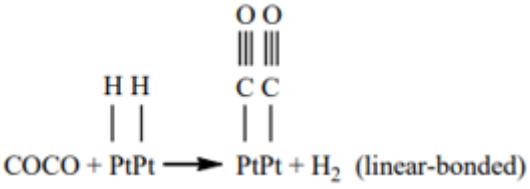

(24)

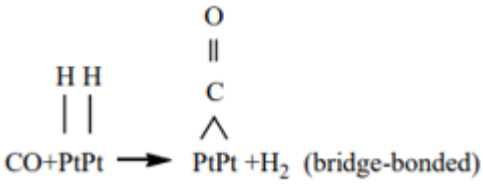

(25)

It is known that when low percentage of the catalyst is covered, the bridge-bonded species are dominant, while linear-bonded species are dominant at high percentage of CO coverage [161,162] .

3.6. CO tolerant catalysts

One of the most practical ways to reduce CO poisoning effect on a PEMFC has been considered the replacement of Platinum with other catalysts. After a long time of R&D it has been found that the binary Pt alloys are more tolerant to CO poisoning that pure Pt. The most selected elements that are used to form alloys with Pt in such catalysts are Ru, Sn, Pd, Mo, Ni [143]. As Adams et al [163] showed, when Pt-Ru alloys were used as anodic catalyst , the cell presented

lower cell voltage losses than using pure Pt during H_2/100 ppm CO supply at the anode. The alloyed catalyst must present both high HOR activity and low overpotential during CO poisoning [164]. Both the bifunctional and electronic properties of the alloyed catalyst increase the CO tolerance level of the cell. More specifically, the electronic behavior of the alloy affects the CO adsorption at low potential values while bifunctional behavior plays a major role in reducing CO coverage at higher potential values. Due to the electronic behavior of the catalyst, the formatted bond between the platinum and the carbon monoxide weakens by adding an alloyed element, while bifunctional mechanism favorize the formation of hydroxyl species at lower potential than the pure Pt [164].

CHAPTER IV

4. ELECTROCHEMICAL TECHNIQUES

4.1. Cyclic Voltammetry (CV)

Cyclic Voltammetry (CV) is one of, if not the most, popular technique used in electrochemistry, giving the opportunity to obtain a large amount of both quantitative and qualitative data about electrochemical systems [165]. In this method the potential of the system is cyclic scanned between two chosen voltage values V1, V2 (upper and lower bounds) monitoring the current in this region. The potential is swept with a constant slope (varying between 1 and 100 mVs^{-1}) as an excitation signal with a triangular potential waveform (see **Figure 15**) [166] . The plot of the current versus that potential is called voltammogram. A classic cyclic voltammogram is illustrated in **Figure 16.**

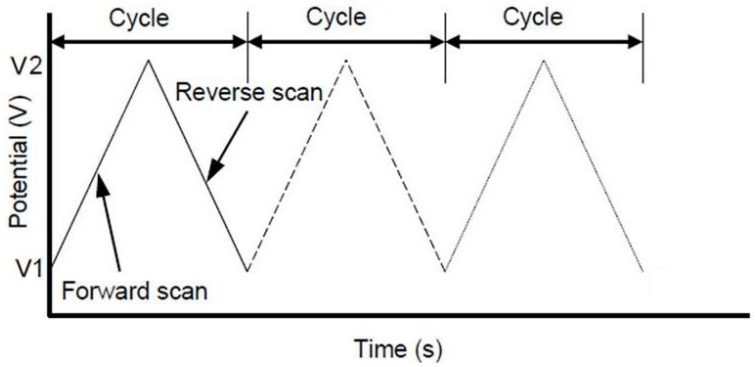

Figure 15. Typical triangular voltammetry potential waveform [166].

To have a deep understanding of CV we need to consider the influence of the applied potential on the electrode's surface. Initially, before the scanning process begins, the potential of the working electrode is such that it does not cause any electrochemical reactions (equilibrium). Once the scanning starts, the potential is being increased (or decreased) until it reaches the given potential values. As a result, oxidation (or reduction) of reactants kicks in while an anodic (or cathodic) current appears. As the potential is increased (or decreased), there is an increase (or decrease) in the anodic (or cathodic) current due to the faster reaction kinetics. The anodic (or cathodic) current is maximized at the time the voltage approaches such a value that all the reduced

electrochemically active elements are being consumed. Subsequently, the current declines, even though potential still increases, as the double-layer expanding, blocking the adsorption of the electrochemically active species. Hence, an anodic peak is shaped on the voltammogram (see **Figure 16**). Eventually, the potential approaches the upper bound, where it starts sweeping in the opposite direction (all the way from V2 to V1). Throughout the reverse process the oxidized (or reduced) elements react ,forming a cathodic (or anodic) peak [143].

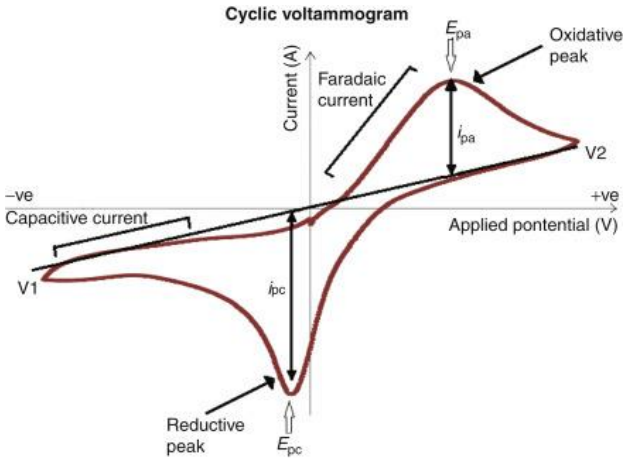

Figure 16. Cyclic Voltammogram [165].

The **Figure 16** has the following parameters:

- E_{pa}, E_{pc}: Cathodic peak potential, Anodic peak potential

Total current separated into capacitive and faradaic current:

Total Current measured= Faradaic current + non-Faradaic current

- Capacitive current (non-Faradaic current): When no electrochemical reaction takes place. It is related to the charge movements near the electrode surface (double-layer charging) [167]
- Faradaic current: Is the result of the electron transfer with the electrode surface.
- i_{pa}, i_{pc}: Peak currents (Anodic, Cathodic). The positions of these peaks do not alter with the potential scan rate (slope shown in **Figure 15**) provided that the electrochemical reactions are reversible. If this is so, i_{pa},i_{pc} are calculated by the following equation:

$$ip = (2.69 \times 10^5) n^{3/2} A D^{1/2} v^{1/2} C \quad (26)$$

where i_p is the peak current [=] Ampere, n is the overall number of electrons transferred/molecule, A is the surface of the electrode [=] cm^2, D is the diffusion coefficient [=] cm^2/s, v is the voltage scan rate [=] V/s and C is the concentration of the electrochemical active specie [=] mol/cm^3. Cyclic voltammetry is the most common tool used to characterize a new and unstudied electrochemical system. Several voltage cycles can be conducted in order to define the system stability and provide data about both the working electrode and the electrochemical reaction that take place. More precisely, a cyclic voltammetry diagram reveals the potential values at which the active species ~~is~~ are ~~being~~ oxidized (or reduced) at the working electrode surface during the oxidative scan (or reductive scan) by creating the anodic (or cathodic) peak potential E_{pa} (or E_{pc}) [168]. Last but not least cyclic voltammetry can also reveal the electrochemical active surface area that will be further discussed in Chapter VII.

4.2. Electrochemical Impedance Spectroscopy (EIS)

Electrochemical impedance spectroscopy (EIS) is a technique that measures the impedance of an electrochemical system at a range of different frequencies [169]. As distinct from resistance, that indicates the opposition to a DC flow (Time Domain), impedance indicates the opposition to an AC flow (Frequency Domain). Therefore, a small AC perturbation, at different frequencies, is applied to the system measuring and recording the response. Those measurements give the opportunity to disassociate the impact and the efficiency of the components of an electrochemical system without taking apart the cell in the first place. That being the case, EIS is the most dominant method of determining different contribution, caused by different phenomena (mass transport, reactions that take place on the surface of the electrode, double layer formation) to the overall cell impedance [170].

To better understand how an EIS measurement works, we firstly need to take a closer look at the following steps. At the start, a sinusoidal potential (or current) signal of known frequency and magnitude is applied to our pseudo-linear system measuring the amplitude and the phase-shift of response current (or potential). (See **Figure 17**). Rather than recording the response at a specific frequency, frequency sweep occur monitoring the impedance for different values, reflecting the term ‘’spectroscopy’’ [171].

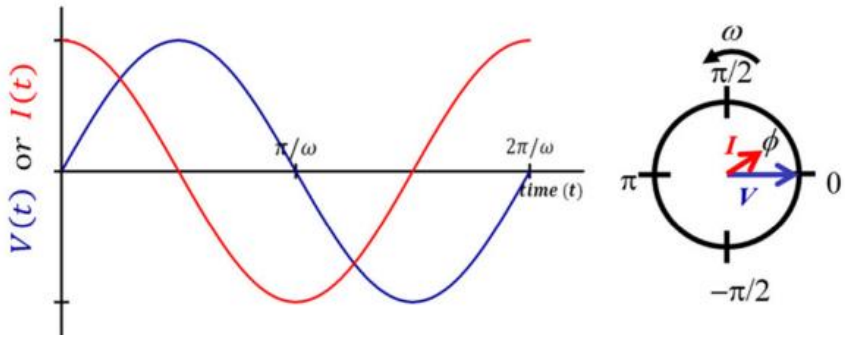

Figure 17. Sinusoidal waveform signal/response [172].

Where:

- V(t) is the perturbation (potential) signal expressed as dependent function of time (5.2).

$$V(t) = V_0 \times \sin(wt) \tag{27}$$

- Vo is the magnitude of the potential.
- ω is the angular frequency [=] radians/second. The relation between ω and frequency (f [=] Hertz) is given by:

$$\omega = 2 \times \pi \times f \tag{28}$$

- I(t) is the response signal (current) considering a pseudo-linear system:

$$I(t) = Io \times \sin(\omega t + \varphi) \tag{29}$$

- Io is the magnitude of the current.
- φ is the phase-shift angle.

Taking into consideration V_t and I_t, the impedance (Z [=] Ohm) of our electrochemical system is given by the generalized Ohm's law:

$$Z = \frac{V(t)}{I(t)} = \frac{V_0 \times \sin(\omega t)}{Io \times \sin(\omega t + \varphi)} = Zo \frac{\sin(\omega t)}{\sin(\omega t + \varphi)} = Zoe^{j\varphi} \tag{30}$$

The resulting Z can be expressed as a complex number, where it consists of two components, the real (Z') and the imaginary (Z'') component using Cartesian complex plane (see **Figure 18**):

$$Z(\omega) = Z' + jZ'' \tag{31}$$

and its phase-shift angle:

$$\tan\varphi = \frac{Z''}{Z'} \tag{32}$$

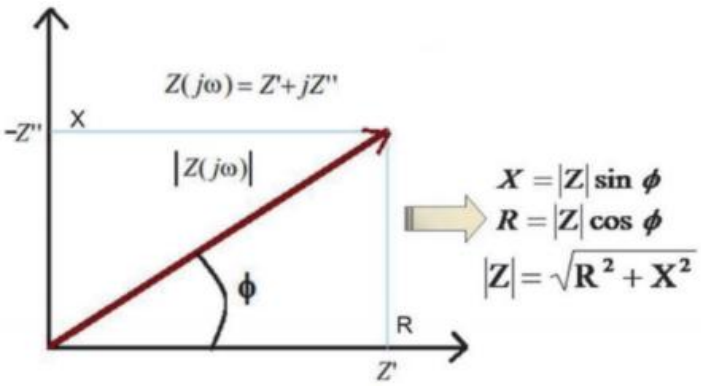

Figure 18. Vector of impedance as complex number; X refers to the capacitive behavior (imaginary part), R refers to the resistance behavior (real part) [173].

There are two common ways to exhibit the measurements of an EIS: a) Bode plot that show the phase and magnitude modifications, b) Nyquist plot that show the plot of Z' versus Z'' recorded at different frequencies. In this work Nyquist plot will be selected, as it reveals insight information about the phenomena and the parts that take place in the reaction [172].

Study of EIS technique is usually performed by matching the data to an equivalent electric system. An equivalent system is consisted of resistances (R), capacitances (C) and inductances (L) which result the same current (or potential) when the same potential (or current) is applied. That system must have at least an electrolyte resistance , a double-layer capacity and the impedance of the Faradaic of non-Faradaic process [174]. One of the most usual and simple equivalent system is a Simplified Randles circuit. Despite its ''simplified'' term, that system has been widely used to simulate a variety of complex electrochemical circuits [171]. (See **Figure 19**)

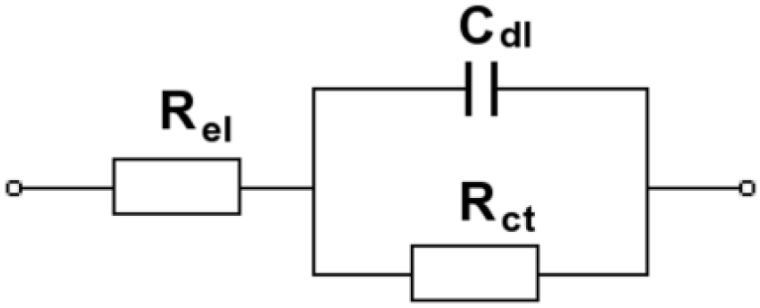

Figure 19. Simplified Randles cell [174].

Where:

- R_{el} is fitted to the electrolyte's resistance. Electrolyte resistance plays a big role in the impedance of the fuel cell. The resistance of the solution is mostly depends on the temperature, the surface , ionic concentration etc [175].

- R_{ct} is fitted to the charge transfer resistance. That resistance refers to the blockade which the electron must overcome through the electrode surface to the electrochemical active species, or from the electrochemical active species trough the electrode. R_{ct} is inversely related to the overpotential. The bigger the overpotential, the lower the charge-transfer resistance [174].
- C_{dl} is fitted to the capacitance of the double-layer formatted. That double-layer exists in the interface between the electrode and the electrolyte, and it is formed as ions from the bulk solution adsorb on the electrode. The ions are distinguished by a neutralizing space.

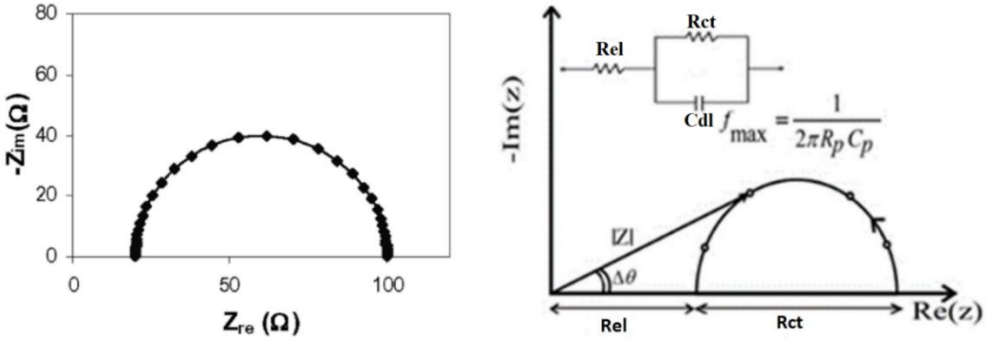

Figure 20. Nyquist plot of a simplified Randles cell [174],[176].

As **Figure 20** shows, the Nyquist plot of such a cell is always semi-circle. Remarkably, as shown above, those diagrams can reveal some important values for our equivalent system. At high frequencies the contribution of the double layer capacitance on the total impedance is negligible, as a result the measured impedance meets R_{el}. Moving on lower frequencies the impedance is calculated between R_{el} and $R_{ct} + R_{el}$. At the low frequencies' region, where arc of the plot intercepts with the real axis of impedance, the total impedance is $R_{ct}+R_{el}$. Consequently, the high frequency is linked with the solution resistance, whilst the low frequency is linked with the resume of the two resistances. The corresponding frequency of the maximum value of $-Z_{im}$ is called characteristic frequency ω_c.

4.3. Chronoamperometry (CA)

Chronoamperometry (CA) is one of the simplest techniques and yet a reliable method to analyze electrochemical reactions and cells. CA is a step technique, meaning that a single potential step is applied at a specific time t=0 recording the current response versus time [176]. To evaluate

in depth how a chronoamperometry works, we first need to consider a cell where the following charge transfer reaction takes place (see **Section 2.1. Electrochemistry**):

$$O + ne^{-} \leftrightarrow R \tag{1}$$

At first, voltage is such that O that the reaction does not occur and therefore no electrons are transferred. Then a step voltage change occurs (E > Eo) and the reaction starts on the electrode's surface leading to a current flow mainly controlled by the diffusion phenomenon [177]. In this case the current flux follows Cottrell equation:

$$i(t) = \frac{nFA\sqrt{Do}\,Co}{\sqrt{\pi\, t}} \tag{33}$$

where i is the time-dependent current recorded [=] amperes, n is the number of electrons that participated in the reaction, F is the Faraday constant [=] C/mol, A is the electrode's surface [=] cm^2, c is the concentration of the electrochemical active species [=] mol/cm^3, D is the diffusion coefficient [=] cm^2/s and t is the time [=] second. **Figure 21** illustrates the above-described phenomena for a planar shaped electrode surface:

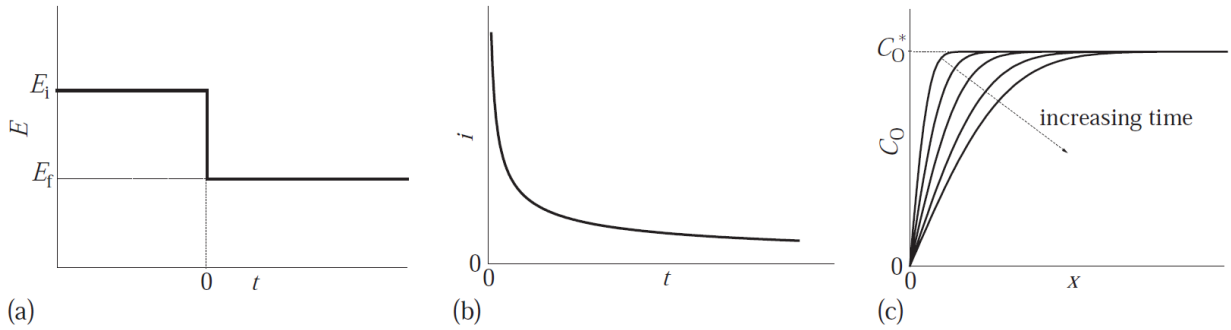

Figure 21. (a) Applied potential step versus time, (b)current output versus time, (c) concentration versus distance near electrode surface [29].

After the applied potential step at t=0, the potential can be either preserved at the same level or it can be also changed to a new level at a future time (t=τ).

The last-mentioned method is called double step chronoamperometry. The response, here, is examined as a reversal method [178]. **Figure 22** shows a typical diagram of a double step CA.

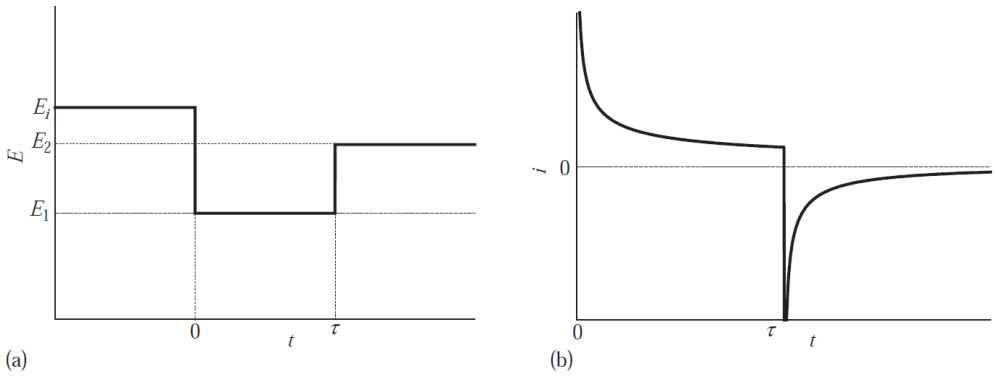

Figure 22. Double step potential technique: (a)potential excitation signal, (b)current response [29].

Chronoamperometry, both single and double step is commonly used for studying the reaction kinetics, absorption, and adsorption. In general, chronoamperometry is also used to study the required time that the system needs to stabilize after the potential is stepped to a new value.

4.4. Linear sweep voltammetry (LSV)

Linear sweep voltammetry (LSV) is a very similar technique to Cyclic voltammetry (CV). Both techniques apply voltage across the electrochemical cell and measuring the current that flows because of that applied potential. Unlike CV, LSV is not cycling the potential value between the two specific boundaries. The potential is ramped up (or down) linearly in a single direction, from a lower (or higher) given voltage to a higher (or lower) given voltage, monitoring the current response through time (see **Figure 23**).

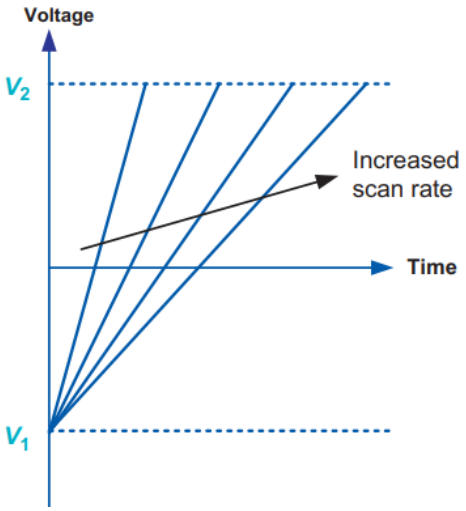

Figure 23. Linear sweep voltammetry [179]

Due to its simplicity and convenience LSV is one a basic method to characterize a new membrane [180]. The resulted plot of voltage versus current is called polarization curve and it is widely used to evaluate the performance of an electrochemical cell. The data extracted by a LSV measurement are the voltage, current and time. This information can be used to create a Tafel plot using Tafel equation. The Tafel equation relates the tested overpotential to logarithmic value of the current density, i [=] ampere per cm^2:

$$n = \frac{RT}{aF} \ln i_o - \frac{RT}{aF} \log i \tag{16}$$

where n express the overpotential applied ($n = E - E_O$). That equation can be further simplified as follow:

$$n = a + b \log i \tag{17}$$

where α and b are constants. By plotting the overpotential versus the logarithmic value of the current a linear graph is extracted (see **Figure 24**). By doing so, two important parameters, for the evaluation of the catalyst can be obtained from the graph: (a) the exchanged current density (i_o) that could be extracted by replacing n=0 and (b) the Tafel slop, which is a useful diagnostic tool.

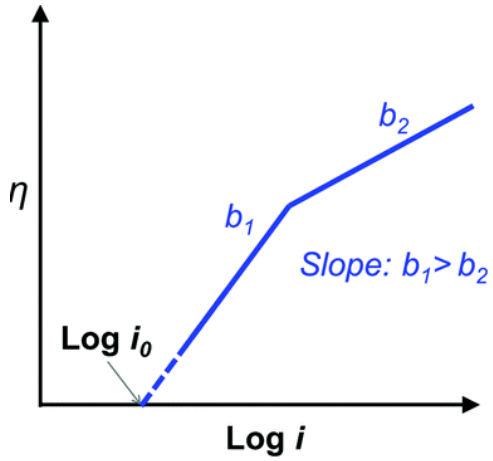

Figure 24. Tafel plot [181].

The Tafel slope is indicative of the electrode's kinetics. The bigger the slope is, the slower the kinetics are. Taking **Figure 24** as an example, we can assume that the current is not increased with the same ratio for a given overpotential in the case b1 and b2 [181]. For the most part of electrochemistry, it is desired to have an increased current flow from a reaction with low overpotential changes.

CHAPTER V

5. EXPERIMENTAL PART

5.1. Experimental Apparatus

All experiments were performed on a single PEM cell to evaluate and compare the activity of four different anode catalyst layers during CO poisoning degradation. The measurements were executed by using anode both as the counter and reference electrode, while the cathode served as the working electrode. The equipment used in the present work is shown in **Figure 25**. The gases that were used are hydrogen, carbon monoxide, nitrogen and oxygen. They were supplied through a mass flow controller (MFC) to accomplish the desired flow rates. Before entering the cell, the gasses were humidified to ensure membrane ionic conductivity. The humidifiers were connected with a recirculator that circulate distilled water at a given temperature. The cell was warmed up to the desired temperature by using a rheostat and a thermocouple to adjust and record the temperature. Finally, recording the response, an AMEL 7050 potentiostat/galvanostat, connected with a personal computer, was used.

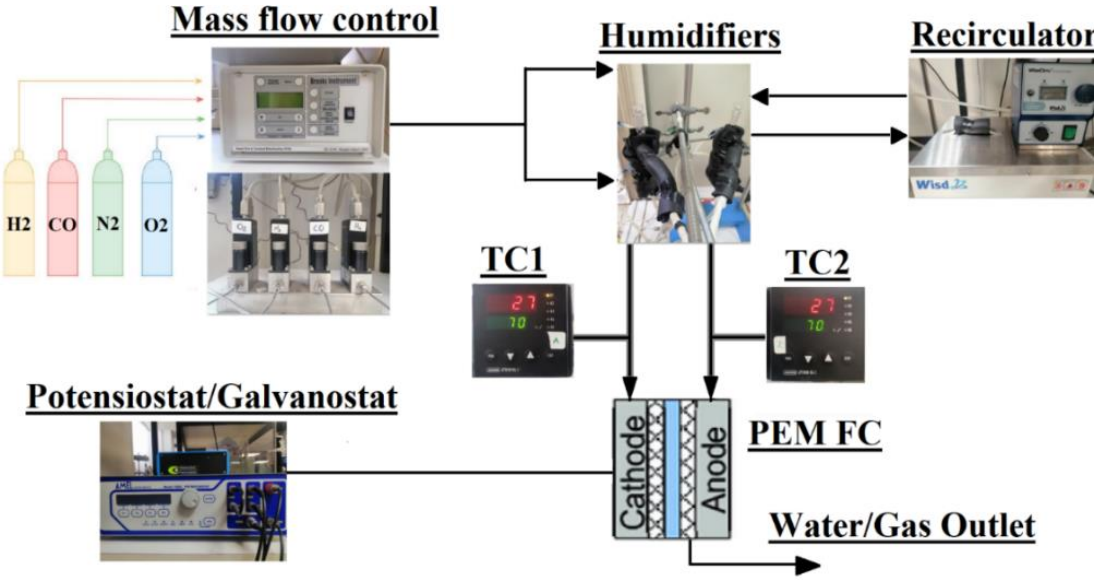

Figure 25. System illustration setup

5.2. Membrane activation

The MEA (Membrane electrode assembly) is the key point of a PEMFC. There are two different ways to construct a MEA (see **Figure 26**), leading to the same similar structure composed of: (a) The anode and the cathode diffusion layers, which main role is to diffuse the gasses to the catalyst layers and remove the produced water at the cathode, (b) The anode and the cathode catalyst layers, where the reactions take place and current is generated and (c) the membrane that behaves as a typical electrolyte, facilitating the passage of the protons from the anode to the cathode [182].The tests were all carried out on a MEA with an active electrode area of 5 cm^2 , while Nafion 115 was used as the solid electrolyte. The four different MEA compositions used were: MEA 1: Pt/C (0.2 mg/cm^2)| Pt/C (0.2 mg/cm^2), MEA 2: PtPd/C (0.04 mg/cm^2)| Pt/C (0.04 mg/cm^2), MEA 3: $PtPd_3$/C (0.04 mg/cm^2)| Pt/C (0.04 mg/cm^2), MEA 4: Pt/C (0.04 mg/cm^2)| Pt/C (0.04 mg/cm^2).

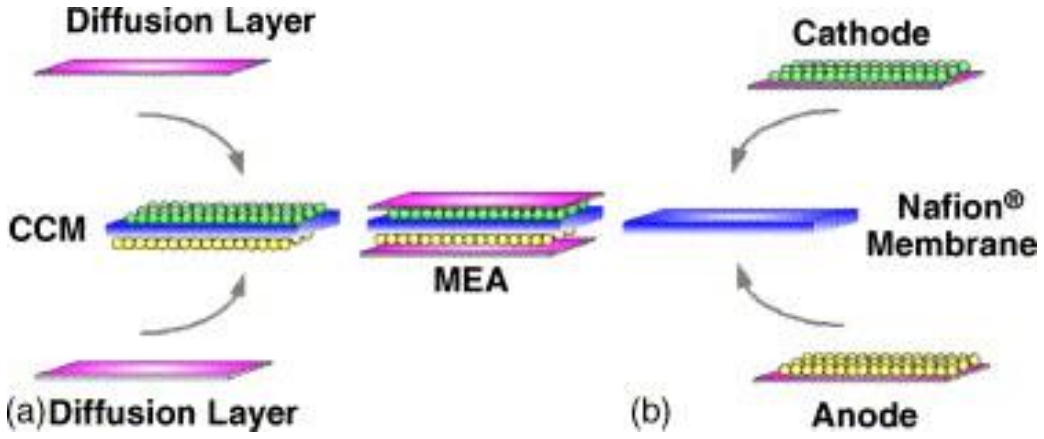

Figure 26. Illustration of a membrane electrode assembly fabrication

A new, unused MEA does not achieve its peak performance and that is the reason it must be ‘’activated’’. The terms break-in, conditioning and activation have all been used to report the above scope. The activation process is the first operation of the MEA, where the performance progressively improves until reaching a maximum and constant level. The duration of this process is well known as the break-in time. As we mentioned above, ‘’conditioning’’ has also been used, but is mostly refers to a recovery process for a reused MEA [183]. During the break-in procedure the MEA is hydrated, the impurities are removed from the catalyst layers, the pathways for the reactants to approach catalyst are formed and eventually the cell’s performance is stabilized [184]. Defining

new and efficient ways to minimize the break-in will be a game-changing step towards fuel cell manufacturing. In the past few years numerous break-in approaches were studied to maximize power density and durability of a MEA, involving voltage scanning/stepping, constant current applied and others. Two reviews that summarize the knowledge about activation were considered for this work. The first one was introduced in 2011 by Yuan et al. [185] and the second one is from 2013 by Zhiani et al. [186]. Those reviews investigated the application of constant voltage, cycling voltage and constant current during break-in. It was found that a constant current application is not as effective as the application of constant voltage and potential cycling, as the main goal of break-in is the hydration of MEA and the removal of impurities. Yuan et al. used constant voltage ~0.6 V until constant current is obtained.

In this work activation took place by (a) chronoamperometry at 0.55 V until obtaining stable performance the anode supplied with humidified H_2 and the cathode fed by O_2 at and (b)cyclic voltammetry between 0,05-0,85 V, while hydrogen and nitrogen were provided to the anode and the cathode respectively, at a scan rate of 100 mV/s to restore the active sites until no further improvement is recorded.

5.3. I-V polarization curve

All the I-V curves were carried out by ramping up the voltage from open circuit voltage (OCV) to 0,3V at a rate of 5.0 mV/s. The polarization curves were taken by providing the anode with humidified H_2 (fuel cell and H_2 pump test) or H_2/CO (fuel cell test) which was used as dynamic hydrogen reference electrode (DHE). At the same time, the cathode was supplied with humidified O_2 (fuel cell operation) or H_2/CO (H_2 pump operation) to compare the behavior of the cell before and after poisoning degradation. Anode and cathode gasses were supplied with 80% relative humidity (RH) and at ambient pressure. The results of this method shown in Chapter VII are emerged as the average curves of 4 different measurements for a more valid graph.

5.4. Cyclic Voltammetry experiments

The Cyclic Voltammetry is adopted to evaluate and compare the electrocatalytic performance of the catalysts. It is mainly used to define and compare the electrochemical surface area (ECSA). ECSA refers to the electrochemical reactivity capacity of the MEA, which is mainly declined due to impurities, poisoning and nanoparticles aggregation. The ECSA active centers that are available for the electrochemical reaction to take place. The bigger the electrochemical surface area the better the catalyst performance [187]. To calculate the ECSA, an inert gas, nitrogen is supplied to the cathode of the fuel cell and hydrogen is supplied to the anode. Afterwards, a voltage scanning is applied between 0.05-1.2V at 50 mV/s scan rate.

5.5. EIS experiments

Electrochemical Impedance Spectroscopy is a useful tool to define transport losses, the ohmic resistance, electrode properties (e.g., resistance to movement of charged particles), capacitance and MEA performance [188]. In the following chapter, the tests were carried out by an AMEL 7050 in potentiostatic mode. The impedance spectra were monitored in the frequency range of 10000 Hz to 0.01 Hz around open circuit voltage. To authenticate the impedance spectrum, the cell must be stable during the EIS measurements. The MEA had already been activated before the EIS measurement followed by a voltage cycling to achieve a steady state and maximum wettability. During those measurements, 80 ml/min H_2 was fed to the anode electrode, while 80 ml/min with 100 ppm CO/H_2 was fed to the cathode electrode.

5.6. Effect of temperature and relative humidity

PEM fuel cells operating conditions have a significant contribution to the performance of the cell. In that sense, it is crucial to know the optimal conditions that lead to the maximum desired outcome. For that purpose, the cell was tested while differing two main operating conditions, the temperature of the gases/cell and the relative humidity of MEA. Temperature is known to affect the efficiency and durability of the PEM fuel cell. Specifically, an increasement in operating

temperature results also to an increasement in the power production of the cell but decreases the durability of the PEM [189]. As for the relative humidity (RH) level , it is known that RH reduction leads to a higher membrane resistance ,thus, a lower proton conductivity in the catalyst layers while reducing the electrode kinetics [190]. However, high humidity levels may lead to water flooding, setting an upper limit at the RH value. When that happens water droplets prevent the flow of the gases through the channels. As a result, a rapid growth in mass transfer resistance occurs decreasing the performance of the fuel cell. A certain level of RH, near saturation (~80% RH) is suggested to achieve a high performance and it was chosen for our study [191]. The temperature effect was examined in the range of 40-80oC for optimization.

CHAPTER VI

6. RESULTS AND DISCUSSION

6.1. Break-in/Activation

Each single MEA underwent the same activation process to evaluate its performance improvement. As mentioned above, two activation steps were followed. At first, constant voltage (0.55 V) was applied to the fuel cell while the gases of were supplied to the anode and the cathode until stable current value was extracted (break-in). Following this, the voltage of the cell was cycled from 0.05 to 0.85 V at 100 mV/s until stable reproducible cycles. Before and after the activation procedure CV were performed at a scan rate of 50 mV/s between 0.05-1.2 V. Polarization curves were used to evaluate the MEA performance before activation process, after the constant voltage and eventually after the voltage cycling. From those polarization curves it can also be calculated the power density curve versus current density.

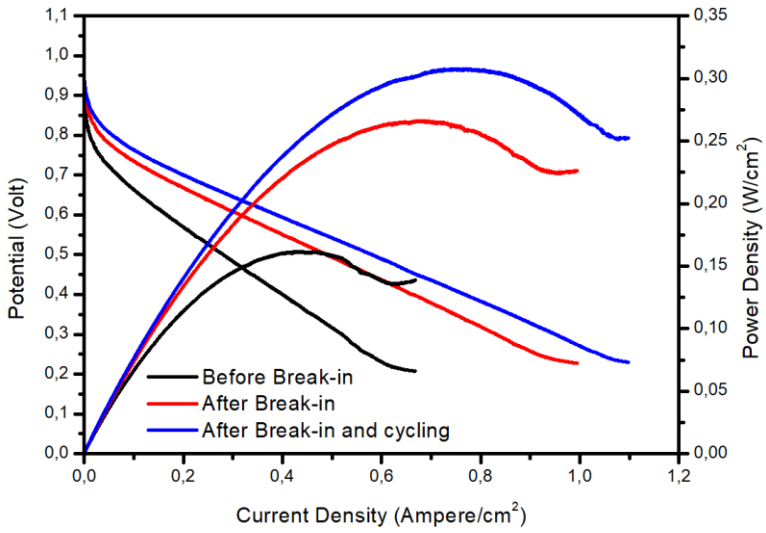

Figure 27. Polarization curves before break-in, after break-in, after break-in and cycling.

For example, polarization curves of MEA 1 are shown in **Figure 27** to make a comparison of the cell performance before and after each activation step. More specifically, **Figure *27*** displays the potential and power density as a function of current density throughout the activation process. The fuel cell was

considered broken-in when the current density stopped improving versus time. As shown in **Figure *27*** the MEA was activated after the break-in accomplishing a better performance which can be attributed to the hydration increase and the successful proton passage from anode to cathode [192]. The performance improvement (PI) was numerically compared as:

$$PI = \left(\frac{P - P_{initial}}{P_{initial}}\right) \times 100 \quad (34)$$

Where $P_{initial}$ is the initial power density at 0.55 V and P is the measured power density after the break-in. After constant voltage break-in procedure, the power density increased approximately by 65% while cycling process has a further power density increase about 15% resulting to a total ~90% increase due to the activation process. CV used to oxidize and detach the impurities of the MEA that are considered as manufacturing defects [193]. As a result, the effective electrochemical surface (ECSA) of the catalyst increases. CV technique was also used to calculate the ECSA. In **Figure 28,** the upper peak at approximately 0.18-0,33 V indicates the hydrogen desorption phenomenon (H_{des}) on the surface of the Pt electrode and the corresponding charge, while the lower peak at 0,15-0,28 V of the descending voltage sweep represents the adsorption phenomenon (H_{ads}).

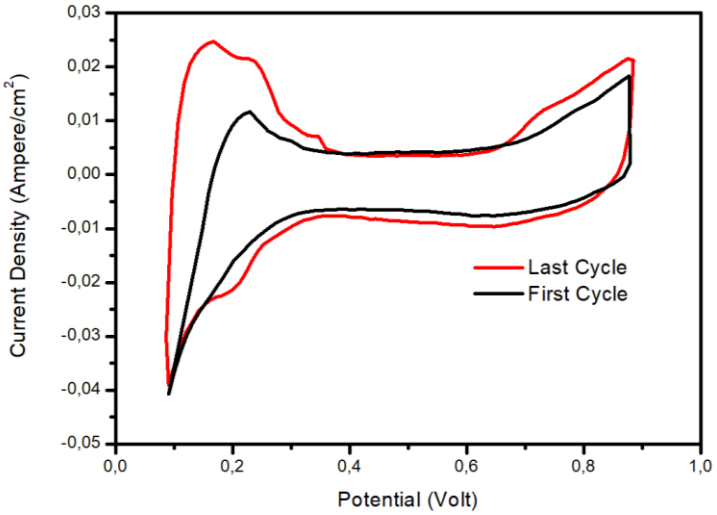

Figure 28. CV curves before and after conditioning at a scan rate of 50 mV/s.

Figure 28 shows differences of those areas with the increase of the cycles. At the final cycle the adsorption region was placed between 0,09-0,3 V while desorption area was placed between 0,098-0,36 V. As it can be seen, those areas are now bigger than before indicating larger scale of

adsorption/desorption. These areas, known as hydrogen region, are utilized for the calculation of the electrochemical active surface.

6.1.1. Electrochemical Active Surface Area (ECSA)

The desorption and adsorption charges are calculated by integrating the corresponding peaks as the charge transferring during the oxidation of Pt is closely relative to the hydrogen atoms desorbed.

$$H_{ad} \leftrightarrow H^+ + e^- \tag{35}$$

Theoretically, these two charges should be similar causing the same ECSA value. However, studies have shown that reversibility can only be considered in an ideal impurity-free electrolyte. Hence, the average area value of H_{des} and, H_{ads} will be used to calculate the total charge transfer and the electrochemical surface area (ECSA):

$$ECSA\left(\frac{cm^2}{mg}\right) = \frac{Q_H(\frac{\mu C}{cm^2})}{L(\frac{mg}{cm^2}) \times Q_{ML}(\frac{\mu C}{cm^2})} \tag{36}$$

Where Q_H is the average charge of Q_{ads} and Q_{des},, L is the metal load of the catalyst layer and Q_{ml} is the charge caused by the oxidation of a monolayer of H_2 per unit area. For Pt that value is set at 210 μC/cm^2 and 205 μC/cm^2 for Pd [194]. Following the above formula, the electrochemical active surface area before conditioning was calculated at 471,33 cm^2/mg while, after the conditioning, it was raised at 833,33 cm^2/mg. In accordance with the sources used above, this increasement was expected. From **Figure 29** it can be seen that the double layer charging region (0.4V to 0.6V) was increased, revealing that the double layer charging was increased.

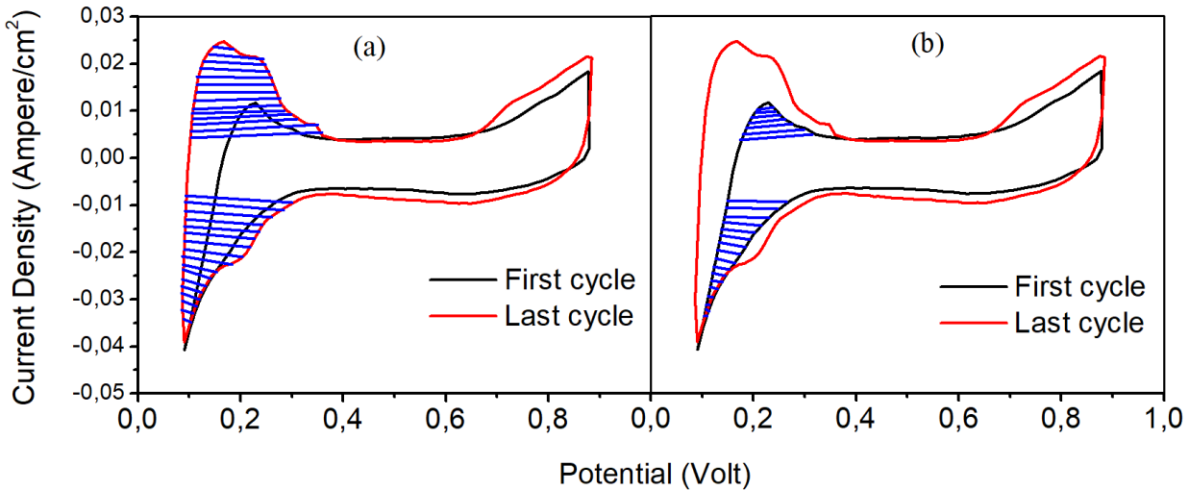

Figure 29. CV curves adsorption and desorption areas used at the first and the last cycle for the calculation of ECSA.

Moreover, the absolute value of the adsorption and desorption peaks were increased after the conditioning process. This means that the conditioning process conferred better electrocatalytic activity. For further information among the three polarization curves referred to each activation step an analytical model was used to calculate and evaluate the two main overpotential losses (activation and ohmic).

6.1.2. Polarization curves analysis

The mass transport overpotential losses, related to the limitation of the reactants concentration to sustain high current density values, can be neglected since the cell was constantly provided with high mass flow at both the anode and the cathode side and the higher limit of the potentiostat used which is around 1 A/cm^2 . To calculate the ohmic overpotential loss, we need first to calculate the ohmic resistance R_{ohm}. At medium current densities, ohmic overpotential losses rule the total losses, resulting to a closely linear overpotential loss. In that range of the I-V curve, the R_{ohm} can be extracted by the slope of the curve [195].Ohmic resistance was calculated by using a linear fitting method and the pseudo-linear section at middle range current density values as shown in **Figure 30**.The activation losses are dominant in low current density values and indicate the height of the activation barrier. Activation losses are mainly dominated by the slow ORR that occurs in the cathodic side.

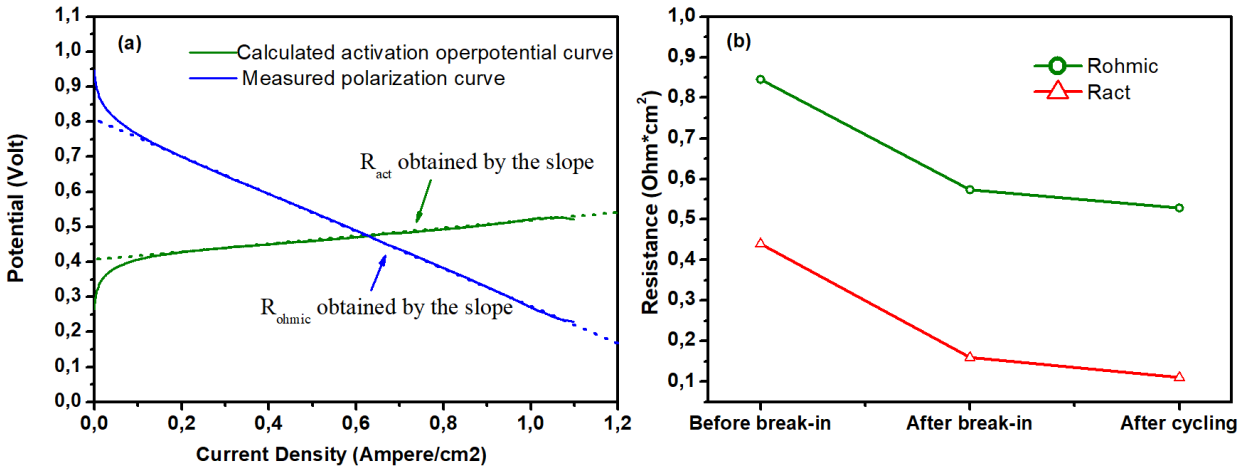

Figure 30. (a) Rohm and Ract obtained by pseudo-linear fitting, (b) Variation trends of Rohm and Ract during break-in steps.

Ohmic resistance R_{ohmic}, reduced step by step from 0.8452 $\Omega \cdot cm^2$ to 0.528 $\Omega \cdot cm^2$ with activation steps followed as the process increases the hydration level of the membrane. This downward trend was also followed by the activation resistance indicating a positive effect on the energy barrier of the ORR reaction, which was decreased from 0.43976 $\Omega \cdot cm^2$ to 0.11051 $\Omega \cdot cm^2$. This performance improvement can also be attributed to the increase of the ECSA. The performance gains are summarized in the following **Table 1**.

Table 1 : Performance results before break-in, after break-in and after cycling

	Power Density @0.6V (W/cm^2)	Current Density @0.6V (A/cm^2)	Max Power Density	R_{ohmic} ($\Omega \cdot cm^2$)	R_{act} ($\Omega \cdot cm^2$)	ECSA (cm^2/mg)
Before break-in	0.1	0.1667	0.1616	0.8452	0.4397	NaN
After break-in	0.18981	0.3165	0.2661	0.57316	0.16	471.33
After cycling	0.2327	0.38788	0.30772	0.528	0.1105	833.33

6.2. Effect of temperature

The single PEM fuel cell has been performed at different temperatures (40°C ,50°C ,60°C, 70°C,80°C) using Pt/C (20% wt.) as catalyst a layer in both the anode and the cathode electrodes, at constant RH~80%. Hydrogen and oxygen were fed at the anode and the cathode respectively while voltage swept from the maximum current density (~1.2 Ampere/cm^2) to open circuit voltage (OCV) value.

6.2.1. Polarization curves

I-V curves were used to characterize the effect of each operating temperature at the fuel cell performance. **Figure 31** shows the effect of temperature on the performance of the cell. As it was expected, the performance is improved at higher temperatures due to better membrane proton conductivity [196] and increased electrode kinetics for both the ORR and the HOR [197].

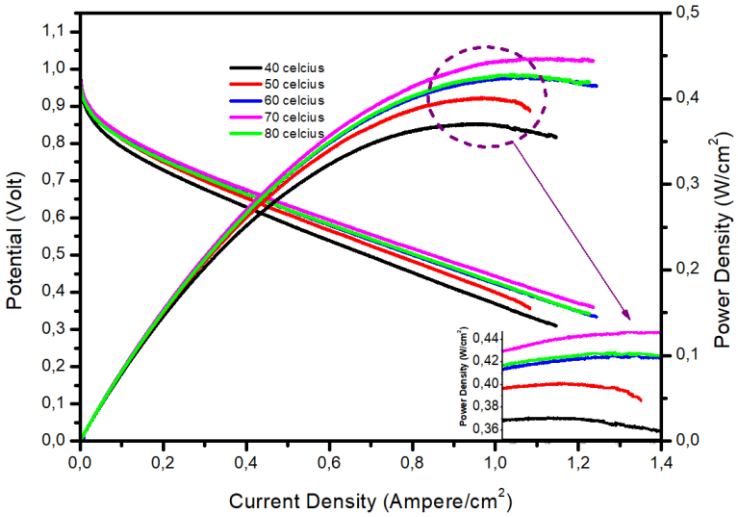

Figure 31. Effect of Temperature on fuel cell performance.

However, as it shown, the performance decreases above 70°C. That may be explained by the impact of the high temperature on a PEM fuel cell. High temperatures may cause the water inside the MEA and the anode/cathode to evaporate at a vast rate. As a result, a dehydrated MEA will cause reduced electrolyte conductivity and higher ohmic resistance while it can accelerate the degradation of components leading to decreased PEM lifetime. These disadvantages outflank the positive effects of improved kinetics, resulting to a mediocre overall performance [191][198]. These measurements were used to select the optimal operation temperature for our system. For this reason, all the experiments followed were conducted at 70°C.

6.2.2. Tafel analysis

However, the major effect of the temperature occurs in the activation part. That being the case, a Tafel approach has been selected to further investigate these losses.

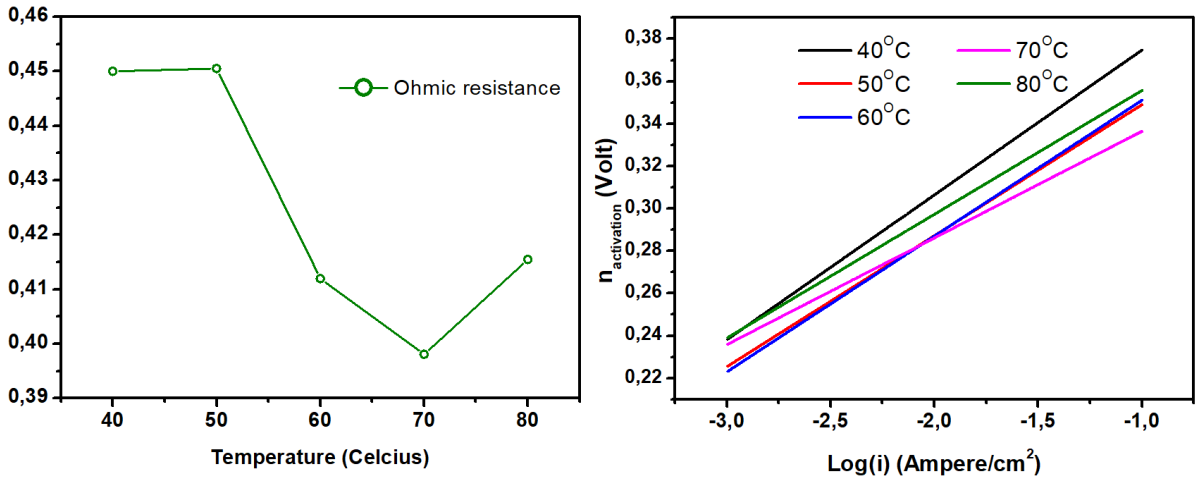

Figure 32. (a) Ohmic resistance versus temperature, (b) Tafel curves obtained from Tafel plots.

As shown in **Figure 32**, both the ohmic resistance and Tafel coefficients were quantified. Tafel slope is the main indicator of activation related losses while ohmic resistance is the main indicator of ohmic related losses. The results of that quantification are shown in **Table 2**.

Table 2: Fitted and calculated parameters at each temperature level.

Temperature	Fitted parameters			Calculated parameters
T (°C)	a (V)	b (mV/decade)	R_{ohmic} (Ω· cm^2)	i_o (A/cm^2)
40	0.44998	73.836	0.44	$8.255 \cdot 10^{-7}$
50	0.4175	70.282	0.43	$1.1761 \cdot 10^{-6}$
60	0.40205	67.876	0.41	$1.2232 \cdot 10^{-6}$
70	0.38844	65.89	0.39665	$1.3183 \cdot 10^{-6}$
80	0.38631	62.955	0.41	$7.49726 \cdot 10^{-6}$

As Ciureanu [199] and Husar et al. [150] has already found, the reduction on ohmic losses by differentiating temperature is small. On the other hand, the Tafel approach reveal more significant effect on activation losses. Specifically, Tafel slope seems to improve while temperature is rising indicating faster kinetic process, especially on cathode that dominates the activation overpotentials. Exchange current density (i_o) has found to be the most reliable indicator of activation losses. As it is shown in **Table *2***, exchange current density increases as temperature is rising. This positive effect of temperature is attributed to the increased thermal energy in the fuel cell that raises the chances of a reactant to own enough energy to hit the activated state [198]. Thus,

the improved reaction kinetics ,based on increased exchange current density, is the main reason for any potential gain related to the rising temperature [200].

6.3. Electrochemical characterization of anode catalysts

Platinum based on carbon, one of the most common catalyst layers at PEM fuel cell, was selected as the cathode catalyst to carry out all the experiments below, as it exhibits high ORR kinetics. Platinum alloys with palladium are mainly used to increase the CO tolerance of the anodic side. Before studying their behavior during H_2 pump mode, they are also studied at hydrogen fuel cell operation. Palladium has been used as its lattice structure is close to the Pt's lattice structure [201].

6.3.1. ECSA calculations

Thereby, cyclic voltammetry experiments were conducted to compare the electrocatalytic activity of three different catalyst layers at the anode, including Pt/C (0.2 mg_{pt/cm^2}), PtPd/C (0,04 mg_{PtPd/cm^2}) and $PtPd_3$/C (0,04 mg_{PtPd3/cm^2}) between 0,05 and 1.2 V at a scan rate of 50 mV/s (see **Figure 33**).

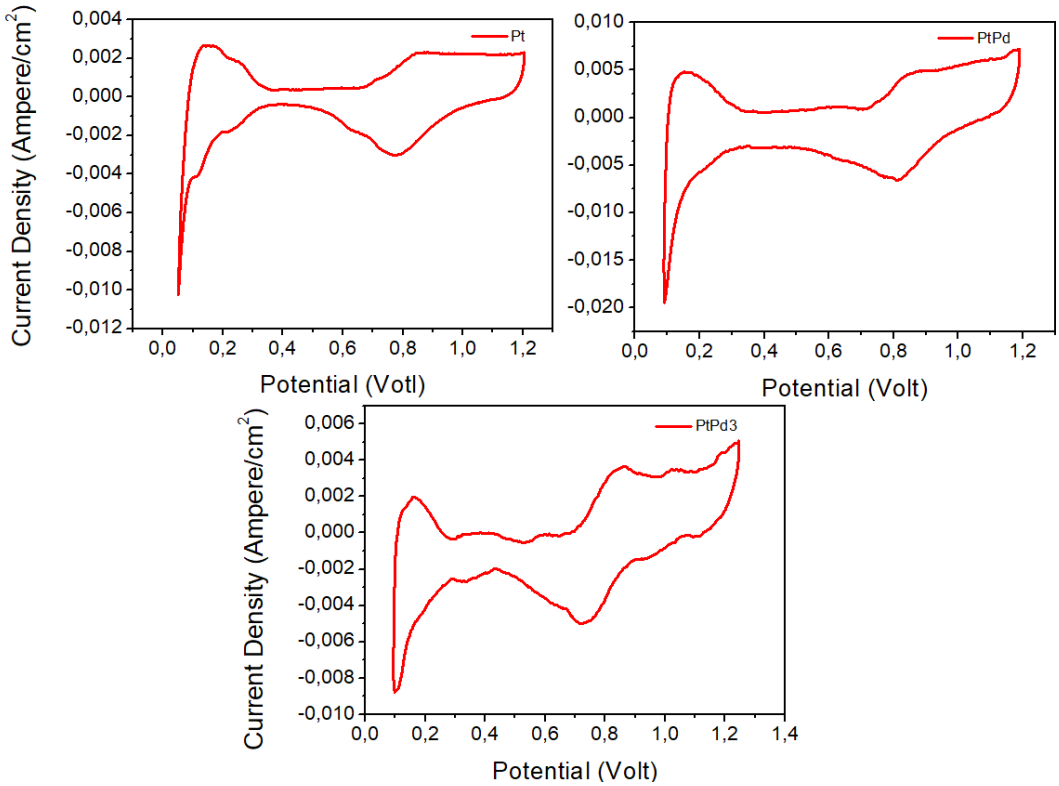

Figure 33. Cyclic voltammogram of (a) Pt/C, (b) PtPd, (c) $PtPd_3$.

The anode was fed with humidified H_2 while cathode was fed with humified N_2.

For Pt-Pd alloys the equation used was:

$$ECSA\ \left(\frac{cm^2}{mg}\right) = \frac{Q_H(\frac{\mu C}{cm^2})}{L(\frac{mg}{cm^2})\times(X_{pt}\times Qpt + X_{pd}\times Qpd)(\frac{\mu C}{cm^2})} \quad (37)$$

Where Xpt and Xpd are the atomic fractions of platinum and palladium respectively, Q_{pt} (=210 C/cm$^{2)}$ and Q_{pd} (=205 C/cm^2) are the charges as a consequence of a monolayer oxidation per unit area [194]. The electrochemical surface area for the three different catalyst layers is shown in **Table 3**.

Table 3: Electrochemical active surface area for Pt, PtPd, PtPd3

Electrocatalyst	ECSA (cm^2/mg)
Pt/C	833.33
PtPd/C	2890
$PtPd_3$/C	1370.42

It is calculated that PtPd/C has the highest electrochemical active surface area followed by $PtPd_3$/C. Some important parameters must also be considered to evaluate the catalyst layer activity such as mass transport losses, mass loading carbon particle sizes etc [202]. The three-catalyst layers tested have different mass loading values. The ECSA decrease with high metal mass loading could be explained by assuming that a large amount of metal blocking the pores and declining the gas permeability [203]. That may explain why PtPd and $PtPd_3$ presents higher electrochemical active surface area than Pt. Platinum based carbon catalyst used had 0,2 mg/cm^2 while the two alloys were having 0,04 mg/cm^2. The electrochemical characterization depending on CV can be enhanced by extracting qualitative data from the curves shown in **Figure 33**. It can be seen that all three catalysts follow a typical CV diagram. The voltammogram can be separated into three distinct parts, the hydrogen region where the hydrogen adsorption and desorption take place at low potential values, the double layer region, where no faradaic process occurs and eventually the oxidation region where surface oxides generated and reduced at high potential values [204]. The major differences from those CV graphs are based on (a)wider potential range of hydrogen desorption/adsorption peaks, (b)higher current result. More precisely, Pt/C shows lower absolute

value of H_2 adsorption peaks compared to PtPd/C and $PtPd_3$/C. The double-layer region is similar to all three catalysts (~0.4 to 0.6 V) indicating similar behavior. At high potential region the behavior of the three catalysts seems quietly the same. Oxide formation and reduction are occurring around 0.8 V while Pt/C shows the less impacted catalyst from this procedure. This may be explained by the fact that Pt has theoretically the highest ORR activity among other noble metals including Pd [205],[206].

6.3.2. Polarization curves

Polarization curves were also used for further electrochemical performance characterization of the three anode catalysts tested in this work, Pt, PtPd, $PtPd_3$. According to the literature Pt's performance is really good for the oxygen reduction reaction when it is utilized as cathode catalyst layer. Similarly, the performance of Pt for the hydrogen oxidation reaction acting as anode catalyst layer, is considerably high [207]. During the following measurements the performance conditions were the same for each catalyst while the anode was fed with humidified H_2. **Figure 34** presents both the polarization and power density curves of each catalyst. All three polarization curves are in accordance with the general theoretical curve. They can be separated into three different regions depending on the main voltage loss mechanism: (a) activation, (b)ohmic [208] .

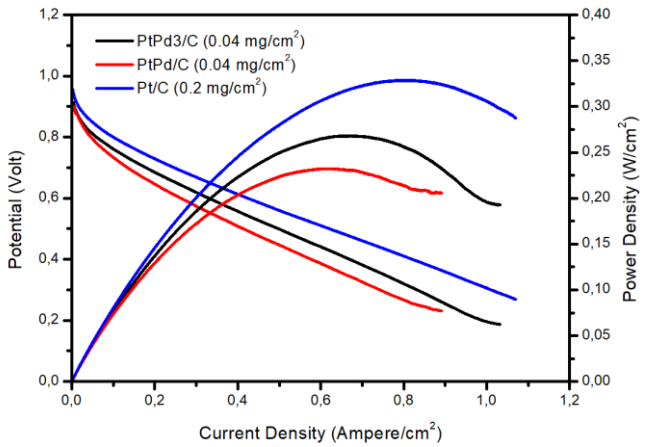

Figure 34. Performance curves on pure Hydrogen with anode catalysts consisting of carbon supported Pt, PtPd, $PtPd_3$.

This region is called the concentration polarization region and it is not shown in **Figure 34** as the cell was constantly provided with high flow rate gasses [209]. The activation region is located at

potentials above ~0.85 V while for both $PtPd_3$/C and PtPd/C the activation region is detected above ~0.8 V. This may be an indication for higher activation energy required for the reaction at $PtPd_3$ and PtPd layer surface. The slope of Pt/C polarization curve, at the ohmic losses region, compared to the other two catalysts, may also be a sign of lower MEA resistance. Besides those, quantitative information, extracted from the polarization and power curves, numerical data can also be extracted. The performance of each catalyst at 70°C is shown in **Table 4**.

Table 4: Performance test results with H2/O2 at 70°C

Catalyst	Power density at 0,6V (W/cm^2)	Current density at 0.6V (A/cm^2)	Max power density (W/cm^2)	R_{ohmic} ($\Omega \cdot cm^2$)
Pt/C	0.2544	0.4241	0.32875	0.5105
PtPd/C	0.158	0.2632	0.23233	0.6358
$PtPd_3$/C	0.1985	0.3308	0.26811	0.5871

As seen from **Table 4**, power densities and current densities at 0.6V of the Pt/C, PtPd/C and $PtPd_3$/C were determined as 0.2544, 0.158, 0.1985 W/cm^2 and 0.4241, 0.2632, 0.3308 A/cm^2 respectively. The maximum power densities were found to be 0.32875, 0.23233, 0.26811 W/cm^2 respectively. Those result values are considered adequate, this is explained as an optimization process of Temperature had already taken place. As it was mentioned before, metal loading plays an important role on the PEM fuel cell performance. When high platinum loading is used, there is a fast reaction rate for ORR resulting improved performance [202]. This is the main reason that pure platinum catalyst presents that high power and current density values. This difference on metal loading among the three catalysts makes the comparison of those three difficult. For that purpose, specific activity curves should be introduced. Over the past few years, scientists have tried to use thinner membranes without having significant current density losses. This lead to lower metal loading used at each MEA [210]. The current density curve of each catalyst was divided by the respective mass loading and the resulted mass activity curves are presented in **Figure 35**. One could maximize the performance of a PEM fuel cell that use a thin film electrode by increasing the catalyst concentration.

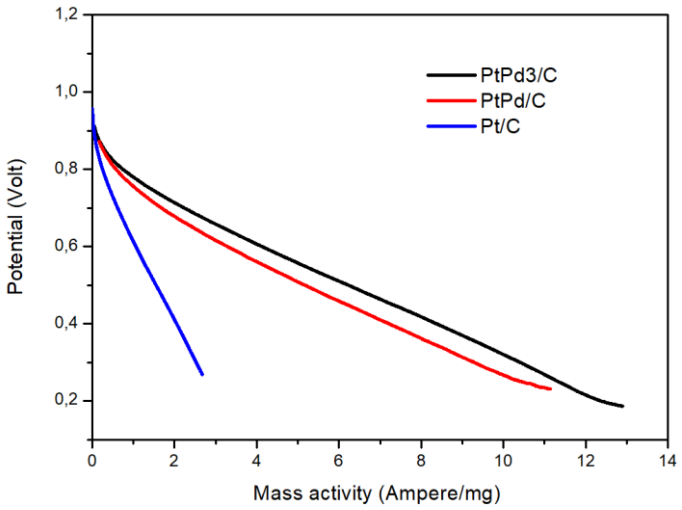

Figure 35. Comparison of cell voltages against mass activity for (a)PtPd3/C, (b)PtPd/C, (c)Pt/C.

Figure 35 shows the voltage losses against mass activity. Having said that, $PtPd_x$ (x=1,3) alloys catalysts, with less catalyst concentration, clearly presents higher mass activity of platinum as catalyst. This may have an impact on further study to replace the high-costed platinum catalyst with platinum/palladium alloys.

6.4. HYDROGEN PUMP CELL

For the following experiments the cell was used with either pure hydrogen or hydrogen containing carbon monoxide at the cathode, which still plays the role of WE and pure hydrogen at the anode which play the role of RE, and CE used as DRE. This layout is called hydrogen pump mode (also known as proton pump) [152]. The symmetrical hydrogen cell is mainly used as H_2 purifier or compressor but also as a research tool. Here, the anodic hydrogen oxidation reaction (HOR) takes place at the WE while the hydrogen evolution reaction (HER) takes place at the RE and CE, resulting the passage of the hydrogen protos through the membrane to the cathode where they are reduced. (See **Figure 36**)

$$\text{Hydrogen Oxidation Reaction (HOR):}\quad H_2 \rightarrow 2H^+ + 2e^- \qquad (38)$$

$$\text{Hydrogen Evolution Reaction (HER):}\quad 2H^+ + 2e^- \rightarrow H_2 \qquad (39)$$

The tests were executed potentiostatically to monitor the anodic behavior.

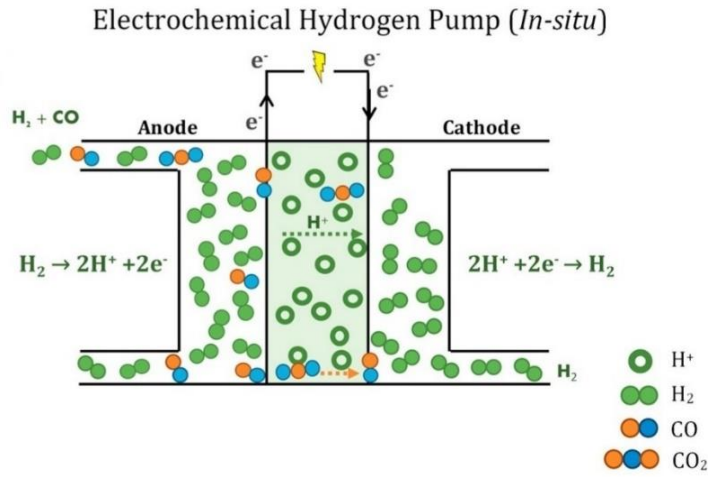

Figure 36. Illustration of a cell operating in hydrogen pump mode [211].

This setup has proved to be a very efficient way to study the conditions and the impact of carbon monoxide poisoning on a single cell for two main reasons. Firstly, no masking effect of cathode is occurred as the slow kinetics of the ORR is avoided by using hydrogen instead of oxygen at that side of the cell. The HER presents fast cathode kinetics with low overpotential, for that reason cathode has slight effect on the voltage-current curve allowing to monitor mainly the anodic behavior [212-214]. Secondly, there is no reaction producing water in the cathode, permitting the full control of the gas humidification level on both sides. Water management is one of the main factors that affect the total performance of a PEM fuel cell as surplus water cover some of the catalytic sites resulting low performance [212]. In this work, carbon monoxide effect is the main purpose of investigation and therefore any other degradation mechanism including water flooding must be excluded.

6.5. CO POISONING

The primary objective of this work is to examine the performance and the tolerance of carbon monoxide for different carbon-supported catalysts. We will compare the CO tolerance of PtPd alloys composed of different atomic fractions (Pt_1Pd_1, $PtPd_3$) and Pt at two different mass loading (0.2 mg/cm^2, 0.04 mg/cm^2). To define the most tolerant catalyst under CO poisoning effect, the electrocatalyst's ability to oxidize CO adsorption at low potential, while the hydrogen oxidation ratio remains almost the same, must be further studied. For that purpose, current-voltage (I-V) were carried out to examine carbon monoxide adsorption and oxidation behavior. This graph reveals the dependence between the potential

and the carbon monoxide adsorption/oxidation. In addition to that, electrochemical impedance spectroscopy (EIS) measurements were also used to study some functional parameters. More specifically, an equivalent circuit consisted of resistances and capacitances was used. Those resistances were found to change according to the CO adsorption/oxidation, so they can be used for poisoning reading. To conduct those measurements, the system must be stable. In this direction, chronoamperometry was used to monitor the stability of the system at 0.2 V. In **Figure 37** the resulted graph, using $PtPd_3/C$ as anodic catalyst layer, is presented:

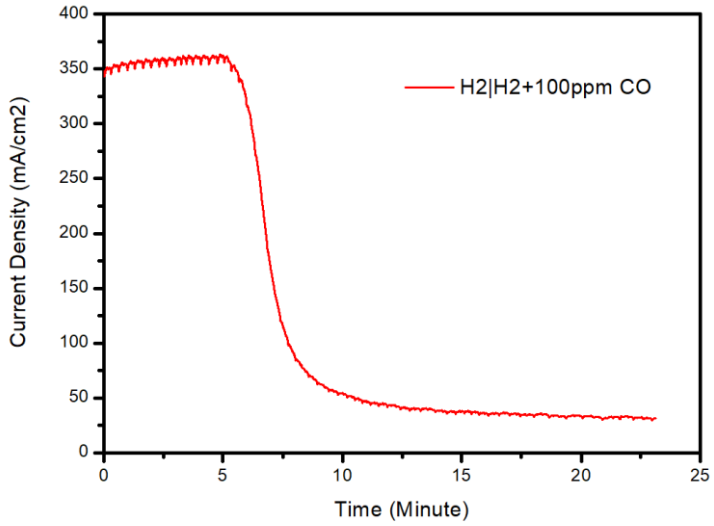

Figure 37. Chronoamperometry curve at 0.2V while H2 supplied at reference electrode and H2/100ppm CO supplied at working electrode.

After purging both the anode and the cathode electrodes with pure hydrogen for 5 mins, resulting a stable current density around 350 $mA/cm^{2,}$ the mixture of gases that contain 100 ppm of CO was injected into the fuel cell. Consequently, the current density was dropping sharply indicating that cell performance was affected. As it is shown the system reached at the desired steady state after 10 mins of a transitional period.

6.5.1. Anode polarization in the presence of CO

Taking platinum catalyst as a reference, carbon monoxide and hydrogen oxidation mechanism has been analyzed in **Section 3.2. Working principles of PEMFC** and **Section 3.5. Poisoning mechanism**. Hydrogen oxidation on platinum catalyst surface is happening in two major steps. First the adsorption of the hydrogen and then the oxidation of the adsorbed hydrogen. The adsorption of

hydrogen requires two bare platinum catalyst sites. The overall electro-oxidation of the adsorbed hydrogen results two bare platinum sites, two positively charged H_2 atoms and two electrons. On the condition that pure hydrogen was supplied, those two steps evolve very fast succeeding high current density [215]. However, when the hydrogen, as a reformed product, contains even a few amounts of carbon monoxide there are significant performance losses because of the Pt poisoning. More precisely, a contest between H_2 and CO takes place for adsorption of platinum electrochemical active sites. Even so, CO is winning that contest as the Gibbs energy of CO adsorption on platinum-based catalyst is lower than H_2 leading to limited bare platinum sites. The adsorbed carbon monoxide can be removed by oxidizing it. Generally humidified gases and mixture of gases provide water molecules at each electrode side. Those molecules are conveniently oxidized at Pt free sites, producing hydroxyl molecules that react with the adsorbed CO giving CO_2 as presented below [216]:

$$Pt - OH + Pt - CO \rightarrow 2Pt + CO_2 + H^+ + e^- \quad (40)$$

As a result, the total polarization performance of a catalyst layer is a combination of CO adsorption and CO removal by oxidizing it. When a Pt-M alloy catalyst is used, the reaction of CO adsorbed oxidation differs from this on platinum surface. In general, it is found that an added M could favorize the oxidation of CO and eventually its removal. The added M can activate the formation of oxygen-containing species (OH) from water. This leads to the adsorption of OH on the catalyst surface that lowers the onset potential of carbon monoxide potential. In other words, alloying Pt with some other metals change the electronic structure of platinum and weakens the formation of Pt-CO [217].

$$M + H_2O \rightarrow M - OH_{ads} + H^+ + e^- \quad (41)$$

$$Pt - CO + OH - M \rightarrow Pt + M + CO_2 + H^+ + e^- \quad (42)$$

The polarization curves for H_2/CO gas mixture are shown in **Figure 38.**

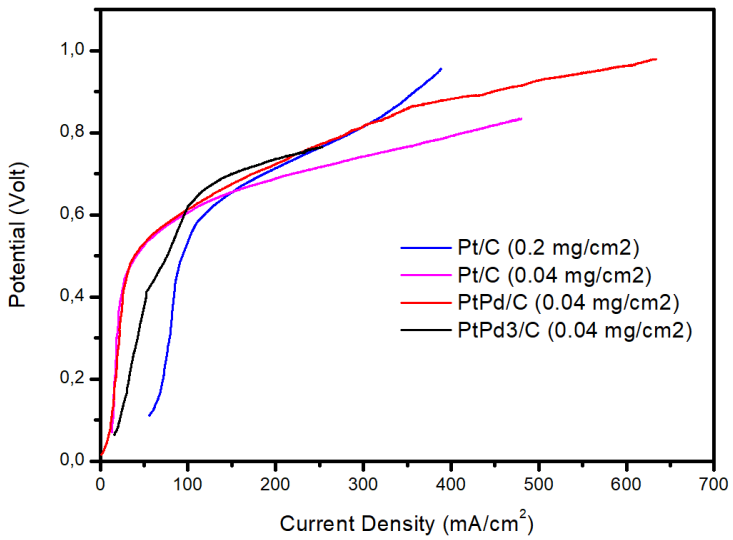

Figure 38. Polarization curves for the oxidation of 100 ppm CO in hydrogen on different catalysts.

Based on the above electrochemical processes of hydrogen and carbon monoxide adsorption/oxidation, those curves are analyzed. At low potential and low current density values, the electro- oxidation is mainly controlled by hydrogen oxidation on the free of adsorbed carbon monoxide catalyst surface. However, those low current density values extracted indicate that this surface is extremely reduced by CO poisoning. At those potential values only a few amounts of adsorbed CO can be oxidized and liberate Pt sites for H_2 oxidation. This stage lasts until the potential value reach ≈0.6 V, where the electro-oxidation is starting to get dominated by CO_{ads} oxidation. As explained before, in this stage the CO that was already adsorbed, is oxidized by the hydroxyl molecules releasing more and more free catalyst surface. As a result, the current density can now be improved by only a few overpotential increase. All polarization curves of the four catalysts are in accordance with those steps. Pt/C with a higher mass load (0.2 mg/cm^2) seems to be the most CO-tolerant catalyst as it presents higher current density values. That might be explained by the higher mass-load used as more Pt sites were free for oxidation reaction to take place. For that purpose, higher mass-load is used to reduce co poisoning effect [218] . Among the rest of the catalysts with same mass loading, $PtPd_3$ shows the higher CO tolerance as it produces higher current density indicating more free catalyst sites for hydrogen oxidation. However, $PtPd_3$ also reveals a drawback for this catalyst layer. $PtPd_3$ seems to need higher potential values to oxidize and remove adsorbed CO by hydroxyl

species. This means, higher energy level needed to convert CO into CO_2 and remove it, liberating more catalyst sites. PtPd/C at 0.02 mg/cm^2 and Pt/C at 0.02 mg/cm^2 present similar behavior at low potentials, while at higher overpotential PtPd/C tends to copy $PtPd_3$/C behavior needing more energy to remove CO. Those indications reveal that at same mass loading catalyst $PtPd_3$/C was the most CO-tolerant catalyst, while high mass loading significantly improves the catalyst behavior during CO poisoning phenomenon.

6.5.2. EIS of CO poisoning at open circuit voltage (OCV)

The conclusions of the latter paragraph are yet to be confirmed by EIS measurements. Once the system is again stabilized EIS measurements were carried out at the same conditions that polarization curves were executed. For that purpose, an equivalent electric circuit consisted of several resistances, must be introduced. At this work, the equivalent circuit model (EEC) for open circuit voltage (OCV) is consisted of two Randle's cell, one referring to the charge transfer and the second one referring to the H_2 adsorption as shown below in **Figure 39**:

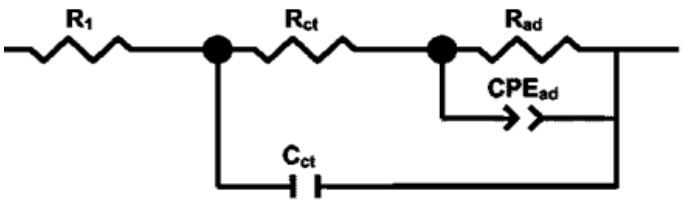

Figure 39. Equivalent circuit of fuel cell fed with H2/H2+CO.

Here R1 represents the ohmic resistance, R_{ct} and C_{ct} represents the high frequency (hf) arc, R_{ad} and CPE_{ad} represents the low frequency (lf) arc. To describe the lf arc, constant phase element (CPE) has been used. CPE is defined by two parameters:

$$Z_{CPE} = 1/T(j\omega)^n \quad (43)$$

Where ω is the angular frequency (ω=2πf) of the voltage and n is a constant. More specifically, if n =0 then CPE is a resistance (R), if n=1 CPE is a capacitance (C), if n=0.5 CPE is a warburg impedance (W) and if n=-1 it is an inductance (L). CPE is mainly used to describe a non-homogenous phenomenon. This equivalent circuit presents two superimposed arcs, that they are to be distinguished

in the Nyquist plot, corresponding to the charge transfer resistance and adsorption resistance respectively. The arc in the hf region is therefore ascribed to the oxidation step of hydrogen (H_{ads}= H + e^-) and the arc in the lf region is ascribed to the adsorption of hydrogen (H_2=H_{ads}). The overall impedance of the equivalent system can be calculated by summarizing the individual impedance of the three resistances. The intercept point with the real axis of the Nyquist plot at the hf region (R_{hf}) is attributed to the ohmic resistance of the cell (R_1), while the intercept point of the Nyquist plot with the real axis at the lf region (R_{lf}) is attributed to both charge transfer and adsorption phenomena. At the following EIS measurements, the impedance spectra for different CO concentrations, different temperatures and different catalyst material were all fitted to the equivalent circuit. **Figure 40** show the complex impedance results at 70°C for different CO concentration.

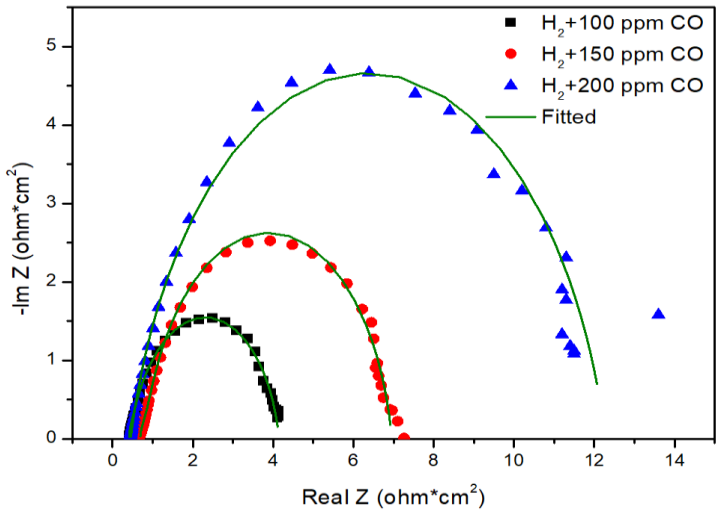

Figure 40. Complex impedance of $PtPd_3$ (0.04 mg/cm^2) using H_2 with different level of CO concentration at OCV and 70°C, operating at hydrogen pump mode.

At first glance, the higher the tested CO concentration, the larger the diameter of the arc. **Table 5** shows the values of the parameters extracted using the equivalent circuit. As it is presented, the rate-determining resistance of the three is the one referred to adsorption. As the CO concentration is increasing from 100 ppm to 200 ppm the R_{ad} is increased from 3.1998 (Ω·cm^2) to 11.831 (Ω·cm^2) respectively. The resistance R_1 which is mainly attributed to the membrane is seems to not be constant although the temperature remains the same for all three tested concentrations. This may be ascribed on membrane humidification fluctuations.

Table 5: Resistances of EEC for fitting impedance curve at different CO concentration during hydrogen pump mode.

	100 ppm		150 ppm		200 ppm	
	Value (ohm·cm^2)	Error (%)	Value (ohm·cm^2)	Error (%)	Value (ohm·cm^2)	Error (%)
R_1	0.41174	0.00038147	0.69122	0.00022888	0.42174	0.016098
R_{ad}	3.1998	7.629E-05	5.7581	7.629E-05	11.831	0.0029755

It may be concluded that higher CO concentration level leads to higher CO coverage on catalyst making the hydrogen adsorption on a free catalyst site more difficult to happen. The CO concentration seems to be proportional to the total impedance of the cell. New techniques have been developed to reduce the CO concentration on hydrogen produced by reforming hydrocarbons, but still traces of CO are present. For the next two tests, the CO concentration that will be used is set at 100 ppm. In this way, we will examine whether the temperature affects the impedance of the cell during CO poisoning or not.

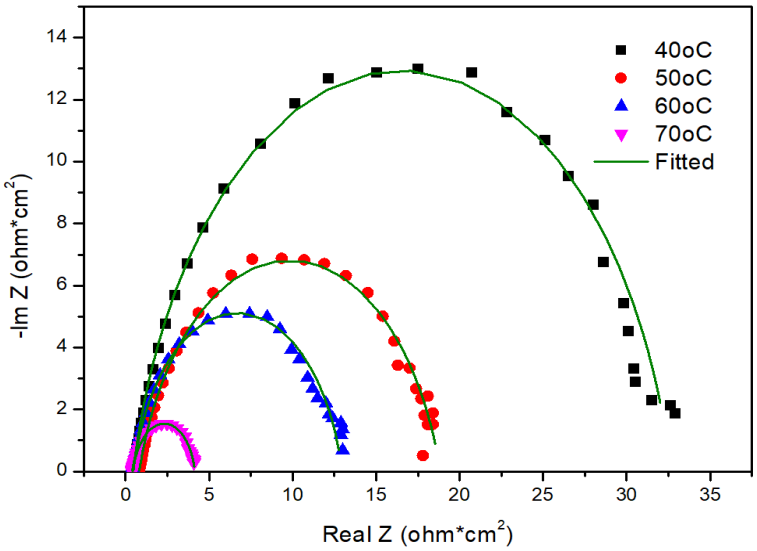

Figure 41. Complex impedance plot of PtPd3 (0.04 mg/cm2) using H2+100 ppm CO at different operating temperatures, at OCV, operating at hydrogen pump mode.

More specifically, **Figure 41**, show the complex impedance results under 40^{o}C,50^{o}C,60^{o}C and 70^{o}C respectively while 100 ppm of CO is supplied at the cell working at hydrogen pump mode. The anode catalyst that was used for all the temperatures was PtPd3/C (0.04 mg/cm^2). CO

adsorption on the electrocatalyst, which is the rate determined phenomenon, is an exothermic reaction meaning that higher operation temperature reduces the CO_{ads} coverage [219].

The temperature effect on a PEM fuel cell during CO poisoning can therefore significantly affect the performance of the cell. Many studies have already been done to examine this behavior. R Jiang et al have studied the performance losses of a PEM fuel cell operating at 105ºC and 120ºC fueled by hydrogen that contains small amount of CO [219], while Li et al used a phosphoric acid-doped PBI membrane to study the temperature range between 125 and 200ºC [215]. All these studies concluded that high operating temperature diminish the performance losses. In this work, a similar behavior is also observed at lower temperatures. In **Figure 41** the distance between the two intersection points R_{LF}-R_{HF} is getting bigger as the operating temperature falls, meaning that the total impedance of the system is increased. In following **Table 6**, the values of R_1, R_{ct}, R_{ad} and their corresponding errors are presented.

Table 6: Resistances of EEC for fitting impedance curve at different temperature during hydrogen pump mode.

	40ºC		50ºC		60ºC		70ºC	
	Value	Error (%)	Value	Error (%)	Value	Error (%)	Value	Error (%)
R_1	0.48466	2.4354	0.4955	0.01976	0.4168	0.00038	0.4117	0.00038
R_{ad}	28.985	0.09651	18.022	0.00114	11.772	0.00038	3.1998	7.6E-05

As it can be seen, both the internal resistance and the resistance that refers to the hydrogen adsorption on catalyst sites are being reduced while the temperature is rising. The R_{ad} is 28.985 $\Omega \cdot cm^2$ and 3.1998 $\Omega \cdot cm^2$ at 40ºC and 70ºC respectively. Followingly, four different catalysts will be used to investigate their corresponding tolerance at CO poisoning. For that purpose, the four catalysts that were previously used to extract the anodic polarization curves, are now used to extract their corresponding impedance plot. Platinum, which is found to be the most efficient catalyst for HOR is lacking tolerance upon CO poisoning. However, some platinum alloys have found to have higher CO tolerance, including platinum-palladium alloys. **Figure 42** presents the complex impedance plot for each catalyst at OCV while 100 ppm of CO is also fed at the anode during operation at hydrogen pump mode.

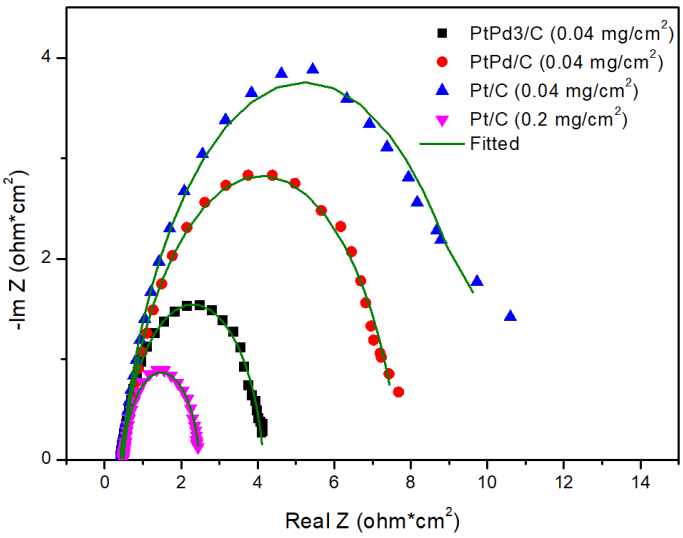

Figure 42. Complex impedance plot at OCV and 70oC for different anodic catalysts, operating at hydrogen pump mode.

As it can be seen Pt/C with 0.04 mg/cm^2 mass loading presents the bigger arc. However, Pt/C at high mass loading (0.2 mg/cm^2) presents the smallest arc among the four tested catalysts. This is partially explained by Yuan et al, who suggested that higher catalyst loading leads to a higher number of available catalyst sites [220]. Consequently, more free sites are available for hydrogen adsorption.

Pt-Pd$_x$ (x=1,3) alloys show less wide arc at medium frequencies indicating higher hydrogen electro-oxidation activity than pure platinum catalyst. Therefore, PtPd and PtPd$_3$ exhibits higher CO tolerance at same mass loading however pure platinum catalyst layer with higher mass loading leads to more bare sites of platinum where platinum oxidation may occur at the same CO concentration. At the following **Table 7** numerical data are also presented.

Table 7: Resistances of EEC for fitting impedance curve using different anodic catalyst during hydrogen pump mode.

	Pt/C (0.2 mg/cm^2)		PtPd/C (0.04 mg/cm^2)		PtPd$_3$/C (0.04 mg/cm^2)		Pt/C (0.04 mg/cm^2)	
	Value	Error (%)	Value	Error (%)	Value	Error (%)	Value	Error (%)
R_1	0.49845	0.00038	0.47997	0.62126	0.41174	0.00038	0.44615	0.32173
R_{ad}	1.9716	0.00053	6.5652	0.11131	3.1998	7.62E-05	9.585	0.51964

As it can be seen, R_1 remains almost the same (0.45 ± 0.5) for all four catalysts. This may be ascribed to the direct connection between temperature and the relative humidity. Humidity strongly affects the ionic resistance, which dominates R_1. R_{ad}, which is the rate determining phenomenon reveals the most CO tolerant catalyst. The lower the value of this resistance, the

most tolerant on CO poisoning the catalyst is. Having said that, we can arrange the four catalysts in series, from the most affected catalyst to the least affected one.

Pt/C (0.2 mg/cm^2) < $PtPd_3$ (0.04 mg/cm^2) < $PtPd/C$ (0.04 mg/cm^2) < Pt/C (0.04 mg/cm^2)

6.5.3. PtPd3/C anodic catalyst poisoning

As it was found in the last two paragraphs and the corresponding experiments, $PtPd_3/C$ was found to show the highest CO tolerance among the other two tested catalysts with the same mass loading. Pt/C at higher mass loading seems to have greater both electro-oxidation activity and CO tolerance. However, higher mass loading catalysts requires also higher cost of catalyst production. This is the reason why $PtPd_3/C$ is selected to exhibit the following CO poisoning measurement, as the practical use and the production of the catalyst should also be taken into account. **Figure 43** compares the performance of the fuel cell providing pure H_2 as fuel and a mixture of H_2/100 ppm CO to simulate reformatted hydrogen at 70°C. The massive effect of CO presence is clearly shown. Significant potential losses are evident when reformatted hydrogen with CO is supplied. The adsorption and oxidation kinetics for CO that were analyzed above, create this severe effect. Even though, the most CO tolerant catalyst was already tested and selected, the CO poisoning effect still provoke insufficient performance activity at 100 ppm CO.

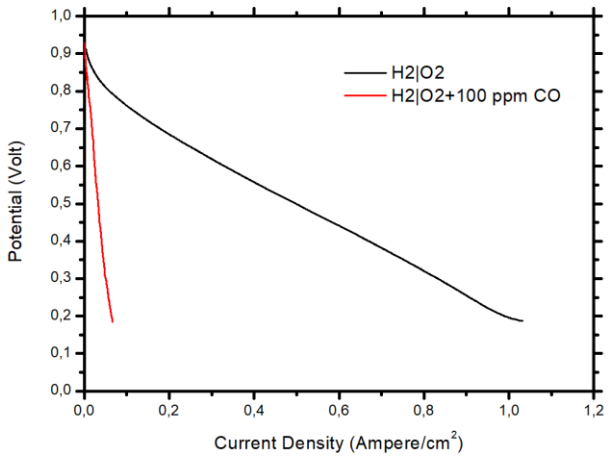

Figure 43. Comparison of cell polarization between supplying pure hydrogen and mixture of hydrogen/100 ppm CO.

This result indicates that further research must be made to reduce the CO presence effect at the fuel cell operation. The usage of Platinum alloys is proposed as one of the main ways to achieve it.

However, in this work, the use of a more CO tolerant catalyst showed unacceptable performance, which can also be attributed to the low mass load catalysts. It is why, mitigation methods should be developed and used after the usage of reformatted hydrogen. Some researchers have proposed that CO poisoning effect can significantly be reduced by operating the cell at even higher temperatures (>100^{o}C) or higher pressure, but that may result the durability of the membrane used. Gottesfeld and Pafford have suggested that the CO poisoning problem of a PEM fuel cell operating at low temperatures can partially be solved by providing 1-4% of oxygen at the anode side, this is known as oxygen bleeding [221]. The presence of oxygen while carbon monoxide covers the catalyst site will lead to an oxidation process that liberate some catalyst sites.

CHAPTER VII

7. CONCLUDING REMARKS

In this work, four different catalysts were used at the anode of a PEM fuel cell to examine their CO tolerance. Pt, which is the most used noble-metal catalyst for ORR, was used at cathode for all the measurements. At first, the cell performance had to be optimized. For this reason, a two-step activation process had to be employed, to increase the MEA hydration level and reach the peak performance of the cell. The chosen activation process increased the Power Density of the cell by 90%, reaching 0.266 W/cm^2 at 0.55 V. In addition, the optimal working temperature had to be determined. The temperature of a cell directly affects the hydration level of the MEA and eventually the performance of the cell. The cell operated at 40,50,60,70 and 80^{o}C respectively. Tafel analysis showed that the rise of the temperature had a positive effect on the activation voltage losses as the Tafel slope (b) found to be decreased, while the exchange current density (i_o) was increased. However, it was found that the ohmic losses of the cell could no longer be improved above 70^{o}C. Therefore, 70^{o}C was found to be the optimal working temperature of our system. Subsequently, three different anodic catalysts (Pt/C at 0.2 mg/cm^2, PtPd/C and $PtPd_3$/C at 0.04 mg/cm^2) were used to examine the total cell performance while pure hydrogen and oxygen were supplied at the anode and the cathode respectively. Pt/C at 0.2 mg/cm^2 showed the highest performance among the three catalysts hitting 0.4241 W/cm^2 at 0.6 V.

For the examination of CO poisoning effect at the anodic catalyst, the corresponding measurements were done while the PEM fuel cell was operating at hydrogen pump mode. During the hydrogen pump mode, the masking effect of the cathode reaction was avoided. Therefore, the impact of the CO poisoning effect at the HOR can easily be distinguished. To carry out the following experiments, the system must firstly be stabilized. Pt/C at 0.04 mg/cm^2 and the three

catalysts that mentioned above were used to investigate the carbon monoxide effect at the anode. Anode polarization shows that platinum at high mass loading concentration and $PtPd_3$/C at low mass loading concentration presented higher current density values at low potential (below 0.6V) than the PtPd/C and Pt/C at low mass loading concentration. This indicates that the two former catalysts had more free catalyst sites for hydrogen adsorption and oxidation. This is the reason that they considered to be more tolerant at the carbon monoxide poisoning effect. Moreover, the CO effect was also investigated by using electrochemical impedance spectroscopy measurements at OCV. To analyze the EIS measurements results, an equivalent circuit model was introduced. This circuit includes the two main steps of hydrogen adsorption and oxidation. At a specific temperature, higher impedance was presented at high CO concentration level due to the increased number of CO_{ads} catalyst sites, while for a specific CO concentration higher temperature presented smaller arc at complex plot. The CO adsorption is an exothermic step reaction and therefore it is directly affected by the temperature, resulting lower impedance for hydrogen adsorption. Lastly, the four catalysts were used at a certain temperature and CO concentration level. The results are in accordance with the anode polarization conclusion. The impedance curves of $PtPd_3$ and Pt at high mass loading observed to be the smallest, while the other two catalysts presented higher impedance.

REFERENCES

1. J. R. Bradley. Fuel and Power in the British Empire, US Government Printing Office, 1935.

2. T. Shair. An Age of Petroleum: Anglo-American Foreign Policy and the Rise of Nationalism in Iran. *The Mirror-Undergraduate History Journal 42 (1)*,16-28, 2022.

3. R. Vernon. Oil Crisis. W.W. Norton and Co. Inc., New York, 1976. DOI:https://doi.org/10.2307/2148587

4. E. F. Camacho, T. Samad, M. Garcia-Sanz, I. Hiskens. Control for renewable energy and smart grids. *The Impact of Control Technology, Control Systems Society 4 (8)*, 69-88, 2011.

5. C. A. Horowitz. Paris agreement. *International Legal Materials 55 (4)*, 740-755, 2016. DOI: https://doi.org/10.1017/S0020782900004253.

6. M. Ram, M. Child, A. Aghahosseini, D. Bogdanov, A. Lohrmann, C. Breyer. A comparative analysis of electricity generation costs from renewable, fossil fuel and nuclear sources in G20 countries for the period 2015-2030. *Journal of Cleaner Production 199*, 687-704, 2018. DOI:https://doi.org/10.1016/j.jclepro.2018.07.159.

7. L. Mchugh. World Energy Resources Coal. *London, England: World Energy Council*, 2016.

8. R. E. Hester, R. M. Harrison. Energy Storage Options and Their Environmental Impact, Royal Society of Chemistry 46, 2018. DOI:https://doi.org/10.1039/9781788015530-FP001.

9. K. S. Deffeyes, M. P. Silverman. Hubbert's peak: the impending world oil shortage. *American Journal of Physics 72*, 126, 2004. DOI:https://doi.org/10.1119/1.1636165.

10. M. R. Simmons. Is the world supply of oil and gas peaking?. *London World 10 (2)*, 46, 2007.

11. D. Cohen. Are we in the post-peak era?. ASPO-USA, 2009.

12. D. Bodansky. Nuclear energy: principles, practices, and prospects (2nd ed.). Springer Science & Business Media, 2004.

13. C. Allardice, E. R. Trapnell, E. Fermi, L. Fermi, R. C. Williams. The First Reactor, 40th Anniversary (rev.). US Atomic Energy Commission (AEC); DOE Office of Nuclear Energy; DOE Office of Management and Administration, 1982.

14. J. Twidell. Renewable energy resources (4th ed.), Routledge, 2021. DOI: https://doi.org/10.4324/9780429452161.

15. I. Dincer, M. A. Rosen. Chapter 4 - Exergy, environment, and sustainable development. Exergy 2nd edition, pp. 61-89, 2021. DOI: https://doi.org/10.1016/B978-0-08-097089-9.00004-8.

16. IEA (2021), Global Energy Review 2021, IEA, Paris https://www.iea.org/reports/global-energy-review-2021.

17. N. Panwar, S. Kaushik, S. J. R. Kothari. Role of renewable energy sources in environmental protection: A review. *Renewable and Sustainable Energy Reviews 15 (3)*, 1513-1524, 2011. DOI: https://doi.org/10.1016/j.rser.2010.11.037.

18. G. Bellini, J. Benziger, D. Bick, G. Bonfini, B. Caccianiga, L. Cadonati; et al. Neutrinos from the primary proton–proton fusion process in the Sun. *Nuclear and Patricle Physics Proceedings 265-266*, 87-92, 2014. DOI: https://doi.org/10.1016/j.nuclphysbps.2015.06.023.

19. H. L. Zhang, J. Baeyens, J. Degrève, G. Cacères. Concentrated solar power plants: Review and design methodology. *Renewable and Sustainable Energy Reviews 22*, 466-481, 2016. DOI: https://doi.org/10.1016/j.rser.2013.01.032.

20. G. M. Joselin Herbert, S. Iniyan, E. Sreevalsan, S. Rajapandian. A review of wind energy technologies. *Renewable and Sustainable Energy Reviews 11 (6)*, 1117-1145, 2007. DOI: https://doi.org/10.1016/j.rser.2005.08.004.

21. M. Bilgili, A. Yasar, E. Simsek. Offshore wind power development in Europe and its comparison with onshore counterpart. *Renewable and Sustainable Energy Reviews 15 (2)*, 905-915, 2011. DOI: https://doi.org/10.1016/j.rser.2010.11.006.

22. J. Moccia, A. Arapogianni. Pure power-wind energy targets for 2020 and 2030. A report by the European Wind Energy Association 43 (1), 2011.

23. D. Krystalidis. Wind Energy in Greece: Economic Analysis; Dissertation, 30, 2022.

24. A. Bauen, G. Berndes, M. Junginger, M. Londo, F. Vuille, R. Ball; et al. Bioenergy: A sustainable reliable energy source. A review of status and prospects, IEA Bioenergy , 108, 2009.

25. L. R. Amjith, B. Bavanish. A review on biomass and wind as renewable energy for sustainable environment. *Chemosphere 293*, 133579, 2022. DOI: https://doi.org/10.1016/j.chemosphere.2022.133579.

26. R.M. Dell, D. A. J. Rand. Understanding batteries. The Royal Society of Chemistry, 2001.

27. P. Moseley, J. Garche. Electrochemical energy storage for renewable sources and grid balancing, Newness, 2015. doi: http://dx.doi.org/10.1016/B978-0-444-62616-5.00001-2.

28. V. S. Bagotsky. Fundamentals of electrochemistry. John Wiley & Sons Inc, 2006.

29. C. G. Zoski. Handbook of electrochemistry. 2006.

30. K. Prasain. Electrochemical Cells and Buffer, Kantipur Engineering College.

31. R. V. Kumar, E. Weal. Chemical and Enviromental Behaviour of Materials: Batteries. University of Cambridge, 2013.

32. J. Garche. Encyclopedia of Electrochemical Power Sources, pp. 28-42, 2009.

33. B. Liu, J. G. Zhang, W. Xu. Advancing Lithium Metal Batteries. *Joule 2 (5)*, 833-845, 2018. DOI: https://doi.org/10.1016/j.joule.2018.03.008.

34. X.B. Cheng, R. Zhang, C.Z. Zhao, Q. Zhang. Toward Safe Lithium Metal Anode in Rechargeable Batteries: A review. *Chemical Reviews 117 (15)*, 10403−10473, 2017. DOI: https://doi.org/10.1021/acs.chemrev.7b00115.

35. J. Cui, T.G. Zhan, K.D. Zhang, D. Chen. The recent advances in constructing designed electrode in lithium metal batteries. *Chinese Chemical Letters 28 (12)*, 2171-2179, 2017. DOI:https://doi.org/10.1016/j.cclet.2017.11.039.

36. T. Najam, S. S. A. Shah, L. Peng, M. S. Javed, M. Imran, M.Q. Zhao, P. Tsiakaras. Synthesis and nano-engineering of MXenes for energy conversion and storage applications: Recent advances and perspectives. *Coordination Chemistry Reviews 454*, 214339, 2022. DOI: https://doi.org/10.1016/j.ccr.2021.214339.

37. H. Liang, X. Gong, L. Jia, F. Chen, Z. Rao, S. Jing, P. Tsiakaras. Highly efficient Li-O2 batteries based on self-standing NiFeP@NC/BC cathode derived from biochar supported Prussian blue analogues. *Journal of Electroanalytical Chemistry 867*, 114124, 2020. DOI: https://doi.org/10.1016/j.jelechem.2020.114124.

38. S. Jing, P. Ding, Y. Zhang, H. Liang, S. Yin, P. Tsiakaras. Lithium-sulfur battery cathodes made of porous biochar support CoFe@ NC metal nanoparticles derived from Prussian blue analogues. *Ionics 25 (11)*, 5297-5304, 2019. DOI: https://doi.org/10.1007/s11581-019-03065-7

39. F. Torabi, P. Ahmadi. Chapter 1- Battery technologies. *Simulation of Battery Systems: Fundamentals and Applications*. pp. 1-54, 2020. DOI:https://doi.org/10.1016/B978-0-12-816212-5.00005-2

40. S. S. Shah, T. Najam, A. Brouzgou, P. Tsiakaras. Alkaline Oxygen Electrocatalysis for Fuel Cells and Metal–Air Batteries. *Encyclopedia of Electrochemistry*, 1-28, 2007. DOI: https://doi.org/10.1002/9783527610426.bard120080.

41. S. Jing, Y. Zhang, F. Chen, H. Liang, S. Yin, P. Tsiakaras. Novel and highly efficient cathodes for Li-O2 batteries: 3D self-standing NiFe@ NC-functionalized N-doped carbon nanonet derived from Prussian blue analogues/biomass composites. *Applied Catalysis B: Environmental 245*, 721-732, 2019. DOI: https://doi.org/10.1016/j.apcatb.2019.01.032.

42. H. Liang, F. Chen, M. Zhang, S. Jing, B. Shen, S. Yin, P. Tsiakaras. Highly performing free standing cathodic electrocatalysts for Li-O2 batteries: CoNiO2 nanoneedle arrays supported on N-doped carbon nanonet. *Applied Catalysis A: General 574*, 114-121, 2019. DOI: https://doi.org/10.1016/j.apcata.2019.01.027.

43. D. Lyu, S. Yao, A. Ali, Z. Q. Tian, P. Tsiakaras, P. K. Shen. N, S Codoped Carbon Matrix-Encapsulated Co9S8 Nanoparticles as a Highly Efficient and Durable Bifunctional Oxygen Redox Electrocatalyst for Rechargeable Zn–Air Batteries. *Advanced Energy Materials 11 (28), 2101249*, 2021. DOI: https://doi.org/10.1002/aenm.202101249.

44. H. Arai, M. Hayashi. Secondary batteries–metal-air systems. In *Encyclopedia of Electrochemical Power Sources*, pp. 347-355, 2009.

45. F. Rahman, M. Baseer, S. Rehman. Assessment of electricity storage systems. In *Solar Energy Storage*, pp. 63-114, 2015. DOI: https://doi.org/10.1016/B978-0-12-409540-3.00004-9

46. J. Jung, L. Zhang, J. Zhang. Lead-acid battery technologies: fundamentals, materials, and applications 8, **2016**.

47. B. G. Pollet, I. Staffell, J. L. Shang, V. Molkov. 22- Fuel Cell (Hydrogen) electric hybrid vehicles. In *Alternative Fuels and Advanced Vehicle Technologies for Improved Environmental Performance*, pp. 685-735, 2014. DOI: https://doi.org/10.1533/9780857097422.3.685.

48. S. Qazi. Fundamentals of Standalone Photovoltaic Systems. In *Standalone Photovoltaic (PV) Systems for Disaster Relief and Remote Areas*, pp. 31-82, 2017. DOI: https://doi.org/10.1016/B978-0-12-803022-6.00002-2.

49. M. M. Thackeray. Batteries, Transportation Applications. In *Encyclopedia of Energy*, 127-139, 2004. DOI: https://doi.org/10.1016/B0-12-176480-X/00187-X.

50. P. J. Tsais, L. I. Chan. 11 - Nickel-based batteries: materials and chemistry. In *Electricity Transmission, Distribution and Storage Systems*, pp. 309-397, 2013. DOI: https://doi.org/10.1533/9780857097378.3.309.

51. M. Yoshio, R. J. Brodd, A. Kozawa. *Lithium-ion batteries* 2009. DOI: https://doi.org/10.1007/978-0-387-34445-4.

52. Q. Wang, P. Ping, X. Zhao, G. Chu, J. Sun, C. Chen. Thermal runaway caused fire and explosion of lithium ion battery. *Journal of Power Sources 208*, 210-224, 2012. DOI: https://doi.org/10.1016/j.jpowsour.2012.02.038.

53. Q. Wang, L. Jiang, Y. Yu, J. Sun. Progress of enhancing the safety of lithium ion battery from the electrolyte aspect. In *Nano Energy 55*, 93-114, 2019. DOI: https://doi.org/10.1016/j.nanoen.2018.10.035.

54. G. Zhang, Y. Shi, H. Wang, L. Jiang, X. Yu, S. Jing, S. Xing, P. Tsiakaras. A facile route to achieve ultrafine Fe2O3 nanorods anchored on graphene oxide for application in lithium-ion battery. *Journal of Power Sources 416*, 118-124, 2019. DOI: https://doi.org/10.1016/j.jpowsour.2019.01.091.

55. P. Simon, Y. Gogotsi. Materials for electrochemical capacitors. *Nanoscience and Technology 7*, 320-329, 2008. DOI: https://doi.org/10.1142/9789814287005_0033.

56. M. S. Halper, J. C. Ellenbogen, McLean. Supercapacitors: A brief overview. The MITRE Corporation, 2006.

57. A. Javaid. 11 - Activated carbon fiber for energy storage. In *Activated Carbon Fiber and Textiles*, pp. 281-303, 2017. DOI: https://doi.org/10.1016/B978-0-08-100660-3.00011-0.

58. N. Shafiei, M. Nasrollahzadeh, G. Hegde. Chapter 10 - Biopolymer-based (nano)materials for supercapacitor applications. In *Biopolymer-Based Metal Nanoparticle Chemistry for Sustainable Applications*, pp. 609-671, 2021.

59. A. Burke. Ultracapacitors: why, how, and where is the technology. *Journal of Power Sources 91 (1)*, 37-50, 2000. DOI: https://doi.org/10.1016/S0378-7753(00)00485-7.

60. R. Kötz, M. Carlen. Principles and applications of electrochemical capacitors. *Electrochimica acta 45 (15-16)*, 2483-2498, 2000. DOI: https://doi.org/10.1016/S0013-4686(00)00354-6.

61. C. Arbizzani, M. Mastragostino, F. Soavi. New trends in electrochemical supercapacitors. *Journal of Power Sources 100 (1-2)*, 164-170, 2001. DOI: https://doi.org/10.1016/S0378-7753(01)00892-8.

62. M. Dai, D. Zhao, X. Wu. Research progress on transition metal oxide based electrode materials for asymmetric hybrid capacitors. *Chinese Chemical Letters 31 (9)*, 2177-2188, 2020. DOI: https://doi.org/10.1016/j.cclet.2020.02.017.

63. P. Simon, Y. Gogotsi. Materials for electrochemical capacitors. In *Nanoscience and technology: a collection of reviews from Nature journals*, World Scientific, pp. 320-329, 2010. DOI:https://doi.org/10.1142/9789814287005_0033.

64. H. Price. Air Analysis | Field Portable Instruments for the Measurement of Airborne Hazards. In *Encyclopedia of Analytical Science (Third Edition)*, pp. 40-43, 2019.

65. W. Vonau, W. Oelßner, U. Guth, J. Henze. An all-solid-state reference electrode. *Sensors and Actuators B: Chemical 144*, 368-373, 2010. DOI: https://doi.org/10.1016/j.snb.2008.12.001.

66. N. R. Stradiotto, H. Yamanaka, M. V. B. Zanoni. Electrochemical sensors: A powerful tool in analytical chemistry. Chemical Society 14(2), 159-173, 2003. DOI: https://doi.org/10.1590/S0103-50532003000200003.

67. W. Y. Yi, K. M. Lo, T. Mak, K. S. Leung, Y. Leung, M. L. Meng. A Survey of Wireless Sensor Network Based Air Pollution Monitoring Systems. Sensors 15 (12), 31392-31427, 2015. DOI: https://doi.org/10.3390/s151229859.

68. E. Gorbova, F. Tzorbatzoglou, C. Molochas, D. Chloros, A. Demin, P. Tsiakaras. Fundamentals and Principles of Solid-State Electrochemical Sensors for High Temperature Gas Detection. *Catalysts 12 (1)*, 1, 2021. DOI: https://doi.org/10.3390/catal12010001.

69. G. Fadeyev, A. Kalakin, A. Demin, A. Volkov, A. Brouzgou, P. Tsiakaras. Electrodes for solid electrolyte sensors for the measurement of CO and H2 content in air. *International journal of hydrogen energy 38 (30)*, 13484-13490, 2013. DOI: https://doi.org/10.1016/j.ijhydene.2013.07.094.

70. A. Kalyakin, A. Demin, E. Gorbova, A. Volkov, P. Tsiakaras. Combined amperometric-potentiometric oxygen sensor. *Sensors and Actuators B: Chemical 313*, 127999, 2020. DOI: https://doi.org/10.1016/j.snb.2020.127999.

71. A. Volkov, E. Gorbova, A. Vylkov, D. Medvedev, A. Demin, P. Tsiakaras. Design and applications of potentiometric sensors based on proton-conducting ceramic materials. A brief review. *Sensors and Actuators B: Chemical 244*, 1004-1015, 2017. DOI: https://doi.org/10.1016/j.snb.2017.01.097.

72. A. Kalyakin, A. Volkov, J. Lyagaeva, D. Medvedev, A. Demin, P. Tsiakaras. Combined amperometric and potentiometric hydrogen sensors based on BaCe0.7Zr0.1Y0.2O3−δ proton-conducting ceramic. *Sensors and Actuators B: Chemical 231*, 175-182, 2016. DOI: https://doi.org/10.1016/j.snb.2016.03.017.

73. A. Kalyakin, J. Lyagaeva, D. Medvedev, A. Volkov, A. Demin, P. Tsiakaras. Characterization of proton-conducting electrolyte based on La0.9Sr0.1YO3–δ and its application in a hydrogen amperometric sensor. *Sensors and Actuators B: Chemical 225*, 446-452, 2016. DOI: https://doi.org/10.1016/j.snb.2015.11.064.

74. G. Balkourani, T. Damartzis, A. Brouzgou, P. Tsiakaras. Cost effective synthesis of graphene nanomaterials for non-enzymatic electrochemical sensors for glucose: a comprehensive review. *Sensors 22(1)*, 355, 2022. DOI: https://doi.org/10.3390/s22010355.

75. G. Balkourani, A. Brouzgou, M. Archonti, N. Papandrianos, S. Song, P. Tsiakaras. Emerging materials for the electrochemical detection of COVID-19. *Journal of Electroanalytical Chemistry 893*, 115289, 2021. DOI: https://doi.org/10.1016/j.jelechem.2021.115289.

76. A. Brouzgou, E. Gorbova, Y. Wang, S. Jing, A. Seretis, Z. Liang, P. Tsiakaras. Nitrogen-doped 3D hierarchical ordered mesoporous carbon supported palladium electrocatalyst for the simultaneous detection of ascorbic acid, dopamine, and glucose. *Ionics 25*, 6061-6070, 2019. DOI: https://doi.org/10.1007/s11581-019-03116-z.

77. X. Yuan, D. Yuan, F. Zeng, W. Zou, F. Tzorbatzoglou, P. Tsiakaras, Y. Wang. Preparation of graphitic mesoporous carbon for the simultaneous detection of hydroquinone and catechol. *Applied Catalysis B: Environmental 129*, 367-374, 2013. DOI: https://doi.org/10.1016/j.apcatb.2012.09.017.

78. V. Dhinakaran, K. Vigneswari, M. Lavanya, M. Varsha Shree. Chapter Ten - Point-of-care applications with graphene in human life. In *Comprehensive Analytical Chemistry 91*, 235-262, 2020. DOI: https://doi.org/10.1016/bs.coac.2020.08.009.

79. A. Demin, E. Gorbova, A. Brouzgou, A. Volkov, P. Tsiakaras. Chapter 6 - Sensors based on solid oxide electrolytes. In *Solid Oxide-Based Electrochemical Devices*, pp. 167-215, 2020. DOI: https://doi.org/10.1016/B978-0-12-818285-7.00006-X.

80. M. S. Cosio, M. Scampicchio, S. Benedetti. Chapter 8 - Electronic Noses and Tongues. In *Chemical Analysis of Food: Techniques and Applications*, pp. 219-247, 2012. DOI: https://doi.org/10.1016/B978-0-12-813266-1.00007-3.

81. A. C. Marques, T. Pinheiro, G. V. Martins, A. R. Cardoso, R. Martins, M. G. Sales; et al. Chapter Seven - Non-enzymatic lab-on-paper devices for biosensing applications. In *Comprehensive Analytical Chemistry*, 89, 189-237, 2020. DOI: https://doi.org/10.1016/bs.coac.2020.05.001.

82. B. Chugh, S. Thakur, A. K. Singh, R. M. Joany, S. Rajendran, T. A. Nguyen. 7 - Electrochemical sensors for agricultural application. In *Nanosensors for Smart Agriculture*, pp. 147-164, 2022. DOI: https://doi.org/10.1016/B978-0-12-824554-5.00018-5.

83. G. Fadeyev, A. Kalyakin, E. Gorbova, A. Brouzgou, A. Demin, A. Volkov, P. Tsiakaras. A simple and low-cost amperometric sensor for measuring H2, CO, and CH4. *Sensors & Actuators B: Chemical 221*, 879-883, 2015. DOI: https://doi.org/10.1016/j.snb.2015.07.034.

84. A. Kalyakin, G. Fadeyev, A. Demin, E. Gorbova, A. Brouzgou, A. Volkov, P. Tsiakaras. Application of Solid oxide proton-conducting electrolytes for amperometric analysis of hydrogen in H2+N2+H2O gas mixtures. *Electrochimica Acta 141*, 120-125, 2014. DOI: https://doi.org/10.1016/j.electacta.2014.06.146.

85. A. Kumar, M. Malinee, A. Dhiman, A. Kumar, T. K. Sharma. Chapter 2 - Aptamer Technology for the Detection of Foodborne Pathogens and Toxins. In *Advanced Biosensors for Health Care Applications*, pp. 45-69, 2019. DOI:https://doi.org/10.1016/B978-0-12-815743-5.00002-0.

86. N. Jaffrezic-Renault, S. V. Dzyadevych. Conductometric Microbiosensors for Environmental Monitoring. Sensors *8(4)*, 2569-2588, 2008. DOI:https://doi.org/10.3390/s8042569.

87. P. M. Grant. Hydrogen lifts off—with a heavy load. *Nature 424*, 129-130, 2003. DOI: https://doi.org/10.1038/424129a.

88. B. Chen, Z. Liu, C. Li, Y. Zhu, L. Fu, Y. Wu, T. van Ree. 9 - Metal oxides for hydrogen storage. In *Metal Oxides in Energy Technologies*, pp. 251-274, 2018. DOI:https://doi.org/10.1016/B978-0-12-811167-3.00009-2.

89. M. Goula, S. Kontou, P. Tsiakaras. Hydrogen production by ethanol steam reforming over a commercial Pd/γ-Al2O3 catalyst. *Applied Catalysis B: Environmental 49(2)*, 135-144, 2004. DOI: https://doi.org/10.1016/j.apcatb.2003.12.001.

90. C. Tarhan, M. A. Çil. A study on hydrogen, the clean energy of the future: Hydrogen storage methods. *Journal of Energy Storage 40*, 102676, 2021. DOI:https://doi.org/10.1016/j.est.2021.102676.

91. B. Zhang, J. Shan, W. Wang, P. Tsiakaras, Y. Li. Oxygen Vacancy and Core–Shell Heterojunction Engineering of Anemone-Like CoP@ CoOOH Bifunctional Electrocatalyst for Efficient Overall Water Splitting. *Small 18(12)*, 2106012, 2022. DOI: https://doi.org/10.1002/smll.202106012.

92. C. Yu, J. Lu, L. Luo, F. Xu, P. K. Shen, P. Tsiakaras, S. Yin. Bifunctional catalysts for overall water splitting: CoNi oxyhydroxide nanosheets electrodeposited on titanium sheets. *Electrochimica Acta 301* 449-457, 2019. DOI: https://doi.org/10.1016/j.electacta.2019.01.149.

93. G.-f. Long, K. Wan, M.-y. Liu, Z.-x. Liang, J.-h. Piao, P. Tsiakaras. Active sites and mechanism on nitrogen-doped carbon catalyst for hydrogen evolution reaction. *Journal of Catalysis 348*, 151-159, 2017. DOI: https://doi.org/10.1016/j.jcat.2017.02.021.

94. L. Zhang, J. Lu, S. Yin, L. Luo, S. Jing, A. Brouzgou, J. Chen, P. K. Shen, P. Tsiakaras. One-pot synthesized boron-doped RhFe alloy with enhanced catalytic performance for hydrogen evolution reaction. *Applied Catalysis B: Environmental 230*, 58-64, 2018. DOI: https://doi.org/10.1016/j.apcatb.2018.02.034.

95. C. Yu, F. Xu, L. Luo, H. S. Abbo, S. J. Titinchi, P. K. Shen, P. Tsiakaras, S. Yin. Bimetallic Ni–Co phosphide nanosheets self-supported on nickel foam as high-performance electrocatalyst for hydrogen evolution reaction. *Electrochimica Acta 317*, 191-198, 2019. DOI: https://doi.org/10.1016/j.electacta.2019.05.150.

96. B. Long, H. Yang, M. Li, M.-S. Balogun, W. Mai, G. Ouyang, Y. Tong, P. Tsiakaras, S. Song. Interface charges redistribution enhanced monolithic etched copper foam-based Cu2O layer/TiO2 nanodots heterojunction with high hydrogen evolution electrocatalytic activity. *Applied Catalysis B: Environmental 243*, 365-372, 2019. DOI: https://doi.org/10.1016/j.apcatb.2018.10.039.

97. J. Lu, Z. Tang, L. Luo, S. Yin, P. Kang Shen, P. Tsiakaras. Worm-like S-doped RhNi alloys as highly efficient electrocatalysts for hydrogen evolution reaction. *Applied Catalysis B: Environmental 255*, 117737, 2019. DOI: https://doi.org/10.1016/j.apcatb.2019.05.039.

98. S. Jing, D. Wang, S. Yin, J. Lu, P. K. Shen, P. Tsiakaras. P-doped CNTs encapsulated nickel hybrids with flower-like structure as efficient catalysts for hydrogen evolution reaction. *Electrochimica acta 298*, 142-149, 2019. DOI: https://doi.org/10.1016/j.electacta.2018.12.055.

99. P. Xu, L. Qiu, L. Wei, Y. Liu, D. Yuan, Y. Wang, P. Tsiakaras. Efficient overall water splitting over Mn doped Ni2P microflowers grown on nickel foam. *Catalysis Today 355*, 815-821, 2020. DOI: https://doi.org/10.1016/j.cattod.2019.04.019.

100. L. Yan, B. Zhang, J. Zhu, Y. Li, P. Tsiakaras, P. Kang Shen. Electronic modulation of cobalt phosphide nanosheet arrays via copper doping for highly efficient neutral-pH overall water splitting. *Applied Catalysis B: Environmental 265*, 118555, 2020. DOI: https://doi.org/10.1016/j.apcatb.2019.118555.

101. A. Saad, Y. Gao, K. A. Owusu, W. Liu, Y. Wu, A. Ramiere, H. Guo, P. Tsiakaras, X. Cai. Ternary Mo2NiB2 as a superior bifunctional electrocatalyst for overall water splitting. *Small 18 (6)*, 2104303, 2021. DOI: https://doi.org/10.1002/smll.202104303.

102. D. M. F. Santos, C. A. C. Sequeira, D. Macciò, A. Saccone, J. L. Figueiredo. Platinum–rare earth electrodes for hydrogen evolution in alkaline water electrolysis. *International Journal of Hydrogen Energy 38 (8)*, 3137-3145, 2013. DOI: https://doi.org/10.1016/j.ijhydene.2012.12.102.

103. N.-T. Suen, S.-F. Hung, Q. Quan, N. Zhang, Y.-J. Xu, H. M. Chen. Electrocatalysis for the oxygen evolution reaction: recent development and future perspectives. *Chemical Society Reviews 46*, 337-365, 2017. DOI: https://doi.org/10.1039/C6CS00328A.

104. Y. Luo, Y. Shi, N. Cai. Chapter 3 - Bridging a bi-directional connection between electricity and fuels in hybrid multienergy systems. In *Hybrid Systems and Multi-energy Networks for the Future Energy Internet*, pp. 41-84, 2021. DOI: https://doi.org/10.1016/B978-0-12-819184-2.00003-1.

105. J. Cen, E. Jiang, Y. Zhu, Z. Chen, P. Tsiakaras, P. K. Shen. Enhanced electrocatalytic overall water splitting over novel one-pot synthesized Ru–MoO3-x and Fe3O4–NiFe layered double hydroxide on Ni foam. *Renewable Energy 177*, 1346-1355, 2021. DOI: https://doi.org/10.1016/j.renene.2021.06.005.

106. P. Millet. 9 - Hydrogen production by polymer electrolyte membrane water electrolysis. In *Compendium of Hydrogen Energy*, pp. 255-286, 2015. DOI: https://doi.org/10.1016/B978-1-78242-361-4.00009-1.

107. T. Momma, H. Nara, T. Osaka. APPLICATIONS–PORTABLE. *Encyclopedia of Electrochemical Power Sources*, pp. 1-46, 2013.

108. M. Ni, M. H. Leung, D. Leung. Technological development of hydrogen production by solid oxide electrolyzer cell (SOEC). *International Journal of Hydrogen Energy 33 (9)*, 2337-2354, 2008. DOI: https://doi.org/10.1016/j.ijhydene.2008.02.048.

109. Z. Chenhuan, Z. Wenqiang, Y. Bo, W. Jianchen, C. Jing. Solid Oxide Electrolyzer Cells. *Progress in Chemistry 28 (8)*, 1265-1288, 2016. DOI: https://doi.org/10.7536/PC151105.

110. R. O'hayre, S.-W. Cha, W. Colella, F. B. Prinz. *Fuel cell fundamentals*, John Wiley & Sons, Inc., 2016.

111. S. Radford. Fuel Cells. 2017–https://energync.org/fuel-cells-2/.

112. S. Mekhilef, R. Saidur, A. Safari. Comparative study of different fuel cell technologies. *Renewable and Sustainable Energy Reviews 16 (1)*, 981-989, 2012. DOI: https://doi.org/10.1016/j.rser.2011.09.020.

113. M. Alhassan, M. U. Garba. Design of an alkaline fuel cell. *Journal of Practices Technologies 5 (9)*, 99-106, 2006.

114. A. Brouzgou, S. Song, P. Tsiakaras. Carbon-supported PdSn and Pd3Sn2 anodes for glucose electrooxidation in alkaline media. *Applied Catalysis B: Environmental 158-159*, 209-216, 2014. DOI: https://doi.org/10.1016/j.apcatb.2014.03.051.

115. N. Sammes, R. Bove, K. Stahl. Phosphoric acid fuel cells: Fundamentals and applications. *Current Opinion in Solid State and Materials Science 8 (5)*, 372-378, 2004. DOI: https://doi.org/10.1016/j.cossms.2005.01.001.

116. A. Dicks, J. Larminie. *Fuel cell systems explained*, John Wiley & Sons Inc., 2003.

117. A. L. Dicks. Molten carbonate fuel cells. *Current Opinion in Solid State and Materials Science 8 (5)*, 379-383, 2004. DOI: https://doi.org/10.1016/j.cossms.2004.12.005.

118. J. Hirschenhofer, D. Stauffer, R. Engleman, M. Klett. Fuel Cell Handbook, Fourth Edition, 1998. DOI: https://doi.org/10.2172/14997.

119. I. Dincer, Y. Bicer. Integrated Energy Systems for Multigeneration, 2020. DOI: https://doi.org/10.1016/C2015-0-06233-5.

120. F. A. Coutelieris, S. Douvartzides, P. Tsiakaras. The importance of the fuel choice on the efficiency of a solid oxide fuel cell system. *Journal of Power Sources 123 (2)*, 200-205, 2003. DOI: https://doi.org/10.1016/S0378-7753(03)00559-7.

121. R. Ormerod. Solid oxide fuel cells. *Chemical Society Reviews 32*, 17-28, 2003. DOI: https://doi.org/10.1039/B105764M.

122. C. Pijolat. Screen-printing for the fabrication of solid oxide fuel cells (SOFC). In *Printed Films*, pp. 469-495, 2012. DOI: https://doi.org/10.1533/9780857096210.2.469.

123. D. Medvedev, V. Maragou, E. Pikalova, A. Demin, P. Tsiakaras. Novel composite solid state electrolytes on the base of BaCeO3 and CeO2 for intermediate temperature electrochemical devices. *Journal of power sources 221*, 217-227, 2013. DOI: https://doi.org/10.1016/j.jpowsour.2012.07.120.

124. L. A. Dunyushkina, A. A. Pankratov, V. P. Gorelov, A. Brouzgou, P. Tsiakaras. Deposition and Characterization of Y-doped CaZrO3 Electrolyte Film on a Porous SrTi0.8Fe0.2O3-δ Substrate. *Electrochimica Acta 202*, 39-46, 2016. DOI: https://doi.org/10.1016/j.electacta.2016.03.120.

125. C. G. Vayenas, S. Bebelis, I. V. Yentekakis, H. G. Lintz. Non-faradaic electrochemical modification of catalytic activity: A status report. *Catalysis Today 11 (3)*, 303-438, 1992. DOI: https://doi.org/10.1016/0920-5861(92)80002-5.

126. J. Lagaeva, D. Medvedev, A. Demin, P. Tsiakaras. Insights on thermal and transport features of BaCe0.8−xZrxY0.2O3−δ proton-conducting materials. *Journal of Power Sources 278*, 436-444, 2015. DOI: https://doi.org/10.1016/j.jpowsour.2014.12.024.

127. P. Sharma, O. P. Pandey. Chapter 1 - Proton exchange membrane fuel cells: fundamentals, advanced technologies, and practical applications. In *PEM Fuel Cells*, pp. 1-24 , 2022. DOI: https://doi.org/10.1016/B978-0-12-823708-3.00006-7.

128. T. Najam, S. S. A. Shah, S. Ibraheem, X. Cai, E. Hussain, S. Suleman, M. S. Javed, P. Tsiakaras. Single-atom catalysis for zinc-air/O2 batteries, water electrolyzers and fuel cells applications. *Energy Storage Materials 45*, 504-540, 2022. DOI: https://doi.org/10.1016/j.ensm.2021.11.050.

129. Q. Chen, Z. Chen, A. Ali, Y. Luo, H. Feng, Y. Luo, P. Tsiakaras, P. Kang Shen. Shell-thickness-dependent Pd@PtNi core–shell nanosheets for efficient oxygen reduction reaction. *Chemical Engineering Journal 427*, 131565, 2022. DOI: https://doi.org/10.1016/j.cej.2021.131565.

130. X. Zhu, L. Huang, M. Wei, P. Tsiakaras, P. K. Shen. Highly stable Pt-Co nanodendrite in nanoframe with Pt skin structured catalyst for oxygen reduction electrocatalysis. *Applied Catalysis B: Environmental 281*, 119460, 2021. DOI: https://doi.org/10.1016/j.apcatb.2020.119460.

131. K. Wang, H. Chen, X. Zhang, Y. Tong, S. Song, P. Tsiakaras, Y. Wang. Iron oxide@graphitic carbon core-shell nanoparticles embedded in ordered mesoporous N-doped carbon matrix as an efficient cathode catalyst for PEMFC. *Applied Catalysis B: Environmental 264*, 118468, 2020. DOI: https://doi.org/10.1016/j.apcatb.2019.118468.

132. H. S. Das, M. F. F. Chowdhury, S. Li, C. W. Tan. 9 - Fuel cell and hydrogen power plants. In *Hybrid Renewable Energy Systems and Microgrids*, pp. 313-349, 2021. DOI: https://doi.org/10.1016/B978-0-12-821724-5.00009-X.

133. G. M. Andreadis, A. K. M. Podias, P. E. Tsiakaras. The effect of the parasitic current on the Direct Ethanol PEM Fuel Cell Operation. *Journal of Power Sources 181 (2)*, 214-227, 2008. DOI: https://doi.org/10.1016/j.jpowsour.2008.01.060.

134. K. Wang, Y. Wang, Z. Liang, Y. Liang, D. Wu, S. Song, P. Tsiakaras. Ordered mesoporous tungsten carbide/carbon composites promoted Pt catalyst with high activity and stability for methanol electrooxidation. *Applied Catalysis B: Environmental 147*, 518-525, 2014. DOI: https://doi.org/10.1016/j.apcatb.2013.09.020.

135. Y. Wang, C. He, A. Brouzgou, Y. Liang, R. Fu, D. Wu, P. Tsiakaras, S. Song. A facile soft-template synthesis of ordered mesoporous carbon/tungsten carbide composites with high surface area for methanol electrooxidation. *Journal of Power Sources 200*, 8-13, 2012. DOI: https://doi.org/10.1016/j.jpowsour.2011.10.037.

136. X.-Z. Yuan, H. Wang. PEM fuel cell fundamentals. In *PEM fuel cell electrocatalysts and catalyst layers*, pp. 1-87, 2008. DOI: https://doi.org/10.10007/978-1-84800-936-3.

137.Edelweiss Publications, Nanomaterial Chemistry and Technology https://edelweisspublications.com/keyword/26/1574/PEM-Fuel-cell.

138. N. Wakabayashi, M. Takeichi, H. Uchida, M. Watanabe. Temperature dependence of oxygen reduction activity at Pt− Fe, Pt− Co, and Pt− Ni alloy electrodes. *The Journal of Physical Chemistry B 109 (12)*, 5836-5841, 2005. DOI: https://doi.org/10.1021/jp046204+.

139. X. Cheng, B. Yi, M. Han, J. Zhang, Y. Qiao, J. Yu. Investigation of platinum utilization and morphology in catalyst layer of polymer electrolyte fuel cells. *Journal of Power Sources 79 (1)*, 75-81, 1999. DOI: https://doi.org/10.1016/S0378-7753(99)00046-4.

140. Z. Qi. Proton exchange membrane fuel cells. CRC Press, 2013.

141. A. Panchenko. Polymer electrolyte membrane degradation and oxygen reduction in fuel cells: an EPR and DFT investigation. 2004. DOI: http://dx.doi.org/10.18419/opus-780.

142. I. Fouzaï, S. Gentil, V. C. Bassetto, W. O. Silva, R. Maher, H. H. Girault. Catalytic layer-membrane electrode assembly methods for optimum triple phase boundaries and fuel cell performances. *Journal of Materials Chemistry A 9 (18)*, 11096-11123, 2021. DOI: https://doi.org/10.1039/D0TA07470E.

143. J. Zhang. *PEM fuel cell electrocatalysts and catalyst layers: fundamentals and applications*. Springer Science & Business Media, 2008. DOI: https://doi.org/10.1007/978-1-84800-936-3.

144. F. T. Wagner, B. Lakshmanan, M. F. Mathias. Electrochemistry and the future of the automobile. *The Journal of Physical Chemistry Letters 1 (14)*, 2204-2219, 2010. DOI: https://doi.org/10.1021/jz100553m.

145. M. Shao, Q. Chang, J.-P. Dodelet, R. Chenitz. Recent advances in electrocatalysts for oxygen reduction reaction. *Chemical reviews 116 (6)*, 3594-3657, 2016. DOI: https://doi.org/10.1021/acs.chemrev.5b00462.

146. G. Elia. Characterization of voltage loss for proton exchange membrane fuel cell. Diploma Thesis ,Department of Fluid Mechanics, Universitat Politècnica de Catalunya, 2015.

147. E. Zakrisson. The effect of start/stop strategy on PEM fuel cell degradation characteristics. Diploma Thesis, Department of Applied Physics of the Chalmers University of Technology, 2011.

148. J.-C. Lin, H. R. Kunz, J. M. Fenton, S. S. Fenton. The fuel cell: An ideal chemical engineering undergraduate experiment. *Chemical Engineering Education 38*, 38-47, 2004. DOI: https://doi.org/10.18260/1-2--11682.

149. Y. Akimoto, K. Okajima. Semi-empirical equation of PEMFC considering operation temperature,. *Energy Technology & Policy 1 (1)*, 91-96, 2014. DOI: https://doi.org/10.1080/23317000.2014.972480.

150. A. Husar, S. Strahl, J. Riera. Experimental characterization methodology for the identification of voltage losses of PEMFC: Applied to an open cathode stack. *International journal of hydrogen energy 37 (8)*, 7309-7315, 2012. DOI: https://doi.org/10.1016/j.ijhydene.2011.11.130.

151. F. Barbir. PEM Fuel Cells-Theory and Practice.Elsevier Inc., 2005.

152. L. Carrette, K. Friedrich, M. Huber, U. Stimming. Improvement of CO tolerance of proton exchange membrane (PEM) fuel cells by a pulsing technique. *Physical Chemistry Chemical Physics 3(3)*, 320-324, 2001. DOI: https://doi.org/10.1039/B005843M.

153. J. Rostrup-Nielsen, K. Aasberg-Petersen. Steam reforming, ATR, partial oxidation: catalysts and reaction engineering. *John Wiley & Sons*, 2010. DOI: https://doi.org/10.1002/9780470974001.f302015.

154. J. Zhang, R. Datta. Electrochemical preferential oxidation of CO in reformate. *Journal of The Electrochemical Society 152 (6)*, 2005. DOI: https://doi.org/10.1149/1.1905983.

155. V. F. Valdés-López, T. Mason, P. R. Shearing, D. Brett. Carbon monoxide poisoning and mitigation strategies for polymer electrolyte membrane fuel cells – A review. *Progress in Energy and Combustion Science 79*, 100842, 2020. DOI: https://doi.org/10.1016/j.pecs.2020.100842.

156. W. Adams, J. Blair, K. Bullock, C. Gardner. Enhancement of the performance and reliability of CO poisoned PEM fuel cells. *Journal of power sources 145 (1)*, 55-61, 2005. DOI: https://doi.org/10.1016/j.jpowsour.2004.12.049.

157. A. A. Franco. Polymer electrolyte fuel cells: Science, Applications, and Challenges. CRC Press, 2013.

158. C. Molochas, P. Tsiakaras. Carbon Monoxide Tolerant Pt-Based Electrocatalysts for H2-PEMFC Applications: Current Progress and Challenges. *Catalysts* 11 (9), 1127, 2021. DOI: https://doi.org/10.3390/catal11091127.

159. B. Beden, A. Bewick, K. Kunimatsu, C. Lamy. Infrared study of adsorbed species on electrodes: Adsorption of carbon monoxide on Pt, Rh and Au. *Journal of Electroanalytical Chemistry and Interfacial Electrochemistry 142 (1-2)*, 345-356., 1982. DOI: https://doi.org/10.1016/S0022-0728(82)80026-0.

160. A. Kabbabi, R. Faure, R. Durand, B. Beden, F. Hahn, J.-M. Leger, C. Lamy. In situ FTIRS study of the electrocatalytic oxidation of carbon monoxide and methanol at platinum–ruthenium bulk alloy electrodes. *Journal of Electroanalytical Chemistry 444 (1)*, 41-53, 1998. DOI: https://doi.org/10.1016/S0022-0728(97)00558-5.

161. S. Ye, T. Kondo, N. Hoshi, J. Inukai, S. Yoshimoto, M. Osawa, K. J. E. Itaya. Recent progress in electrochemical surface science with atomic and molecular levels. *77*, 2-20. 2009. DOI: https://doi.org/10.5796/electrochemistry.77.2.

162. H. Igarashi, T. Fujino, M. Watanabe. Hydrogen electro-oxidation on platinum catalysts in the presence of trace carbon monoxide. *Journal of Electroanalytical Chemistry 391 (1-2)*, 119-123, 1995. DOI: https://doi.org/10.1016/0022-0728(95)03914-3.

163. W. A. Adams, J. Blair, K. R. Bullock, C. L. Gardner. Enhancement of the performance and reliability of CO poisoned PEM fuel cells. *Journal of Power Sources 145*, 55-61, 2005. DOI: https://doi.org/10.1016/j.jpowsour.2004.12.049.

164. P. P. Lopes, K. S. Freitas, E. A. Ticianelli. CO tolerance of PEMFC anodes: Mechanisms and Electrode designs. *Electrocatalysis 1 (4)*, 200-212, 2010. DOI: https://doi.org/10.1007/s12678-010-0025-y.

165. O. J. Guy, K.-A. D. Walker. Chapter 4 - Graphene Functionalization for Biosensor Applications. In *Silicon Carbide Biotechnology (Second Edition)***,** pp. 85-141, 2016. DOI: https://doi.org/10.1016/B978-0-12-802993-0.00004-6.

166. C.-y. Hui, C.-w. Kan, C.-l. Mak, K.-h. Chau. Flexible Energy Storage System—An Introductory Review of Textile-Based Flexible Supercapacitors. *Processes 7 (12)*, 922, 2019. DOI: https://doi.org/10.3390/pr7120922.

167. J. Scotto, W. A. Marmisollé, D. Posadas. About the capacitive currents in conducting polymers: the case of polyaniline. *Journal of Solid State Electrochemistry 23 (7)*, 1947-1965, 2019. DOI: https://doi.org/10.1007/s10008-019-04291-9.

168. R. Dominko, S. Drvarič Talian, A. Vizintin. Lithium sulfur batteries: Electrochemistry and mechanistic research. In *Reference Module in Chemistry, Molecular Sciences and Chemical Engineering*, 2021. DOI: https://doi.org/10.1016/B978-0-12-823144-9.00056-X.

169. A. J. Bard, L. R. Faulkner, H. S. White. Electrochemical methods: fundamentals and applications (Third Edition). John Wiley & Sons, 2022.

170. N. O. Laschuk, E. B. Easton, O. V. Zenkina. Reducing the resistance for the use of electrochemical impedance spectroscopy analysis in materials chemistry. *RSC Advances 11 (45)*, 27925-27936, 2021. DOI: https://doi.org/10.1039/D1RA03785D.

171. J. J. Giner-Sanz, E. Ortega, M. García-Gabaldón, V. Pérez-Herranz. Theoretical Determination of the Stabilization Time in Galvanostatic EIS Measurements: The Simplified Randles Cell. *Journal of The Electrochemical Society 165 (13)*, 628, 2018.

172. W. Choi, H.-C. Shin, J. M. Kim, J.-Y. Choi, W.-S. Yoon. Modeling and applications of electrochemical impedance spectroscopy (EIS) for lithium-ion batteries. *Journal of Electrochemical Science Technology 11 (1)*, 1-13, 2020. DOI: https://doi.org/10.33961/jecst.2019.00528.

173. M. El-Azazy, M. Min, P. Annus. *Electrochemical Impedance Spectroscopy*, BoD – Books on Demand, 2020. DOI: https://dx.doi.org/10.5772/intechopen.87884.

174. X.-Z. Yuan, C. Song, H. Wang, J. Zhang. EIS Equivalent Circuits. In *Electrochemical Impedance Spectroscopy in PEM Fuel Cells: Fundamentals and Applications*, pp. 139-192, 2010. DOI: https://doi.org/10.1007/978-1-84882-846-9.

175. Gamry Instruments Inc, Complex impedance in Corrosion. Basics of electrochemical impedance spectroscopy, 1-30, 2007.

176. R. K. Franklin, S. M. Martin, T. D. Strong, R. B. Brown. Chemical and Biological Systems: Chemical Sensing Systems for Liquids. In *Reference Module in Materials Science and Materials Engineering*, 2016. DOI: https://doi.org/10.1016/B978-0-12-803581-8.00549-X.

177. J.C. Lindon, G. E. Tranter, D. Koppenaal. Spectroelectrochemistry, Methods and Instrumentation. In *Encyclopedia of Spectroscopy and Spectrometry (Third Edition)*, pp. 172-177, 2016.

178. P.T. Kissinger, W.R. Heineman Laboratory Techniques in Electroanalytical Chemistry (Second edition), Marcel Dekker Inc., 1996.

179. K. Scott, E. H. Yu. Microbial electrochemical and fuel cells: fundamentals and applications, 2015. DOI: http://dx.doi.org/10.1016/B978-1-78242-375-1.00001-0.

180. H. Wang, X.-Z. Yuan, H. Li. PEM fuel cell diagnostic tools 2, 2011.

181. N.-T. Suen, S.-F. Hung, Q. Quan, N. Zhang, Y.-J. Xu, H. M. Chen. Electrocatalysis for the oxygen evolution reaction: recent development and future perspectives. *Chemical Society Reviews 46 (2)*, 337-365, 2017. DOI: https://doi.org/10.1039/C6CS00328A.

182. S. Song, P. Tsiakaras. Recent progress in direct ethanol proton exchange membrane fuel cells (DE-PEMFCs). *Applied Catalysis B: Environmental 63 (3-4)*, 187-193, 2006. DOI: https://doi.org/10.1016/j.apcatb.2005.09.018.

183. K. Christmann, K. A. Friedrich, N. Zamel. Activation mechanisms in the catalyst coated membrane of PEM fuel cells. *Progress in Energy and Combustion Science 85*, 100924, 2021. DOI: https://doi.org/10.1016/j.pecs.2021.100924.

184. M. M. Taghiabadi, M. Zhiani, V. Silva. Effect of MEA activation method on the long-term performance of PEM fuel cell. *Applied Energy 242*, 602-611, 2019. DOI: https://doi.org/10.1016/j.apenergy.2019.03.157.

185. X.-Z. Yuan, S. Zhang, J. C. Sun, H. Wang. A review of accelerated conditioning for a polymer electrolyte membrane fuel cell. *Journal of Power Sources 196 (22)*, 9097-9106, 2011. DOI: https://doi.org/10.1016/j.jpowsour.2011.06.098.

186. M. Zhiani, S. Majidi, M. M. Taghiabadi. Comparative Study of on-Line Membrane Electrode Assembly Activation Procedures in Proton Exchange Membrane Fuel Cell. *Fuel Cells- From Fundamentals to Systems 13 (5)*, 946-955, 2013. DOI: https://doi.org/10.1002/fuce.201200139.

187. D. Chen, P. Pei, Y. Li, P. Ren, Y. Meng, X. Song, Z. Wu. Proton exchange membrane fuel cell stack consistency: Evaluation methods, influencing factors, membrane electrode assembly parameters and improvement measures. *Energy Conversion and Management 261*, 115651, 2022. DOI: https://doi.org/10.1016/j.enconman.2022.115651.

188. J. Wu, X. Z. Yuan, H. Wang, M. Blanco, J. J. Martin, J. Zhang. Diagnostic tools in PEM fuel cell research: Part I Electrochemical techniques. *International Journal of Hydrogen Energy 33 (6)*, 1735-1746, 2008. DOI: https://doi.org/10.1016/j.ijhydene.2008.01.013.

189. M. Salam, M. Habib, P. Arefin, K. Ahmed, M. Uddin, T. Hossain, N. Papri. Effect of Temperature on the Performance Factors and Durability of Proton Exchange Membrane of Hydrogen Fuel Cell: A Narrative Review. *Material Science Research India 53 (17)*, 179-191, 2020. DOI: http://dx.doi.org/10.13005/msri/170210.

190. J. Zhang, Y. Tang, C. Song, Z. Xia, H. Li, H. Wang, J. Zhang. PEM fuel cell relative humidity (RH) and its effect on performance at high temperatures. *Electrochimica Acta 53 (16)*, 5315-5321, 2008. DOI: https://doi.org/10.1016/j.electacta.2008.02.074.

191. J. Zhang, J. Wu, H. Zhang, J. Zhang. PEM fuel cell testing and diagnosis, Newnes. 2013. DOI: http://dx.doi.org/10.1016/B978-0-444-53688-4.00001-2

192. V. B. R. e Silva. Polymer electrolyte membrane fuel cells: activation analysis and operating conditions optimization. Diploma Thesis, Department of Chemical Engineering ,Universidade do Porto (Portugal), 2009.

193. X.-Z. Yuan, S. Zhang, J. C. Sun, H. Wang. A review of accelerated conditioning for a polymer electrolyte membrane fuel cell. *Journal of Power Sources 196 (22)*, 9097-9106, 2011. DOI: https://doi.org/10.1016/j.jpowsour.2011.06.098.

194. A. Brouzgou, A. Seretis, S. Song, P. K. Shen, P. Tsiakaras. CO tolerance and durability study of PtMe(Me = Ir or Pd) electrocatalysts for H2-PEMFC application. *International Journal of Hydrogen Energy 46 (26)*, 13865-13877, 2021. DOI: https://doi.org/10.1016/j.ijhydene.2020.07.224.

195. F. Grumm, M. Schumann, C. Cosse, M. Plenz, A. Lücken, D. Schulz. Short circuit characteristics of pem fuel cells for grid integration applications. *Electronics 9 (4)*, 602, 2020. DOI: https://doi.org/10.3390/electronics9040602.

196. M. A. Khan, J. Yuan, B. Sunden. Simulation of Multiphase Transport Phenomena in PEMFC Involving Water Phase Change, 2010.

197. J. Zhang, Z. Xie, J. Zhang, Y. Tang, C. Song, T. Navessin, Z. Shi, D. Song, H. Wang, D. P. Wilkinson. High temperature PEM fuel cells. *Journal of power Sources 160 (2)*, 872-891, 2006. DOI: https://doi.org/10.1016/j.jpowsour.2006.05.034.

198. S. Haji. Analytical modeling of PEM fuel cell i–V curve. *Renewable Energy 36 (2)*, 451-458, 2011. DOI: https://doi.org/10.1016/j.renene.2010.07.007.

199. M. Ciureanu. Effects of Nafion® dehydration in PEM fuel cells. *Journal of Applied Electrochemistry 34 (7)*, 705-714. 2004. DOI: https://doi.org/10.1023/B:JACH.0000031102.32521.c6.

200. S. Strahl, A. Husar, P. Puleston, J. Riera. Performance improvement by temperature control of an open-cathode PEM fuel cell system. *Fuel Cells-From Fundamentals to Systems 14 (3)*, 466-478, 2014. DOI: https://doi.org/10.1002/fuce.201300211.

201. B. G. Abraham, R. Bhaskaran, R. Chetty. Electrodeposited bimetallic (PtPd, PtRu, PtSn) catalysts on titanium support for methanol oxidation in direct methanol fuel cells. *Journal of The Electrochemical Society 167 (2)*, 24512, 2020. DOI: https://doi.org/10.1149/1945-7111/ab6a7d.

202. E. Carcadea, M. Varlam, A. Marinoiu, M. Raceanu, M. S. Ismail, D. B. Ingham. Influence of catalyst structure on PEM fuel cell performance – A numerical investigation. *International Journal of Hydrogen Energy 44 (25)*, 12829-12841, 2019. DOI: https://doi.org/10.1016/j.ijhydene.2018.12.155.

203. A. Caillard, C. Charles, D. Ramdutt, R. Boswell, P. Brault. Effect of Nafion and platinum content in a catalyst layer processed in a radio frequency helicon plasma system. *Journal of Physics D: Applied Physics 42 (4)*, 45207, 2009. DOI: https://doi.org/10.1088/0022-3727/42/4/045207.

204. M. Łukaszewski, M. Grdeń, A. Czerwiński. Cyclic voltammetric behavior of Pd–Pt–Rh ternary alloys. *Journal of Solid State Electrochemistry 9 (1)*, 1-9, 2005. DOI: https://doi.org/10.1007/s10008-004-0528-7.

205. M. Johansson, E. Skulason, G. Nielsen, S. Murphy, R. M. Nielsen, I. Chorkendorff. Hydrogen adsorption on palladium and palladium hydride at 1 bar. *Surface Science 604 (7-8)*, 718-729, 2010. DOI: https://doi.org/10.1016/j.susc.2010.01.023.

206. F. Si, Y. Zhang, L. Yan, J. Zhu, M. Xiao, C. Liu; et al. 4-*Electrochemical Oxygen Reduction Reaction*. In Rotating Electrode Methods and Oxygen Reduction Electrocatalysts, pp. 133-170, 2014. DOI: https://doi.org/10.1016/B978-0-444-63278-4.00004-5.

207. E. Antolini. Palladium in fuel cell catalysis. *Energy & Environmental Science 2 (9)*, 915-931, 2009. DOI: https://doi.org/10.1039/B820837A.

208. G. Catlin. PEM fuel cell modeling and optimization using a genetic algorithm. Diploma Thesis, Department of Mechanical Engineering of the University of Delaware, 2022.

209. M. Arif, S. Cheung, J. Andrews. A systematic approach for matching simulated and experimental polarization curves for a PEM fuel cell. *International Journal of Hydrogen Energy 45 (3)*, 2206-2223, 2020. DOI: https://doi.org/10.1016/j.ijhydene.2019.11.057.

210. H. A. Gasteiger, J. E. Panels, S. G. Yan. Dependence of PEM fuel cell performance on catalyst loading. *Journal of Power Sources 127 (1-2)*, 162-171, 2004. DOI: https://doi.org/10.1016/j.jpowsour.2003.09.013.

211. C. Jackson, L. Raymakers, M. Mulder, A. Kucernak. Assessing electrocatalyst hydrogen activity and CO tolerance: Comparison of performance obtained using the high mass transport 'floating electrode' technique and in electrochemical hydrogen pumps. *Applied Catalysis B: Environmental 268*, 118734, 2020. DOI: https://doi.org/10.1016/j.apcatb.2020.118734.

212. O. Himanen, T. Hottinen, M. Mikkola, V. Saarinen. Characterization of membrane electrode assembly with hydrogen–hydrogen cell and ac-impedance spectroscopy: Part I. Experimental. *Electrochimica acta 52 (1)*, 206-214, 2006. DOI: https://doi.org/10.1016/j.electacta.2006.05.016.

213. N. Wagner, W. Schnurnberger, B. Müller, M. Lang. Electrochemical impedance spectra of solid-oxide fuel cells and polymer membrane fuel cells. *Electrochimica Acta 43 (24)*, 3785-3793, 1998. DOI: https://doi.org/10.1016/S0013-4686(98)00138-8.

214. M. Ciureanu, H. Wang. Electrochemical Impedance Study of Electrode-Membrane Assemblies in PEM Fuel Cells: I. Electro-oxidation of H2 and H2/CO Mixtures on Pt-Based Gas-Diffusion Electrodes. *Journal of the Electrochemical Society 146 (11)*, 4031, 1999. DOI: https://doi.org/10.1149/1.1392588.

215. Q. Li, R. He, J.-A. Gao, J. O. Jensen, N. J. t. Bjerrum. The CO poisoning effect in PEMFCs operational at temperatures up to 200oC. *Journal of the Electrochemical Society 150 (12)*, A1599, 2003. DOI: https://doi.org/10.1149/1.1619984.

216. S. Lee, S. Mukerjee, E. Ticianelli, J. McBreen. Electrocatalysis of CO tolerance in hydrogen oxidation reaction in PEM fuel cells. *Electrochimica Acta 44 (19)*, 3283-3293, 1999. DOI: https://doi.org/10.1016/S0013-4686(99)00052-3.

217. X. Wei, R.-Z. Wang, W. Zhao, G. Chen, M.-R. Chai, L. Zhang, J. Zhang. Recent research progress in PEM fuel cell electrocatalyst degradation and mitigation strategies. *EnergyChem 3 (5)*, 100061, 2021. DOI: https://doi.org/10.1016/j.enchem.2021.100061.

218. M. S. Yazici, S. Dursun, I. Borbáth, A. Tompos. Reformate gas composition and pressure effect on CO tolerant Pt/Ti0. 8Mo0. 2O2–C electrocatalyst for PEM fuel cells. *International Journal of Hydrogen Energy 46 (25)*, 13524-13533, 2021. DOI: https://doi.org/10.1016/j.ijhydene.2020.08.226

219. R. Jiang, H. R. Kunz, J. M. Fenton. Electrochemical Oxidation of H2 and H2/CO Mixtures in Higher Temperature (Tcell 100°C) Proton Exchange Membrane Fuel Cells: Electrochemical Impedance Spectroscopy. *Journal of the Electrochemical Society 152 (7)*, A1329, 2005. DOI: https://doi.org/10.1149/1.1928067.

220. X. Yuan, H. Wang, J. Colin Sun, J. Zhang. AC impedance technique in PEM fuel cell diagnosis—A review. *International Journal of Hydrogen Energy 32 (17)*, 4365-4380, 2007. DOI: https://doi.org/10.1016/j.ijhydene.2007.05.036.

221. S. Gottesfeld, J. Pafford. A new approach to the problem of carbon monoxide poisoning in fuel cells operating at low temperatures. *J. Electrochemical Society 135 (10)*, 2651-2652, 1988.